Chair of Applied Mechanics
Department of Mechanical Engineering
Technical University of Munich

Design of a Controller to Stabilize a Biped Robot under Consideration of Structural Dynamics

Auslegung der Stabilisierungsregelung eines humanoiden Laufroboters unter Berücksichtigung der Strukturdynamik

Scientific work for obtaining the academic degree
Master of Science in Robotics, Cognition, Intelligence (M.Sc.)
at the Department of Informatics of the Technical University of Munich

Supervisor Prof. Dr. Daniel J. Rixen
Chair of Applied Mechanics

Advisor Felix Sygulla, M.Sc.
Chair of Applied Mechanics

Submitted by Oskar Baumann, B.Sc.

Submitted on May 15, 2020 in Garching bei München

Contents

Acronyms

ARE Algebraic Ricatti Equation

CCF Controllable Canonical Form

CoG Center of Gravity

CoM Center of Mass

DARE Discrete Algebraic Ricatti Equation

DoF Degree of Freedom

EoM equations of motion

IMU Inertia Measurement Unit

LQR Linear Quadratic Regulator

LTI Linear Time-Invariant

MBS Multi-Body Simulation

MRE Mean Relative Error

ODE Ordinary Differential Equation

ODEs Ordinary Differential Equations

PPF Positive Position Feedback

RMSE Root Mean Squared Error

SIMO Single-Input-Multiple-Output

List of Figures

List of Tables

Chapter 1

Introduction

Robots have changed the human society fundamentally. Many tasks in production which had to be done by humans are nowadays performed by industrial robots that can perform repetitive tasks faster and with higher precision. These robots are often inflexible and tailored exactly to their application and work in a completely defined and certain work environment. But the market for robots that are able to work in uncertain environments is rapidly growing. Robot solutions are developed to help humans with their every day life. For example there are robots that navigate autonomously through homes and help cleaning by vacuuming the floor. Such robots are limited in their locomotion as they mostly base on wheels which cause problems in uneven environments like a staircase or in the outdoors. Thus, it is desired to develop robot anatomies that allow to move through uncertain and uneven terrain. One approach is to recreate humanoid walking as walking on two feet allows for locomotion in tight spaces with uneven terrain as it is proven by humans everyday.

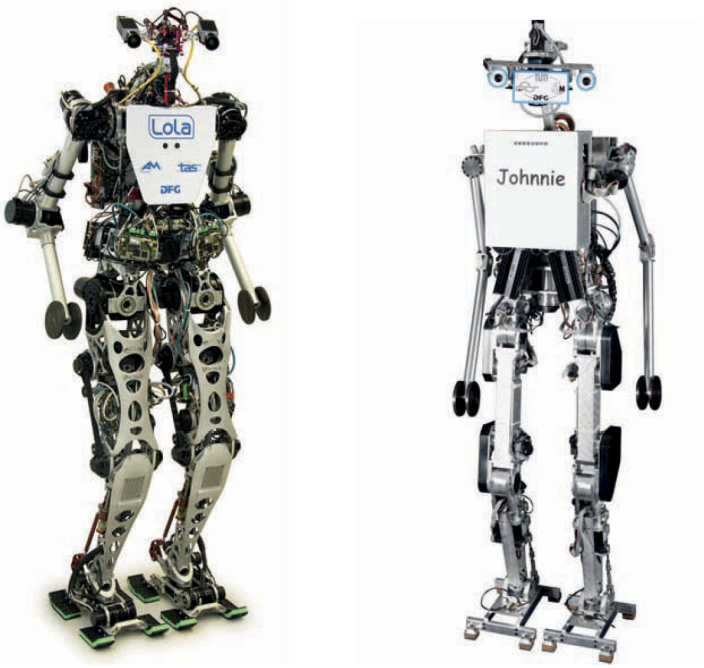

Figure 1.1: Biped robots Lola and Johnnie from the Chair of Applied Mechanics at TUM [5]

At the Chair of Applied Mechanics at the Technical University of Munich (TUM) the research on humanoid walking started with the development of the biped robot JOHNNIE. This robot was able to realize stable walking with speeds up to 2.4 km h^{-1} and a step length of 55 cm [1]. As JOHNNIEs performance was limited by the mechanical construction a new biped robot called LOLA was developed building on the experience gained with JOHNNIE. On this new robotic platform different research is conducted, e.g. recent studies on walking in uneven terrain with partial footholds [37], on walking in unknown environments with obstacles and disturbances [13] and on computer vision based reconstruction and navigation through unknown environments [42].

The movement of the robot LOLA is controlled based on the data of force sensors in the feet and an Inertia Measurement Unit (IMU) in the upper body. The IMU is mounted in the upper body which is connected to the the lower body with a tube that resembles a human spine. During highly dynamical motion this spine begins to oscillate. As the controller design assumes all parts of the robot to be rigid, the controller is not able to react to the oscillation of the spine and reinforces the oscillations leading to strong vibrations. This mechanism currently limits the maximal performance of the robot.

Therefore, the goal of this thesis is to extend the control system of LOLA, specifically the balance controller, to dampen the vibrations resulting from the structural dynamics of the spine. To do so the model of the inverted pendulum on which the balance controller is based has to be extended by a structural dynamics model. To control this extended model different approaches form the fields of active vibration damping and model based control shall be applied. These controllers are tested in a simulation that models the behavior of the robot to provide a proof of concept for these control approaches. The concept shall be validated using the MBS of LOLA.

In chapter 2 the state of the art of LOLA's controls is displayed. A special focus lies on putting the balance controller into the context of the complete control system. Additionally, some state of the art research on vibration damping is discussed. The structural dynamics model is derived in chapter 3 where also the complete simulation setup including actuator and sensors models is introduced. In this simulation environment different control approaches are tested in chapter 4. In the beginning in section 4.1 the limitations of the previously used balance controller in the simulation with structural dynamics are revealed to motivate the use of more sophisticated control strategies. In section 4.2 approaches from the field of active vibration damping are discussed before model based control structures are examined in section 4.3. At the end of the chapter in section 4.4 the performance of the tested controllers are compared. Afterwards, the most promising control schemes are validated using a Multi-Body Simulation (MBS) of LOLA in chapter 5.

[1] Laufmaschine JOHNNIE.(2020, May 5). Retrieved from https://www.mw.tum.de/am/forschung/abgeschlossene-projekte/humanoide-robotik/johnnie/

Chapter 2

State of the Art

This section outlines the state of the art of the topic. In the beginning the control of the biped robot LOLA is summarized. This section will put the stabilization control, around which this thesis evolves, into context of the control of LOLA and will detail the approach of prior work. Afterwards, basics about oscillating systems are given before some concepts to control such systems are outlined.

2.1 Control of the biped robot LOLA

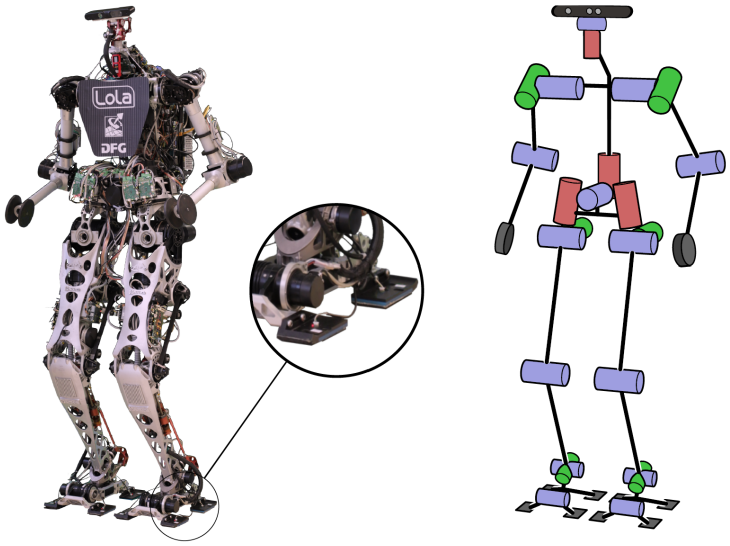

Figure 2.1: LOLA's kinematic chain from [37]

LOLA is a biped robot developed at the Chair of Applied Mechanics at TUM since 2005 and the successor of the prior biped project JOHNNIE. LOLA consists of 24 joints actuated by brushless DC motors with high ratio gearboxes. The robots and its kinematic chain can be seen in fig. 2.1. Each joint contains an absolute as well as an incremental encoder to realize a decentralized position and velocity control of each joint. Joint control with stiff, high ratio gearboxes leads to a high achievable precision in joint control [8]. To obtain the motion of the upper body an IMU is contained in LOLA's torso. The IMU itself consists of an accelerometer and a ring laser gyroscope. LOLA's feet contain digital switches in order to detect ground contact and a 6-axis force/torque sensors to measure the ground reaction forces $\boldsymbol{\lambda}_{f,\mathrm{m}}$ on each foot f. On the head on the robot a depth camera is mounted to get a 3D representation of the robots surroundings. A detailed description of LOLA's mechatronical design can be found in [20].

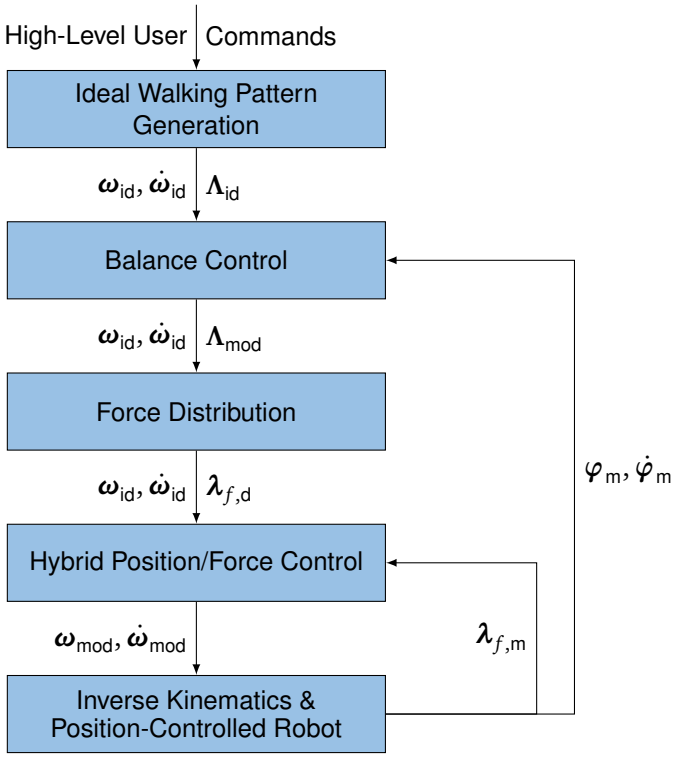

Figure 2.2: Hierarchical Control Scheme of LOLA (modified from [37])

Figure 2.2 shows a simplified schematic of LOLA's control in a hierarchical manner. Based on High-Level User Input i.e. via joy stick an Ideal Walking Pattern Generator creates desired, ideal trajectories $\boldsymbol{\omega}_{id}, \dot{\boldsymbol{\omega}}_{id}$ for the Center of Gravity (CoG) and the feet as well as a ideal ground reaction wrench $\boldsymbol{\Lambda}_{id}$. Afterwards, the Balance Control module modifies the ground reaction forces in order to stabilize the upper body under consideration of the IMU data $\boldsymbol{\varphi}_m, \dot{\boldsymbol{\varphi}}_m$. The modified reaction wrench $\boldsymbol{\Lambda}_{mod}$ is then distributed to the feet using either a heuristic approach or a optimization method (more detailed in [31],[5]). The new desired contact forces and torques $\boldsymbol{\lambda}_{f,d}$ per foot f and the desired trajectories $\boldsymbol{\omega}_{id}, \dot{\boldsymbol{\omega}}_{id}$ are fed into a hybrid position/force controller (details in [6]). Using the measured contact forces and torques $\boldsymbol{\lambda}_{f,m}$ the controller calculates modified trajectories $\boldsymbol{\omega}_{mod}, \dot{\boldsymbol{\omega}}_{mod}$ that are transformed to joint space coordinates using velocity level inverse kinematics. These trajectories in joint space are controlled decentralized for each joint itself. While the other control elements run with a sample time of 1 ms the joint controllers are able to utilize higher local sample rates (50 µs to 100 µs) [38].

The focus of this thesis is the balance controller of the upper body which is further discussed in this section. It is common to model the human balance using the inverted pendulum model for more than twenty years [43]. This model is also used for the stabilization controller of LOLA. The data of the IMU are used to calculate an inclination φ in the frontal plane and an inclination ψ in the sagittal plane of the inverted pendulum. Therefore, the original 3D inverted pendulum can be decomposed in two 2D inverted pendulum models - one in frontal and one in sagittal direction. Two independent controllers calculate an additional torque around the CoG that is necessary to realize the desired torso inclinations and stabilize the upper body. As both the sagittal and frontal systems work analog but for different physical constants the frontal system is treated as a representative in this thesis. In the next sections the inverted pendulum and the corresponding controllers are discussed in detail. It should also be mentioned that previously in the stabilization module the Center of Mass (CoM) height was controlled by modifying the normal forces on the feet, but Sygulla and Rixen [37] suggested including the vertical dynamics of the CoM into the force controller which made this calculation unneeded. Therefore, the CoM control is neglected in this thesis.

Inverted Pendulum Model

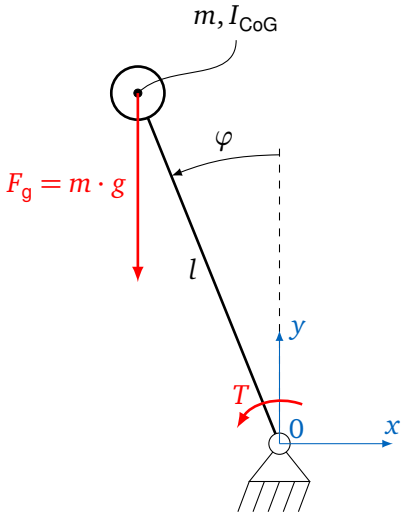

Figure 2.3: Inverted Pendulum Model

The inverted pendulum is a classical control problem used as an example in many fields of control theory, as it is one of the most basic problems that is both nonlinear and unstable. There are also many real world applications that can be modeled as inverted pendulum e.g. Segways. Figure 2.3 shows a schematic of the inverted pendulum variant that is used for the purpose of this thesis. The pendulum is connected to the ground with a rotational joint. This allows the pendulum for one Degree of Freedom (DoF), the angle φ around this joint. The pendulum itself consists of a rigid, massless beam of length l. On top of this beam a body with mass m and moment of inertia I_{CoG} is mounted. This system can be actuated by applying a torque T to the pendulum.

To derive the equations of motion for the inverted pendulum the principle of angular momentum is applied with the rotational joint as reference point. Therefore, the inertia around the joint I_0 is needed and can be calculated using Steiner's Law $I_0 = I_{\text{CoG}} + m \cdot l^2$. The system is affected by the torque T, which represents the control input, and a torque resulting from the gravitational forces T_g. As the lever arm for the gravitational force is proportional to $\sin(\varphi)$ it can be directly seen that this system is nonlinear. The equation of motion of the pendulum derive to:

$$I_0 \ddot{\varphi} = \underbrace{mgl \cdot \sin(\varphi)}_{T_g(\varphi)} + T. \tag{2.1}$$

This equation can be vectorized to obtain a state-space representation of the dynamics of the inverted pendulum:

$$\begin{bmatrix} \dot{\varphi} \\ \ddot{\varphi} \end{bmatrix} = \begin{bmatrix} 0 & 1 \\ 0 & 0 \end{bmatrix} \begin{bmatrix} \varphi \\ \dot{\varphi} \end{bmatrix} + \begin{bmatrix} 0 \\ \frac{1}{I_0} \end{bmatrix} \left(T_g(\varphi) + T \right). \tag{2.2}$$

By linearizing this system around the upright position one can derive a linear dynamics model with one unstable pole in the right half plane:

$$\begin{bmatrix} \dot{\varphi} \\ \ddot{\varphi} \end{bmatrix} = \begin{bmatrix} 0 & 1 \\ \frac{mgl}{I_0} & 0 \end{bmatrix} \begin{bmatrix} \varphi \\ \dot{\varphi} \end{bmatrix} + \begin{bmatrix} 0 \\ \frac{1}{I_0} \end{bmatrix} T. \tag{2.3}$$

PD+ Controller

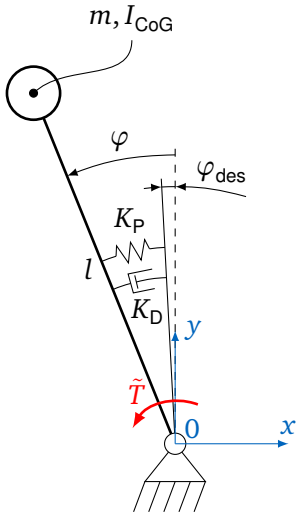

Figure 2.4: PD+ controlled Inverted Pendulum

Rauth [31] derived a controller for this pendulum system by applying an input-output linearization to the nonlinear system from eq. (2.1). The resulting controller is a combination of a standard Proportional-Derivative (PD) controller combined with gravity compensation. The controller is referred to as PD+ controller and the control law is given to be

$$u = K_\mathrm{D}\left(\dot{\varphi}_\mathrm{des} - \dot{\varphi}\right) + K_\mathrm{P}\left(\varphi_\mathrm{des} - \varphi\right) - mgl\sin\left(\varphi\right). \tag{2.4}$$

The last term transforms the system to a double integrator with two poles in zero (assuming perfect measurement) which can be interpreted as inverted pendulum without gravity. This system can be controlled well with a PD controller as the steady state error of the closed-loop system will be zero due to the integrating behavior of the gravity compensated pendulum. The effect of PD controller can be looked at as an addition of a spring and damper to the pendulum. This is illustrated in fig. 2.4. The analogy of this system with the controlled pendulum can be proved by applying the control law of eq. (2.4) to the equations of motion (EoM) in eq. (2.2). The resulting dynamics derive to

$$\begin{aligned}\begin{bmatrix}\dot{\varphi}\\ \ddot{\varphi}\end{bmatrix} &= \begin{bmatrix}0 & 1\\ 0 & 0\end{bmatrix}\begin{bmatrix}\varphi\\ \dot{\varphi}\end{bmatrix} + \begin{bmatrix}0\\ \frac{1}{I_0}\end{bmatrix}\left(K_\mathrm{D}\left(\dot{\varphi}_\mathrm{des} - \dot{\varphi}\right) + K_\mathrm{P}\left(\varphi_\mathrm{des} - \varphi\right)\right)\\ &= \begin{bmatrix}0 & 1\\ -\frac{K_\mathrm{P}}{I_0} & -\frac{K_\mathrm{D}}{I_0}\end{bmatrix}\begin{bmatrix}\varphi\\ \dot{\varphi}\end{bmatrix} + \begin{bmatrix}0\\ 1\end{bmatrix}\underbrace{\left(\frac{K_\mathrm{D}}{I_0}\dot{\varphi}_\mathrm{des} + \frac{K_\mathrm{P}}{I_0}\varphi_\mathrm{des}\right)}_{\tilde{T}}.\end{aligned} \tag{2.5}$$

It can be seen that the corresponding Ordinary Differential Equation (ODE) is equivalent to the EoM of the pendulum in fig. 2.4:

$$\ddot{\varphi} + \frac{K_\mathrm{D}}{I_0}\dot{\varphi} + \frac{K_\mathrm{P}}{I_0}\varphi = \tilde{T}. \tag{2.6}$$

The closed-loop system has the dynamics of a second order system. The corresponding eigenfrequency and damping can be calculated accordingly with the formulas

$$\omega_0 = \sqrt{\frac{K_\mathrm{P}}{I_0}}, \tag{2.7}$$

$$D = \frac{K_\mathrm{D}}{2K_\mathrm{P}}\sqrt{\frac{K_\mathrm{P}}{I_0}}. \tag{2.8}$$

For damping values strictly greater than zero the eigenvalues of the system have a negative real part and therefore, the closed-loop system is asymptotically stable for such damping values ([21, p. 419]). The effect of the (positive) damping on the system and its eigenvalues can be summarized by the following enumeration.

Underdamped:	$0 < D < 0$	$\lambda_{1,2} = a \pm ib$	Oscillation with decaying amplitude (overshoot)
Critically damped:	$D = 1$	$\lambda_{1,2} = a$	No overshoot
Overdamped:	$1 < D$	$\lambda_{1,2} = a \pm b$	No overshoot but slower convergence

By tuning the proportional gain K_P the eigenfrequency can be set whilst influencing the damping simultaneously. By changing the derivative gain K_D the damping can be set arbitrarily for a fixed proportional gain. One goal could be to achieve critical damping in order to obtain a non overshooting and not oscillating behavior with acceptable convergence speed. The proportional gain is desired to be as large as possible to achieve fast convergence.

The influence of the proportional and derivative gain on the eigenvalues can be seen in the Root Locus plot in fig. 2.5. On the left in fig. 2.5a the proportional gain K_P is varied for a fixed derivative gain. For small proportional gains the eigenvalues are both real and negative. By increasing the proportional gain the real part of the eigenvalues is moving together corresponding to higher system dynamics as the slowest pole is getting faster. At a real part of roughly -2 critical damping is reached and the eigenvalues are in the same position. For even higher proportional gains the eigenvalues are complex conjugated and the step response will overshoot. In fig. 2.5b the derivative gain is varied for a fixed proportional gain. Without derivative gain the eigenvalues are purely complex conjugated. For increasing derivative gains the eigenvalues get a negative real part and the imaginary part is decreasing until the eigenvalues reach the real axis corresponding to the critical damping ratio. For increasing gains above this point the eigenvalues stay purely real but one eigenvalue is moving towards zero which corresponds to slow dynamics.

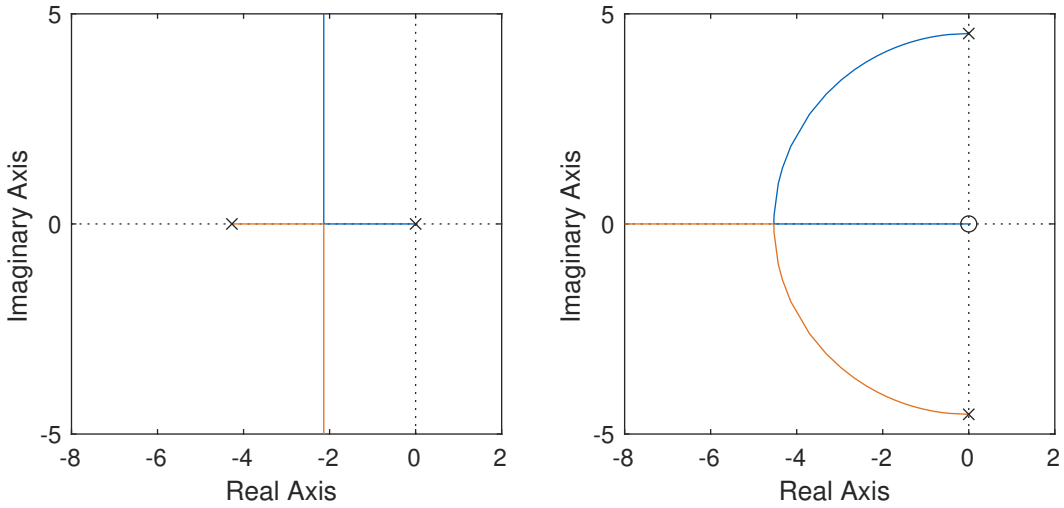

(a) Root Locus varying K_P **(b)** Root Locus varying K_D

Figure 2.5: Root Locus plots for the inverted pendulum controlled by the PD+ controller with the parameters from table 3.2. For the plots one of the parameters is varied

In a real world system these design criteria have to be adopted to the conditions of the real world. First of all, usually one cannot apply arbitrarily large input values as most actuators are limited. Therefore, it is not possible to choose the damping to create critical damping and set the convergence speed with the proportional gain. Secondly, often the angular velocity is noisy and therefore a high derivative gain cannot be used. Also the sampling frequency often does prohibit overly aggressive controllers, as those

can lead to a vibration. Therefore, a compromise has to found and usually the damping ratio is set to $0.4 < D < 0.8$ [21, p. 487].

2.2 Vibration Damping

In the previous section it is shown that the control of LOLA bases on the control of the inverted pendulum. In [39] the model of the inverted pendulum is extended by a flexible model to cope with flexibility in joints and links of a cost-effective humanoid robots like the NAO by Aldebaran Robotics. The model of the inverted pendulum is extended by a second mass that is connected with a spring-damper system to the base of the pendulum. Building on this model a preview controller is used to generate stable walking motions (more detail in [40]). By including the flexibility of the robot like this, a stable walk with cost-effective robots was enabled.

Although the idea of including a model for flexibility is similar to the idea of this thesis, LOLA is no cost-effective robot and only the flexibility of the spine shall be modeled. Thus, a different model extension has to be used in this thesis. Instead of an additional mass on the base, the dynamics of the inverted pendulum shall be extended to an elastic beam and therefore, different control approaches of flexible links and beams are displayed in the following.

Positive Position Feedback

Positive Position Feedback is a common vibration control method for flexible beams that are equipped with strain actuators and sensors in collocated configuration [27, p. 101]. The idea is to use a second-order filter with eigenfrequency ω_f and damping D_f to improve the roll-off of the control system. The transfer function of the strain sensor output y to the strain actuator input u is given by

$$G_{\mathrm{PPF}}(s) = \frac{Y(s)}{U(s)} = \frac{g\,\omega_\mathrm{f}^2}{s^2 + 2D_\mathrm{f}\omega_\mathrm{f}s + \omega_\mathrm{f}^2}. \tag{2.9}$$

This approach was first introduced by [11] to overcome the instabilities due to limited actor dynamics. It was proven that the control algorithm cannot be destabilized by such actor dynamics [11]. Positive Position Feedback is able to control multiple resonance frequencies while still being insensitive to spillover effects from uncontrolled flexible modes [10]. In [9] the feasibility of Positive Position Feedback was shown and experiments were conducted on a flexible beam with one or two sets of collocated piezoelectric sensors and actuators where up to six structural modes were controlled simultaneously. The robustness of Positive Position Feedback against parameter changes was investigated by [36] on a flexible aluminum cantilever beam with the result that single-mode vibration suppression as well as multiple-mode vibration suppression is robust against changes in the natural frequency.

Different research has been done on adaptive Positive Position Feedback to compensate for changing resonance frequencies of the structure. In [4] the Positive Position Feedback is formulated in uncoupled modal coordinates and the parameters of the Positive Position Feedback controller are adapted leading to an Adaptive Model Positive Position Feedback (AMPPF). The parameters are adapted such that the system follows the behavior of an optimal reference model. The stability of the adaption law is proven with Lyapunov theorems and the effectiveness of the resulting controller was shown in experiments with a cantilever beam. In [25] a recursive least-squares method is used to estimate the natural frequencies of the plant, which are used to calculate the Positive Position Feedback controller. Additionally PD control and input shaping is used to control a flexible beam.

Resonant controller

The Positive Position Feedback controller can be adjusted to work not with a strain sensor but with an acceleration feedback. The transfer function of the controller is the same as for the Positive Position Feedback but instead of collocated strain sensors/actors collocated acceleration sensors and force actuators are used. This control setup is called resonant controller [1]. In [34] it was proven that this controller is unconditionally stable (for collocated pairs) and experiments with a flexible beam were conducted which resulted in a improved vibration damping. The robustness of this controller was investigated in [28] with the result that the controller is only effective for exact tuning on the natural frequencies and that closely spaced resonance frequencies cannot be damped strongly.

In [29] this control law was applied to a non-collocated system. Experiments were conducted on a rotating beam that is driven by a AC motor with an acceleration sensor on the tip of the beam. In the experiments the vibration of the tip of the beam was significantly decreased by using the resonant controller. Therefore, Qiu reasons that the acceleration feedback with resonant controllers do work effectively for collocated or nearly collocated systems.

Notch Filters

Another approach for non-collocated sensor/actor pairs is the use of Notch Filters. In [33] a notch filter was used to reduce the oscillations of dual inertia spring system. The effectiveness of the notch filter was proven with an experimental setup. Notch Filters were used to dampen the vibration of a flexible beam in [14] and by doing so the settling time was reduced by 45 %.

State Feedback Control

It is possible to realize the control of flexible structures via state feedback and additional observers. In [3] a combination of linear state feedback and of a Luenberger state estimator was developed. The continuous structure was discretised to N nodes which were controlled by the state feedback. One advantage of this approach is that multiple nodes can be controlled with only a few actuators which do not need to be collocated with the sensors as long as the system fulfills the controllability and observability condition. The effect of uncontrolled, residual modes of this control system were investigated in [2] with the result that spillover effects can lead to closed-loop instabilities especially for residual modes with small stability margins. In [7] a state feedback controller for active vibration damping is design via pole-placement and tested on a one-link robot arm with the conclusion that in this configuration the spillover problem presents no significant practical problem.

A special kind of observer and state feedback combination is the combination of a linear Kalman Filter with a Linear Quadratic Regulator which is referred to as Linear-Quadratic-Gaussian (LQG) regulator [22, p. 375]. This approach was applied to a 2-mass system with flexible linkage in [17] where the torsional vibration was damped significantly.

Passive and Semi-Active Vibration Damping

For the sake of completeness the reader is referred to the fields of passive and semi-active vibration control. The idea is to use physical components with fixed (passive) or tunable (semi-active) physical properties. Approaches from these fields are often heavier for comparable performance than active solutions and active vibration control may offer better maximal performance [27, p. 5].

In this thesis the vibration damping approaches are applied to LOLA's balance controller. The control algorithms are designed and tested in a MATLAB SIMULINK simulation which includes a model of the flexible inverted pendulum. The resulting controllers are validated in a MBS of the robot LOLA.

Chapter 3

Simulation Setup

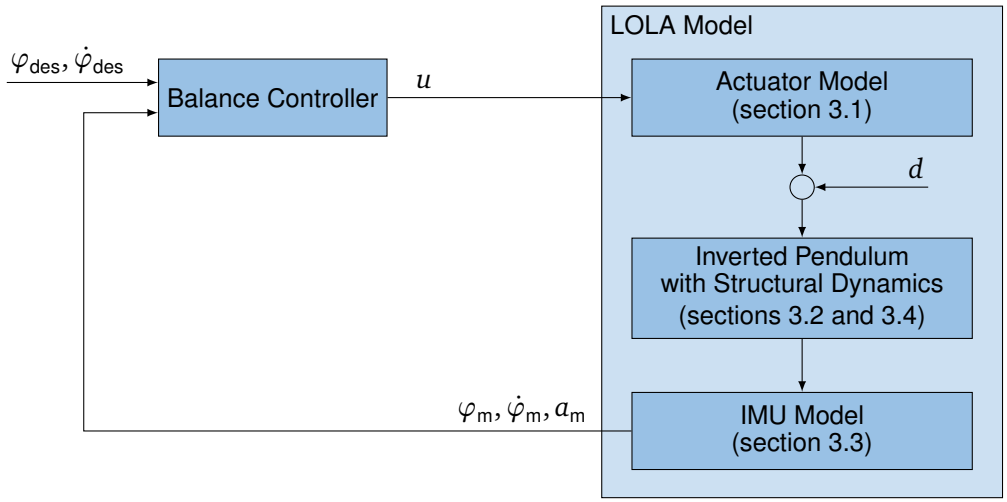

Figure 3.1: Scheme of the Simulation used for this thesis

This thesis bases on a simulation of an extended model of LOLA that includes structural dynamics. The setup of this simulation which is implemented using MATLAB SIMULINK can be seen in fig. 3.1. First the input signal generated by the balance controller is fed into an actuator model which emulates the behavior of the hybrid position/force controller. Afterwards, disturbance d is added to the signal which forms the input of the inverted pendulum model. To model the structural dynamics of LOLA's spine this model is extended in a way that enables oscillation. A model of the IMU which incorporates noise and quantization feeds the measured data - φ_m, $\dot{\varphi}_m$ and a_m - back into the balance controller. This simulation is covered in sections 3.1 to 3.4 before the performance of the previously used PD+ controller on this extended LOLA model is discussed. The goal of this simulation is not to create a perfect LOLA model but to approximately recreate the behavior and make a proof of concept for the control strategies.

3.1 Actuator Model

On Lola, the balance controller calculates a control input torque u to stabilize the upper body of the robot. This torque has to be realized by the extremities. It is distributed to the feet before calculating desired joint angles with the hybrid position/force controller which are then controlled in each joint separately. This process has a trailing behavior which can be modeled using a first order lag (see [31]). Furthermore, only a finite torque can be realized. To model this behavior in the simulation the input signal u is limited to values in the range of $[-T_{max}; T_{max}]$ before being filtered with a first order transfer function with time

constant T_{act} which is illustrated in fig. 3.2. The saturation of the input introduces the second nonlinearity along with the sinusoidal term of the torque created by gravity.

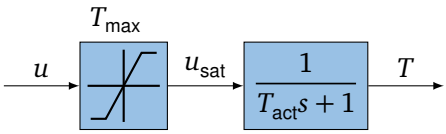

Figure 3.2: Actuator model used for the simulation

3.2 Structural Dynamics Model

LOLA was previously modeled as an inverted pendulum which does not enable vibration due to structural dynamics. Therefore, in this section a structural dynamics model is introduced before merging this model with the inverted pendulum.

For the sake of simplicity the structural dynamics can be approximated by a transfer function $G_s(s)$ filtering the angle of the ideal, rigid pendulum. This filter adds resonance and antiresonance frequencies leading to a simplified structural dynamics model. It consists of multiple elements, where every element models one pair of resonance and anti-resonance frequencies. The transfer function $G_e(s)$ of one element is given to:

$$G_e(s) = \frac{\frac{1}{\omega_z^2}s^2 + \frac{2D_z}{\omega_z}s + 1}{\frac{1}{\omega_p^2}s^2 + \frac{2D_p}{\omega_p}s + 1}. \tag{3.1}$$

The static gain of the transfer function is consciously chosen to one to fit the desire that the structural dynamics are not engaged for low dynamical motion. Each of these elements has four parameters. The natural frequencies of the poles ω_p and of the zeros ω_z as well as the two dimensionless damping ratios D_p and D_z. The damped resonance frequencies of the poles and zeros $f_{d,p/z}$ can be calculated based on the natural frequencies and damping ratios as follows:

$$f_{d,p/z} = \frac{1}{2\pi}\omega_{d,p/z} = \frac{1}{2\pi}\omega_{p/z}\sqrt{1-D_{p/z}^2}. \tag{3.2}$$

The parameterization of these parameters is discussed in section 3.4 where the simulation output is tuned to match the real world behavior of LOLA.

To model n eigenfrequencies n of these elements are stringed together. This leads to the transfer function of the structural dynamics $G_s(s)$ which is given by:

$$G_s(s) = \frac{Y_s(s)}{U_s(s)} = \prod_{i=1}^{n} G_{e,i} = \frac{b_{2n}s^{2n} + b_{2n-1}s^{2n-1} + ... + b_1 s + b_0}{s^{2n} + a_{2n-1}s^{2n-1} + ... + a_1 s + a_0}. \tag{3.3}$$

Using formulas provided in [21, p. 159] this transfer function can be brought to Controllable Canonical Form (CCF) which results in the following state-space model:

$$\dot{\boldsymbol{x}}_s = \begin{bmatrix} 0 & 1 & 0 & \cdots & 0 \\ \vdots & \ddots & \ddots & \ddots & 0 \\ 0 & \cdots & 0 & \ddots & 1 \\ -a_0 & \cdots & \cdots & \cdots & -a_{2n-1} \end{bmatrix} \boldsymbol{x}_s + \begin{bmatrix} 0 \\ \vdots \\ 0 \\ 1 \end{bmatrix} u_s, \tag{3.4}$$

$$y_s = \begin{bmatrix} (b_0 - b_{2n}a_0) & (b_1 - b_{2n}a_1) & \ldots & (b_{2n-1} - b_{2n}a_{2n-1}) \end{bmatrix} \boldsymbol{x}_s + b_{2n}u_s. \tag{3.5}$$

This state-space model is not well conditioned as $a_0 = \prod_{i=1}^{n} \omega_{\mathrm{p},i}^2 >> 1$. This high difference between the largest and smallest entry in the matrix can cause numerical problems. Therefore, another formulation has to be found. Instead of formulating one combined transfer function for all the elements and transforming it to a state-space model, one can formulate a single element in state-space form and then string those state-space models together. To fit the CCF conditions the transfer function is reformulated:

$$G_{\mathrm{e},i}(s) = \frac{\frac{1}{\omega_{\mathrm{z},i}^2}s^2 + \frac{2D_{\mathrm{z},i}}{\omega_{\mathrm{z},i}}s + 1}{\frac{1}{\omega_{\mathrm{p},i}^2}s^2 + \frac{2D_{\mathrm{p},i}}{\omega_{\mathrm{p},i}}s + 1} = \frac{\frac{\omega_{\mathrm{p},i}^2}{\omega_{\mathrm{z},i}^2}s^2 + \frac{2D_{\mathrm{z},i}\omega_{\mathrm{p},i}^2}{\omega_{\mathrm{z},i}}s + \omega_{\mathrm{p},i}^2}{s^2 + 2D_{\mathrm{p},i}\omega_{\mathrm{p},i}s + \omega_{\mathrm{p},i}^2}. \tag{3.6}$$

This transfer function is brought to CCF:

$$\dot{\boldsymbol{x}}_{\mathrm{e},i} = \underbrace{\begin{bmatrix} 0 & 1 \\ -\omega_{\mathrm{p},i}^2 & -2D_{\mathrm{p},i}\omega_{\mathrm{p},i} \end{bmatrix}}_{\boldsymbol{A}_{\mathrm{e},i}} \boldsymbol{x}_{\mathrm{e},i} + \underbrace{\begin{bmatrix} 0 \\ 1 \end{bmatrix}}_{\boldsymbol{b}_{\mathrm{e}}} u_{\mathrm{e},i}, \tag{3.7}$$

$$y_{\mathrm{e},i} = \underbrace{\begin{bmatrix} \omega_{\mathrm{p},i}^2\left(1 - \frac{\omega_{\mathrm{p},i}^2}{\omega_{\mathrm{z},i}^2}\right) & 2\frac{\omega_{\mathrm{p},i}^2}{\omega_{\mathrm{z},i}^2}\left(D_{\mathrm{z},i} - D_{\mathrm{p},i}\frac{\omega_{\mathrm{p},i}}{\omega_{\mathrm{z},i}}\right) \end{bmatrix}}_{\boldsymbol{c}_{\mathrm{e},i}} \boldsymbol{x}_{\mathrm{e},i} + \underbrace{\begin{bmatrix} \frac{\omega_{\mathrm{p},i}^2}{\omega_{\mathrm{z},i}^2} \end{bmatrix}}_{d_{\mathrm{e},i}} u_{\mathrm{e},i}. \tag{3.8}$$

The first element is excited by the angle of the pendulum φ, which is the input of the overall structure model. The input of every following element $u_{\mathrm{e},i}$ is the output of the previous element $y_{\mathrm{e},n-1}$ which leads to the following relations:

$$\begin{aligned}
u_{\mathrm{e},1} &= u_{\mathrm{s}} = \varphi, \\
u_{\mathrm{e},2} &= y_{\mathrm{e},1} = \boldsymbol{c}_{\mathrm{e},1}\boldsymbol{x}_{\mathrm{e},1} + d_{\mathrm{e},1}u_{\mathrm{s}}, \\
u_{\mathrm{e},3} &= y_{\mathrm{e},2} = \boldsymbol{c}_{\mathrm{e},2}\boldsymbol{x}_{\mathrm{e},2} + d_{\mathrm{e},2}\boldsymbol{c}_{\mathrm{e},1}\boldsymbol{x}_{\mathrm{e},1} + d_{\mathrm{e},2}d_{\mathrm{e},1}u_{\mathrm{s}}, \\
&\vdots \\
u_{\mathrm{e},n} &= y_{\mathrm{e},n-1} = \boldsymbol{c}_{\mathrm{e},n-1}\boldsymbol{x}_{\mathrm{e},n-1} + \sum_{i=1}^{n-2}\left(\prod_{j=i+1}^{n-1} d_j\right)\boldsymbol{c}_{\mathrm{e},i}\boldsymbol{x}_{\mathrm{e},i} + \left(\prod_{i=1}^{n-1} d_i\right)u_{\mathrm{s}}.
\end{aligned}$$

It is possible to stack the state vectors of each of the elements and obtain a state-space description of the complete structure where the input u_{s} is equal to the angle of the inverted pendulum φ and the output y_{s} equals the output of the last element $y_{\mathrm{e},n}$:

$$\dot{\boldsymbol{x}}_{\mathrm{s}} = \underbrace{\begin{bmatrix} \boldsymbol{A}_{\mathrm{e},1} & & & \\ \boldsymbol{b}_{\mathrm{e}}\boldsymbol{c}_{\mathrm{e},1} & \boldsymbol{A}_{\mathrm{e},2} & & \\ d_{\mathrm{e},2}\boldsymbol{b}_{\mathrm{e}}\boldsymbol{c}_{\mathrm{e},1} & \boldsymbol{b}_{\mathrm{e}}\boldsymbol{c}_{\mathrm{e},2} & \boldsymbol{A}_{\mathrm{e},3} & \\ \vdots & & \ddots & \ddots \\ \prod_{i=2}^{n-1} d_{\mathrm{e},i}\boldsymbol{b}_{\mathrm{e}}\boldsymbol{c}_{\mathrm{e},1} & \cdots\cdots & \boldsymbol{b}_{\mathrm{e}}\boldsymbol{c}_{\mathrm{e},n-1} & \boldsymbol{A}_{\mathrm{e},n} \end{bmatrix}}_{\boldsymbol{A}_{\mathrm{s}}} \underbrace{\begin{bmatrix} \boldsymbol{x}_{\mathrm{e},1} \\ \boldsymbol{x}_{\mathrm{e},2} \\ \boldsymbol{x}_{\mathrm{e},3} \\ \vdots \\ \boldsymbol{x}_{\mathrm{e},n} \end{bmatrix}}_{\boldsymbol{x}_{\mathrm{s}}} + \underbrace{\begin{bmatrix} \boldsymbol{b}_{\mathrm{e}} \\ \boldsymbol{0} \\ \vdots \\ \boldsymbol{0} \end{bmatrix}}_{\boldsymbol{b}_{\mathrm{s}}} u_{\mathrm{s}}, \tag{3.9}$$

$$y_{\mathrm{s}} = y_{\mathrm{e},n} = \underbrace{\begin{bmatrix} \left(\prod_{i=2}^{n} d_i\right)\boldsymbol{c}_{\mathrm{e},1} & \ldots & d_n d_{n-1}\boldsymbol{c}_{\mathrm{e},n-2} & d_n\boldsymbol{c}_{\mathrm{e},n-1} & \boldsymbol{c}_{\mathrm{e},n} \end{bmatrix}}_{\boldsymbol{c}_{\mathrm{s}}} \boldsymbol{x}_{\mathrm{s}} + \underbrace{\begin{bmatrix} \prod_{i=1}^{n-1} d_i \end{bmatrix}}_{d_{\mathrm{s}}} u_{\mathrm{s}}. \tag{3.10}$$

In comparison to the prior model using the CCF of the complete structure the elements of this matrix are concentrated close to the diagonal. The largest entry is smaller with a value of ω_n^2. The condition number of this matrix is significantly improved (for the parameters from table 3.2 it improved from 3.99×10^{11} to 9.80×10^{3}).

The dynamics of the structure from eqs. (3.9) and (3.10) can be combined with the dynamics of the inverted pendulum from eq. (2.2) to obtain a state-space model for the complete system:

$$\dot{\boldsymbol{x}} = \underbrace{\left[\begin{array}{cc|ccc} 0 & 1 & 0 & \dots & 0 \\ 0 & 0 & 0 & \dots & 0 \\ \hline & & & & \\ \boldsymbol{b}_\mathrm{s} & \boldsymbol{0} & & \boldsymbol{A}_\mathrm{s} & \\ & & & & \end{array}\right]}_{\boldsymbol{A}} \underbrace{\left[\begin{array}{c} \varphi \\ \dot{\varphi} \\ \hline \\ \boldsymbol{x}_\mathrm{s} \\ \\ \end{array}\right]}_{\boldsymbol{x}} + \underbrace{\left[\begin{array}{c} 0 \\ \frac{1}{I_0} \\ \hline \\ \boldsymbol{0} \\ \\ \end{array}\right]}_{\boldsymbol{b}} \left(T + T_\mathrm{g}(\varphi)\right). \tag{3.11}$$

3.3 Sensor Model

The IMU is mounted in the upper body of LOLA and thus, effected by the structural dynamics of the spine. The sensor module returns three signals for each the frontal and sagittal plane. For the frontal plane those signals are the inclination angle φ_m and the angular velocity a_m in the IMU coordinate frame. In the simulation the structural dynamics are modeled using a filter which returns an angle affected by structural dynamics and subsequently the output of this filter is used to model the IMU output. Additionally noise and quantization is modeled in the simulation which will be discussed after introducing the equations for the ideal sensor.

The first sensor output φ_m corresponds to the angle of the upper body and thus, can be modeled directly with the output of the structural dynamics filter:

$$\varphi_\mathrm{m} = y_\mathrm{s} = \boldsymbol{c}_\mathrm{s}\boldsymbol{x}_\mathrm{s} + d_\mathrm{s}u_\mathrm{s} = \begin{bmatrix} d_\mathrm{s} & 0 & \boldsymbol{c}_\mathrm{s} \end{bmatrix}\boldsymbol{x}. \tag{3.12}$$

The second output $\dot{\varphi}_\mathrm{m}$ models the measurement of the angular velocity and is modeled by taking the derivative of the first sensor output:

$$\dot{\varphi}_\mathrm{m} = \dot{y}_\mathrm{s} = \boldsymbol{c}_\mathrm{s}(\boldsymbol{A}_\mathrm{s}\boldsymbol{x}_\mathrm{s} + \boldsymbol{b}_\mathrm{s}u_\mathrm{s}) + d_\mathrm{s}\dot{u}_\mathrm{s} = \begin{bmatrix} \boldsymbol{c}_\mathrm{s}\boldsymbol{b}_\mathrm{s} & d_\mathrm{s} & \boldsymbol{c}_\mathrm{s}\boldsymbol{A}_\mathrm{s} \end{bmatrix}\boldsymbol{x}. \tag{3.13}$$

The last sensor output a_m models the acceleration of the IMU in the frontal plane in its own coordinate system. The acceleration can be calculated by multiplying the angular acceleration $\ddot{\varphi}_\mathrm{m}$ with the length of the pendulum l which yields:

$$\begin{aligned} a_\mathrm{m} &= l\ddot{y}_\mathrm{s} = l\boldsymbol{c}_\mathrm{s}\boldsymbol{A}_\mathrm{s}(\boldsymbol{A}_\mathrm{s}\boldsymbol{x}_\mathrm{s} + \boldsymbol{b}_\mathrm{s}u_\mathrm{s}) + l\boldsymbol{c}_\mathrm{s}\boldsymbol{b}_\mathrm{s}\dot{u}_\mathrm{s} + ld_\mathrm{s}\ddot{u}_\mathrm{s} = \\ &= \begin{bmatrix} l\boldsymbol{c}_\mathrm{s}\boldsymbol{A}_\mathrm{s}\boldsymbol{b}_\mathrm{s} & l\boldsymbol{c}_\mathrm{s}\boldsymbol{b}_\mathrm{s} & l\boldsymbol{c}_\mathrm{s}\boldsymbol{A}_\mathrm{s}^2 \end{bmatrix}\boldsymbol{x} + d_\mathrm{s}\frac{l}{I_0}\left(T + T_\mathrm{g}(\varphi)\right). \end{aligned} \tag{3.14}$$

These output equations can be summarized to form an output equation to the vectorized dynamics:

$$\boldsymbol{y} = \underbrace{\left[\begin{array}{cc|c} d_\mathrm{s} & 0 & \boldsymbol{c}_\mathrm{s} \\ \boldsymbol{c}_\mathrm{s}\boldsymbol{b}_\mathrm{s} & d_\mathrm{s} & \boldsymbol{c}_\mathrm{s}\boldsymbol{A}_\mathrm{s} \\ l\boldsymbol{c}_\mathrm{s}\boldsymbol{A}_\mathrm{s}\boldsymbol{b}_\mathrm{s} & l\boldsymbol{c}_\mathrm{s}\boldsymbol{b}_\mathrm{s} & l\boldsymbol{c}_\mathrm{s}\boldsymbol{A}_\mathrm{s}^2 \end{array}\right]}_{\boldsymbol{C}} \boldsymbol{x} + \underbrace{\begin{bmatrix} 0 \\ 0 \\ d_\mathrm{s}\frac{l}{I_0} \end{bmatrix}}_{\boldsymbol{d}} \left(T + T_\mathrm{g}(\varphi)\right). \tag{3.15}$$

It can be seen that the acceleration a_m is not linear in the state vector $\boldsymbol{x}$ as the torque T_g due to the gravity depends nonlinearly from the rigid pendulum angle φ. A first order Taylor expansion yields $T_\mathrm{g} \approx mgl\varphi$ and the linearized dynamics derive to:

$$\boldsymbol{y} \approx \underbrace{\left[\begin{array}{cc|c} d_\mathrm{s} & 0 & \boldsymbol{c}_\mathrm{s} \\ \boldsymbol{c}_\mathrm{s}\boldsymbol{b}_\mathrm{s} & d_\mathrm{s} & \boldsymbol{c}_\mathrm{s}\boldsymbol{A}_\mathrm{s} \\ l\boldsymbol{c}_\mathrm{s}\boldsymbol{A}_\mathrm{s}\boldsymbol{b}_\mathrm{s} + d_\mathrm{s}\frac{mgl^2}{I_0} & l\boldsymbol{c}_\mathrm{s}\boldsymbol{b}_\mathrm{s} & l\boldsymbol{c}_\mathrm{s}\boldsymbol{A}_\mathrm{s}^2 \end{array}\right]}_{\boldsymbol{C}_\mathrm{lin}} \boldsymbol{x} + \begin{bmatrix} 0 \\ 0 \\ d_\mathrm{s}\frac{l}{I_0} \end{bmatrix} T. \tag{3.16}$$

In the simulation sensor noise and quantization are also modeled. The parameters of both models are approximated under use of real world sensor data from a scenario where the robot was standing upright without motion for approximately two seconds. Figure 3.3 displays the chronological sequence of the sensor output from this scenario. In each subplot the first 1.6 s are enlarged to see the signal range used to determine the quantization and noise. It can be seen that the first output containing information about the angle φ is mainly affected by the quantization and less by noise which is plausible as the angle is not directly measured but calculated using an integration which reduces the noise on the signal. Furthermore, it can be noticed that the angle is defined differently in the measured data and in this thesis (see fig. 2.3). In this thesis the upright position corresponds to an angle of 0° as this is the more intuitive definition whilst in the experimental data the upright position is defined by an angle 90°. In contrast to the first subplot, the quantization interval is not clearly visible in the second and third subplot of the figure. It can be seen that the noise on the signals is larger than the quantization interval.

The quantization intervals are derived by taking the smallest difference between two consecutive data points from each signal of fig. 3.3. To validate the approximated quantization interval for each sensor signal the Mean Relative Error (MRE) is calculated for the error between every data point and the closest multiple of the quantization interval relative to the latter. Equation (3.17) displays the calculation of this error for a sensor signal y_i with n data points and the approximated quantization interval Δ_i. The calculated quantization intervals and the corresponding errors are displayed in table 3.1. It can be seen that the MRE is below 1 % for the angular velocity and the accelerations. For the angle the error is significantly higher but is considered sufficiently low, as the focus of this thesis is to prove the general concept and not to model the system as accurately as possible. Additionally the simplifications due to the inverted pendulum assumption and the actor dynamics outweigh the effect of the quantization.

$$MRE_i = \frac{1}{n}\sum_{j=0}^{n}(y_i[j]/\Delta_i - \lceil (y_i[j]/\Delta_i) - 0.5)\rceil) \tag{3.17}$$

In the simulation the noise is modeled as additive white Gaussian noise. The variance of this noise V_i is parameterized with the variance of the first N samples corresponding to 1.6 s of the data y_i from fig. 3.3. The formula to calculate the variance can be seen in eq. (3.18). Table 3.1 contains the calculated variances.

$$V_i = \frac{1}{N-1}\sum_{j=1}^{N}(y_i[j]-\mu_i)^2 \qquad \text{where} \qquad \mu_i = \frac{1}{N}\sum_{j=1}^{N} y_i[j] \tag{3.18}$$

Table 3.1: Parameters of the sensor model

Sensor signal (y_i)	Quantization (Δ_i)	MRE_i	Noise variance
φ_m	1.7453×10^{-4} rad	15.087 %	5.7245×10^{-9} rad
$\dot{\varphi}_\mathrm{m}$	1.0000×10^{-12} rad s^{-1}	0.8154 %	1.3231×10^{-6} rad s^{-1}
a_m	1.0000×10^{-5} m s^{-2}	1.1905×10^{-12}	1.6849×10^{-3} m^2 s^{-4}

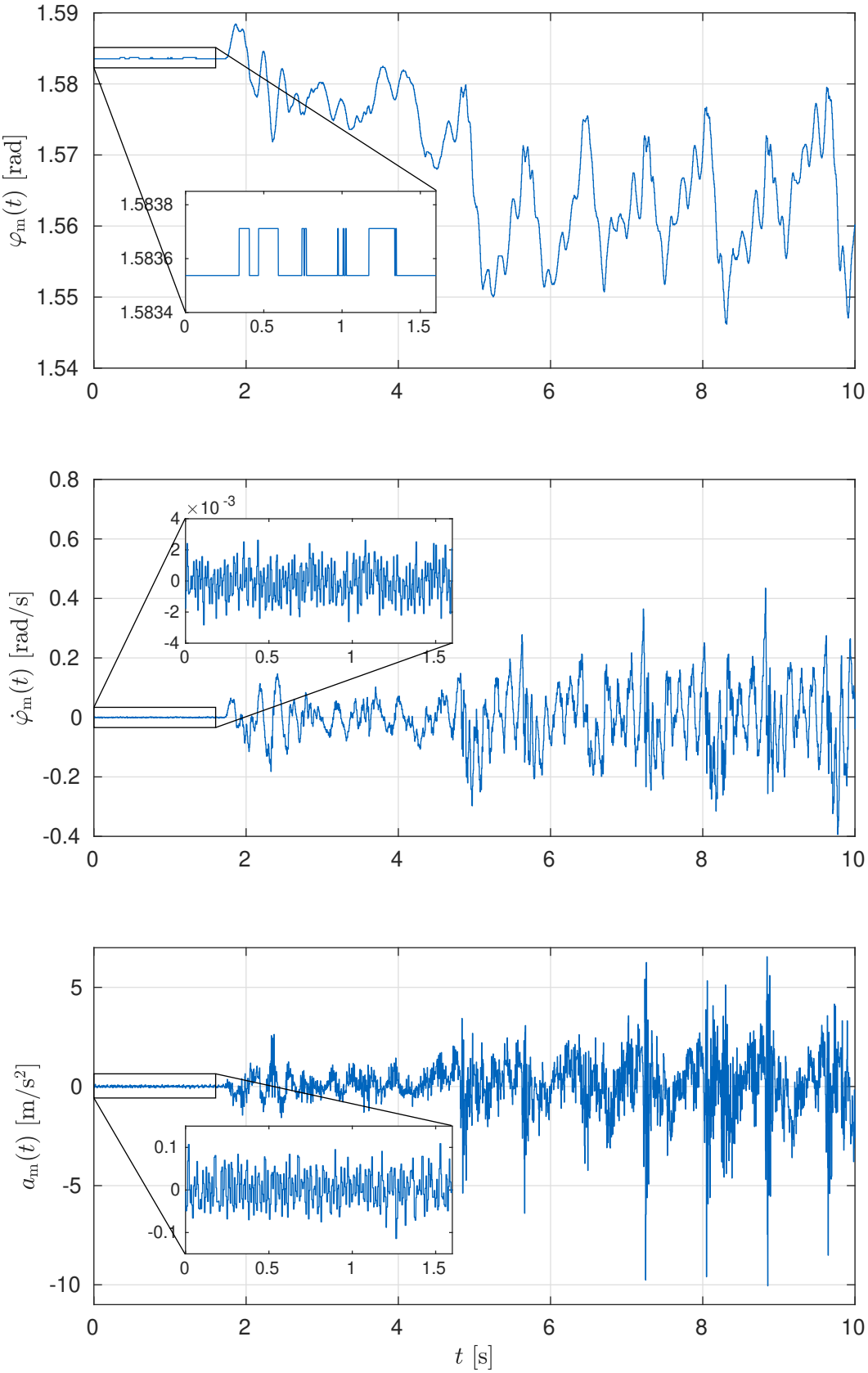

Figure 3.3: Sensor data from an experiment with LOLA

3.4 Parameterization of Simulation Model

In this section the parameter values of the simulation model are determined. Table 3.2 contains all parameters with their values which are used in the simulation. The physical parameters of the inverted pendulum, the actuator model parameter and the PD+ controller gains are adopted from [31]. The damped resonance and anti-resonance frequencies are given as they were determined from an eigenfrequency analysis experiment prior to this thesis. To each of these frequencies a corresponding damping coefficient is needed. Those damping values are set using a trial and error approach. The goal is to model the behavior visible at the robot LOLA when being controlled with the PD+ controller. For the gains used in the real application no oscillation should be visible in the angle while the angular velocity contain vibrations due to the structure with a decreasing amplitude. The first resonance should dominate the other, higher resonance frequencies.

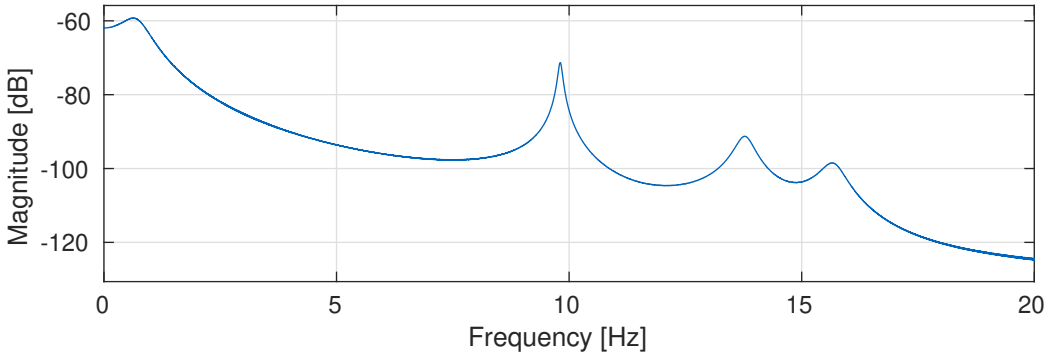

Figure 3.4: Identified disturbance transfer function $G_\mathrm{d}(s)$ for the simulation with the PD+ controller

Figure 3.4 shows the identified disturbance transfer function from the disturbance d to the output angle y_1 for the simulation with the parameters from table 3.2. More information on the identification of the transfer function can be found in section 3.5. In the figure it can be seen that the peak with the highest magnitude is at around 0.7 Hz and originates from the inverted pendulum dynamics. The structural dynamics cause three additional peaks that have a lower magnitude than the first one. The first structure peak has a higher magnitude than the higher resonance frequencies and subsequently is dominating the structure.

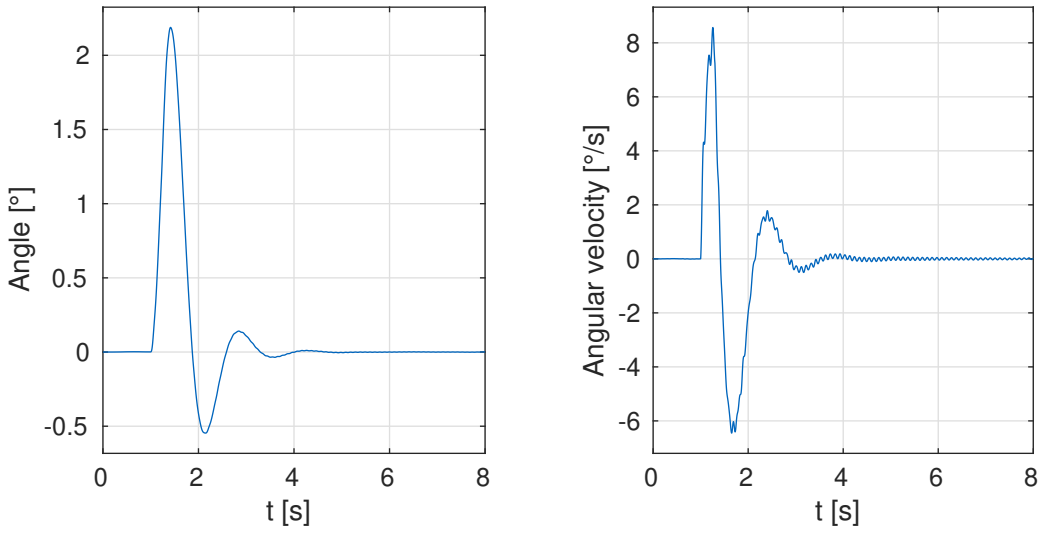

Figure 3.5: Disturbance impulse response of the simulation with the PD+ controller

The response to a disturbance impulse is displayed in fig. 3.5. On the left side the resulting angle y_1 can be seen. The system is excited at 1 s and deviates more than 2° before oscillating around to the initial position with decreasing amplitude. In the angle there is barely any vibration in the structure visible. The angular velocity on the right side on the contrary does also contain a visible vibration of the structure with decaying amplitude.

Table 3.2: Parameters used for the simulations. First section contains physical parameters of the inverted pendulum, the second part displays the structural dynamics model parameters and the actuator model parameters. Lastly the controller gains are displayed

Parameter	Value	Description
g	9.81 m s^{-1}	Gravity Constant
m	60.885 kg	Mass of the pendulum
l	0.9 m	Length of the pendulum
I_{CoG}	10.66 kg m^2	Moment of inertia around the
$f_{\mathrm{d,p}}$	[9.8 Hz, 13.8 Hz, 15.7 Hz]	Resonance frequencies
D_{p}	[0.015, 0.015, 0.015]	Damping of the resonances
$f_{\mathrm{d,z}}$	[11 Hz, 14.6 Hz, 16.5 Hz]	Anti-resonance frequencies
D_{z}	[0.015, 0.015, 0.015]	Damping of the anti-resonances
T_{max}	120 N m	Maximum torque by the actuator
T_{act}	0.035 s	Actuator time constant
K_{P}	1250	Proportional Gain of the PD+ Controller
K_{D}	260	Derivative Gain of the PD+ Controller

The parameterized model can be linearized around the upright position which leads to $\sin(\varphi) \approx \varphi$ and $u_{\mathrm{sat}} \approx u$. The poles and zeros of the linearized open-loop system are displayed in a pole-zero plot in fig. 3.6. The pole on the left at -28.5 resembles the dynamics of the actuator model and as this pole has a larger negative real part and is faster does not contribute to the system dynamics significantly. The three complex conjugated poles and zeros represent the structural dynamics. The two poles on the real axis that are symmetrical to the imaginary axis result from the inverted pendulum dynamics. As one of these poles is in the right side of the complex plane one can directly see that this system is unstable.

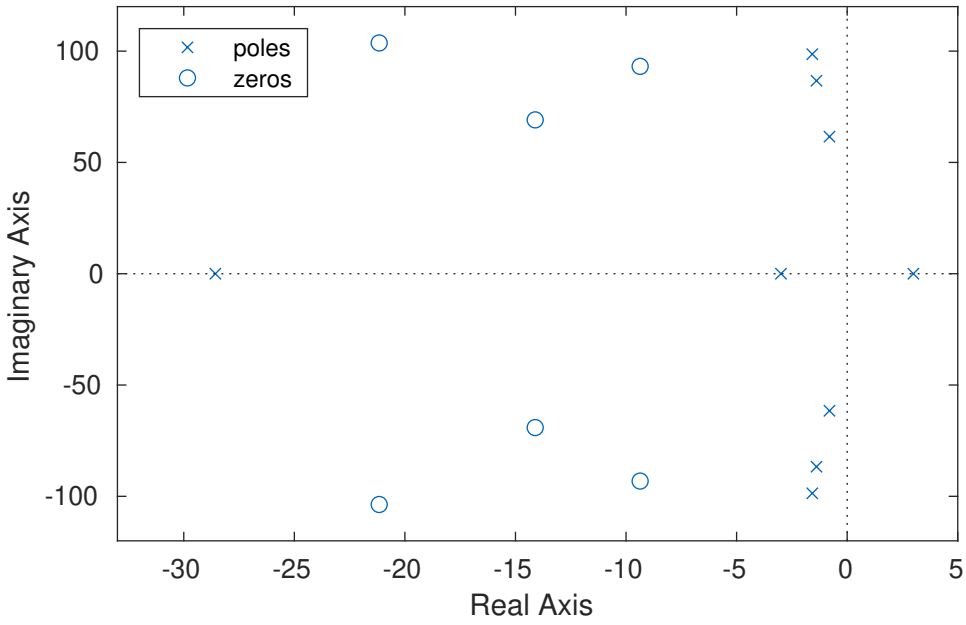

Figure 3.6: Poles and zeros of the linearized LOLA model

3.5 Performance Measures for the Closed-Loop System

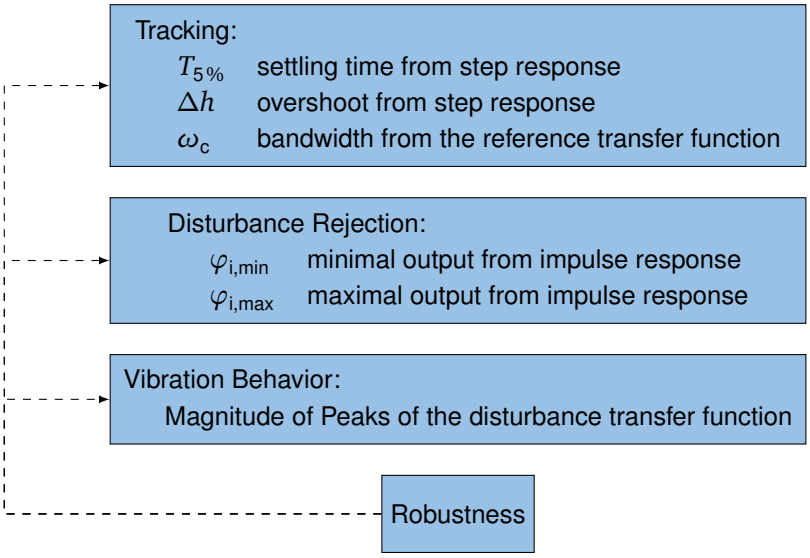

Figure 3.7: Performance measures to quantify the performance of a control scheme

After stating the complete simulation environment this section will elaborate on measures to evaluate the closed-loop performance of each control setup. In general the controlled system is supposed to track the desired trajectory well and reject disturbances whilst preventing vibrations. Additionally the parameters vary in LOLA's application so the closed-loop is desired to be robust to parameter changes. To quantify the performance in these areas the step response, disturbance impulse response and the identified transfer functions from desired angle to output and from disturbance to output are used. Figure 3.7 illustrates the design goals and the indicators to quantify them. To analyze the robustness one can vary the parameters of the system and track at the changes of the performance indicators. In the following all indicators are discussed in detail with the corresponding plots.

Step Response

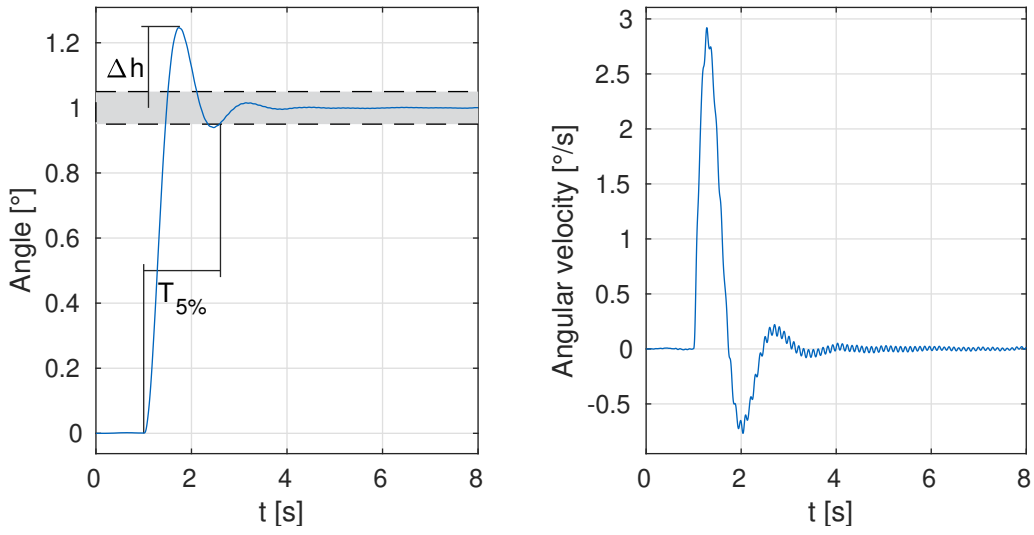

Figure 3.8: Step response of the system controlled with the PD+ controller

The two indicators visible in the step response are illustrated in fig. 3.8. The overshoot Δh specifies how far the output passes the desired value of 1° before settling to this value. The overshoot is often measured relative to the desired value and is given in percent. The settling time $T_{5\,\%}$ is reached when the output does not leave an error band of ±5 % anymore. For a perfect controller both indicators would converge to zero corresponding to perfect tracking behavior. For a system that is dominated by a pair of complex conjugated poles $p_{1/2}$ both measures can be easily calculated using eqs. (3.19) to (3.21) [21, p. 487-488]. Figure 3.9 shows the step response of the simulation together with this approximation as a second order system using the poles corresponding to the mechanical pendulum. The approximation is slightly shifted and does not incorporate the vibrations but does approximate the step response well overall. Thus, the system can be considered to be dominated by this pole pair which validates the approximation of the indicators based on the dominant pole pair for this specific controller.

$$p_{1/2} = -\delta_\mathrm{e} \pm j\omega_\mathrm{e} \tag{3.19}$$

$$\Delta h \approx \mathrm{e}^{-\frac{\delta_\mathrm{e}}{\omega_\mathrm{e}}\pi} \tag{3.20}$$

$$T_{5\,\%} \approx \frac{3}{\delta_\mathrm{e}} \tag{3.21}$$

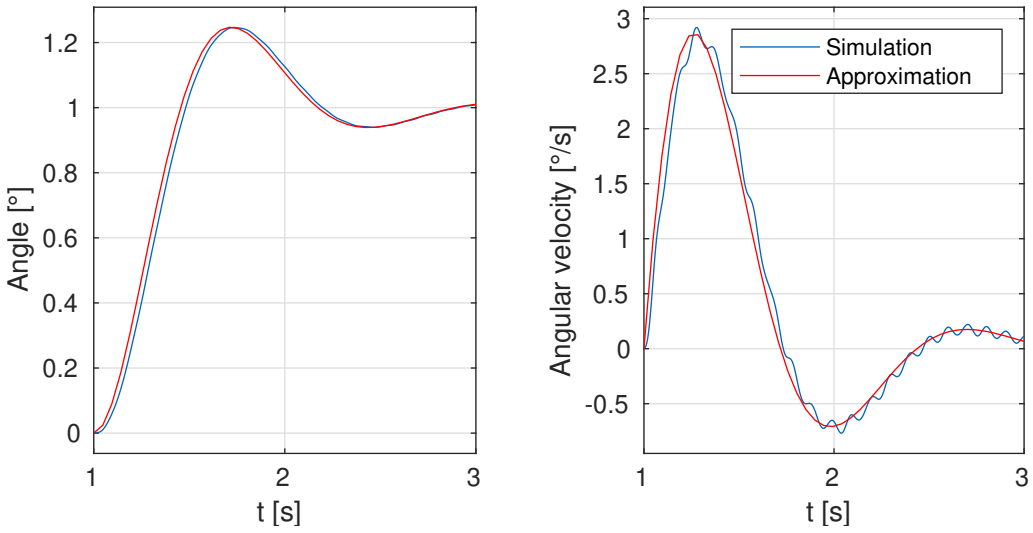

Figure 3.9: Comparison between the simulation output and the approximation with a second order system that only contains the dominant conjugated pole pair

Reference Transfer Function

The simulation model is nonlinear and prone to noise and thus does not have a perfect transfer function. For this application nonetheless the angles are typically low and thus, a linear approximation is reasonable. The identification of the transfer function can be done by using a sine sweep with logarithmic growth of the frequency as reference. This basically leads to a signal where all frequencies have approximately the same number of cycles and as a result small growth rates are necessary for the output to adjust to the input frequency [32]. Such growth rates lead to time consuming scenarios can be inapplicable in real-world application but are fine for a fast running simulation. Based on this input and corresponding output data the transfer function is approximated with the function TFESTIMATE of MATLAB which are based on [41]. The resulting reference transfer function can be seen in fig. 3.10. In this plot the bandwidth of the closed-loop system (see def. 3.1) is illustrated.

Definition 3.1 (Bandwidth)**.** The *bandwidth* of a Linear Time-Invariant (LTI) system is defined as the frequency interval $\omega = [0; \omega_c]$ where the energy of the output signal is more than half as high compared to the static case which results in the relation $|G(j\omega_c)|_{dB} \approx |G(0)|_{dB} - 3\,dB$ for the cutoff frequency ω_c [21, p. 299].

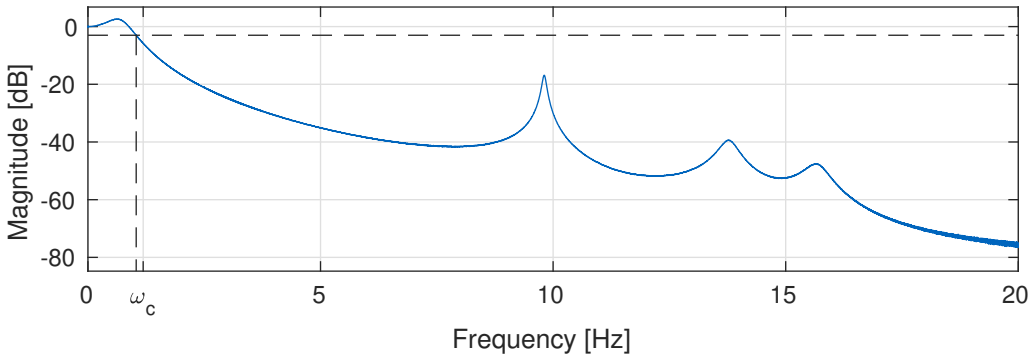

Figure 3.10: Identified reference transfer function $G_r(s)$ from desired angle $Y_{des,1}(s)$ to the resulting output angle $Y_1(s)$

Impulse Response

The impulse response is generated by applying the Dirac delta function as an input. In LOLA's application a possible disturbance would be an impact on the upper body due to a crash or a hit. This scenario is described with the parameters from table 3.3 and is an approximation of the ideal impulse. Figure 3.11 shows the response to this disturbance impulse which approximates the impulse response for the standard PD+ controlled system. The maximum and the minimum of the impulse response are used as a performance measure for disturbance rejection. In LOLA's application the reference trajectory is equal to zero most of the time and thus the disturbance rejection is of higher importance for the control design than the reference tracking.

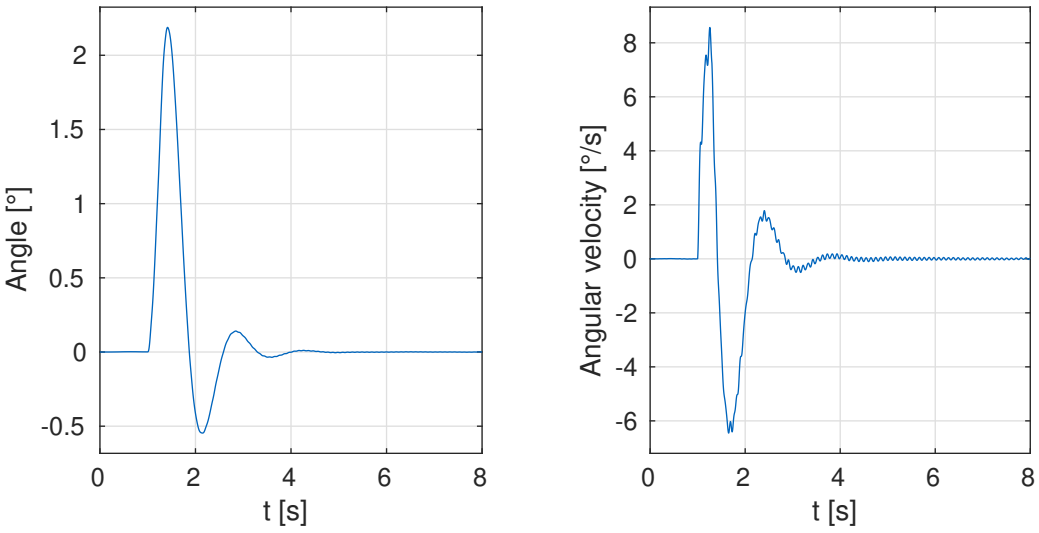

Figure 3.11: Response of the closed-loop system with a PD+ controller to a disturbance impulse

Disturbance transfer function

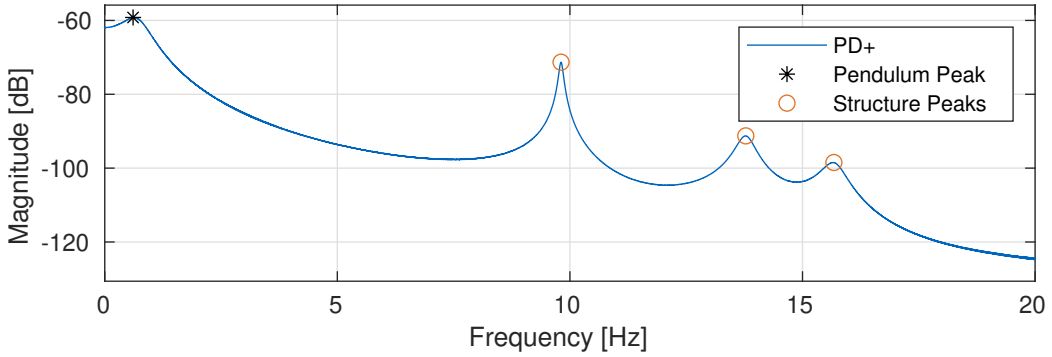

Figure 3.12: Identified disturbance transfer function $G_\mathrm{d}(s)$ from disturbance $D(s)$ to the resulting output angle $Y_1(s)$

The disturbance transfer function $G_\mathrm{d}(s)$ can be identified as described for the reference transfer function before by applying a sine sweep with adequate amplitude (see table 3.3) to the disturbance signal. The resulting transfer function can be seen in fig. 3.12. The figure contains one annotation with the resonance frequency due to the mechanics of the inverted pendulum which represents the disturbance rejection performance. Additionally the peaks resulting from the structural dynamics are highlighted. The magnitude of structural peak i is denoted as $|G_\mathrm{d}(j\omega_{\mathrm{r},i})|$. These peaks are the main measure for the resulting vibrations.

Robustness Analysis

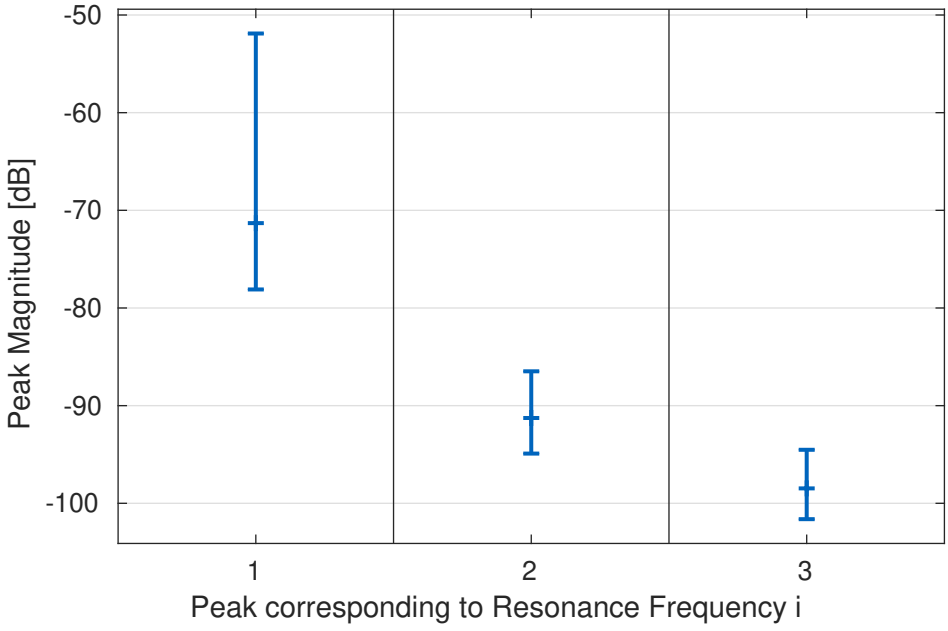

Figure 3.13: Variance of the structure peak magnitudes for varied parameters

As already mentioned the robustness is determined by varying some parameter of the LOLA model. As in LOLA's case the configuration does change during walking for example due to different arm positions the resonance frequencies will likely change. Additionally the arm position does alter the moment of inertia around the CoG. The configuration of the legs does affect the height of the CoG and thus, the length of the virtual pendulum can change. To evaluate the robustness of the system against these

changes the following simulation parameters are individually varied by ±20 %. All frequencies are shifted together as well as the first resonance anti-resonance pair. The damping factors are also all varied at once. Additionally the length of the pendulum l and the moment of inertia I_{CoG} are varied. To visualize the results the individual simulation outcomes have to be merged in one measure. This is done for the magnitudes of the peaks corresponding to the structural dynamics. Figure 3.13 illustrates the range of peak magnitudes for each structural resonance frequency. The bar covers the range between the maximal and the minimal peak magnitude over all parameter variations. The peak height for the nominal system is marked additionally. For example the peak of the first resonance frequency of the structure ranges from −78 dB to −52 dB while it is −71 dB for the nominal system. The maximal magnitude of the peak corresponding to resonance i with frequency $\omega_{\mathrm{r},i}$ is denoted by $|G_{\mathrm{d}}(j\omega_{\mathrm{r},i})|_{\max}$.

Table 3.3: Parameters for the simulation setting for approximating the step response and transfer functions

Parameter	Value
Impulse time	300 ms
Impulse amplitude	$0.5 \cdot T_{\max}$
Reference sine sweep amplitude	0.5°
Reference sine frequency range	[0.01 Hz; 30 Hz]
Reference sine target time	2000 s
Disturbance sine sweep amplitude	$0.1 \cdot T_{\max}$
Disturbance sine frequency range	[0.01 Hz; 30 Hz]
Disturbance sine target time	2000 s

Chapter 4

Controller Design

In this section control schemes for the previously introduced model are covered and designed. In the beginning of this chapter in section 4.1 the PD+ controller is evaluated on the system with structural dynamics which yields that the PD+ controller is not sufficient to control this kind of system and which stresses out the need for more sophisticated control schemes that are adapted to the structural dynamics. Thus, methods from the field of Active Vibration Damping are covered in section 4.2. Afterwards, model based control structures that evolve around state feedback with state estimation are introduced in section 4.3. In the end of the chapter in section 4.4 the concepts are compared with each other. The performance measures of all control schemes can be seen in table C.1 in appendix C

4.1 PD+ Controller

The goal of any control scheme is to achieve higher system dynamics compared the previously used controller which is the PD+ controller with the gains displayed in table 3.2. These gains were used on LOLA's balance controller in prior experiments. Using the PD+ controller one can realize increased performance by increasing the gains of the controller. For arbitrary, increased performance goals, for example $T_{5\,\%} < 1\,\mathrm{s}$ and $\Delta h < 20\,\%$, the gains $K_\mathrm{P} = 2200$ and $K_\mathrm{D} = 390$ are sufficient. Figure 4.1 contains the step response of the closed-loop with this more active PD+ controller. In this figure it is visible that whilst meeting the performance new requirements the system does vibrate significantly with lower damping and increased amplitude in comparison to the controller with the original gains.

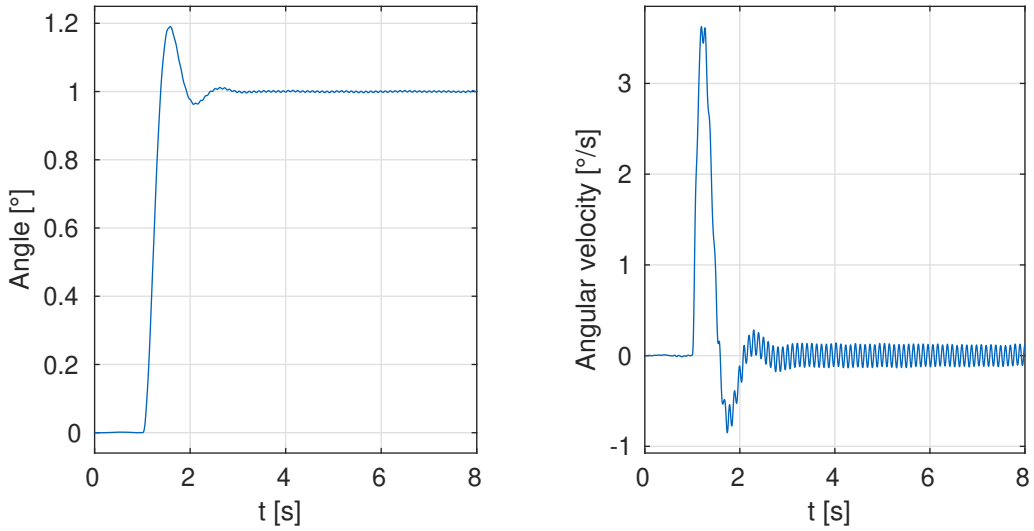

Figure 4.1: Step response for the PD+ controlled system with gains $P = 2200$ and $D = 380$

This effect can be illustrated well with a root locus plot. Figure 4.2 contains this root locus where the starting system without additional feedback is equal to the closed-loop with the original PD+ controller gains. The ratio of additional P and D gain is chosen such that the prior mentioned increased gains $P = 2200$ and $D = 390$ are lying on the trajectory. The plot does contain the poles of this more aggressively tuned system. It can be seen that the poles corresponding to the mechanical eigenfrequency of the pendulum are moved to the left and thus the performance in tracking and disturbance rejection is improved. But simultaneously the pole pairs corresponding to the first and second resonance frequencies of the structure are moved to the right of the complex plane and thus are less damped. For even higher gains the the poles would move into the right half of the complex plane and would destabilize the system. The PD+ controller is able to fulfill the new higher requirements but on cost of higher vibrations.

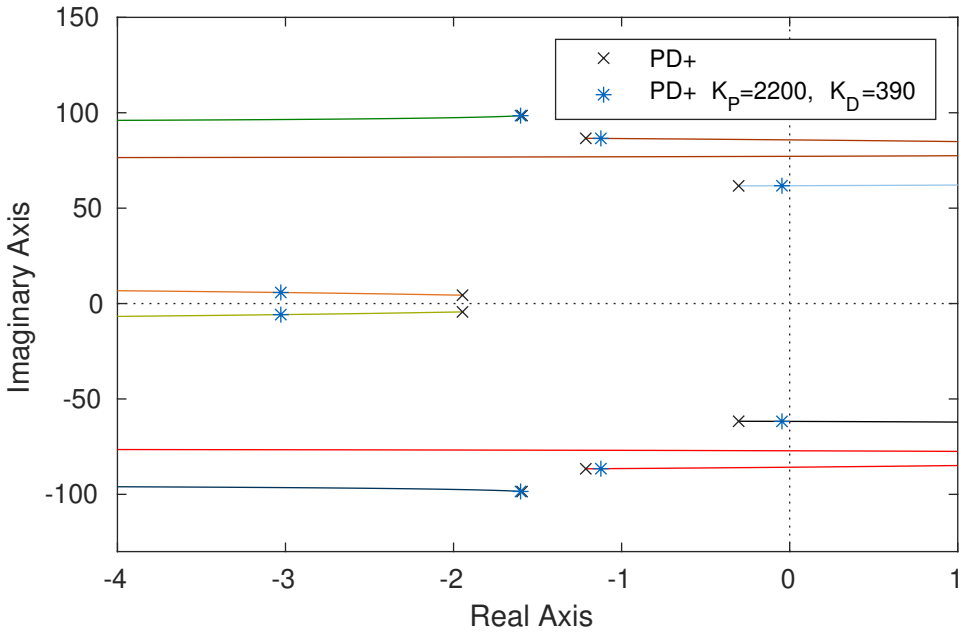

Figure 4.2: Root locus plot for increasing PD gains starting from the standard PD+ controlled closed-loop. Additionally the pole positions of one parameterization are highlighted.

Clearly the PD+ controller is not an adequate control approach for this system and increased performance requirements. Therefore, the following approaches will include strategies to tackle the vibrations directly. To be able to compare the control systems all are tuned to perform at least as well in tracking and disturbance rejection as the more aggressive PD+ controller. The vibration behavior and the robustness of these control systems are then compared to mark out the superior control scheme. The performance of the more aggressive PD+ controller with the gains $K_\mathrm{P} = 2200$ and $K_\mathrm{D} = 390$ are also the requirements for the following control systems on the step response

$$T_{5\,\%} \overset{!}{<} 1\,\mathrm{s}, \tag{4.1}$$

$$\Delta h \overset{!}{<} 20\,\% \tag{4.2}$$

and on the impulse response

$$\varphi_{\mathrm{i,min}} \overset{!}{>} -0.3^\circ, \tag{4.3}$$

$$\varphi_{\mathrm{i,max}} \overset{!}{<} 1.5^\circ \tag{4.4}$$

and on the bandwidth

$$\omega_\mathrm{c} \overset{!}{>} 1.34\,\mathrm{Hz}. \tag{4.5}$$

4.2 Active Vibration Damping

The PD+ controller alone does not suffice for the control of this lightly damped structure as the controller is solely based on the model of the rigid inverted pendulum. Therefore, different methods from the field of active vibration damping are introduced in sections 4.2.1 to 4.2.3 before being applied to LOLA's case in section 4.2.4. These methods generally do not need any model besides the location of the resonances and act only on these resonances [27, p. 11].

One key concept in active vibration damping is collocated control. One pair of sensor and actor is considered collocated if they are located at the same physical position [16, p. 115]. A more detailed definition can be found in [27, p. 26]. This property is crucial for control of flexible structures as many active damping approaches show guaranteed stability for this case if actor or sensor dynamics can be neglected [23, p. 213]. Namely those approaches are the resonant controller which is discussed in section 4.2.2 and the Positive Position Feedback (PPF) controller. PPF controllers can be applied for structures equipped with collocated strain actuators and sensors and thus, are not applicable for this thesis [27, p. 101].

4.2.1 Direct Acceleration Feedback

The PD+ controller only makes use of the measured angle φ_m and the measured angular velocity $\dot{\varphi}_\mathrm{m}$. Therefore, the idea of this concept is to improve the controller by adding acceleration feedback. The acceleration can be fed back directly with

$$u = -K_\mathrm{A} a_\mathrm{m}. \tag{4.6}$$

Neglecting the reference for simplicity, this feedback combined with the PD+ control law from eq. (2.4) can be interpreted as an output feedback controller of the gravity compensated system:

$$\begin{aligned} u &= -K_\mathrm{A} a_\mathrm{m} - K_\mathrm{D}\dot{\varphi}_\mathrm{m} - K_\mathrm{P}\varphi_\mathrm{m} - mgl\sin(\varphi_\mathrm{m}) \\ &= -\boldsymbol{k}_\mathrm{output}\cdot\boldsymbol{y} - mgl\sin(\varphi_\mathrm{m}). \end{aligned} \tag{4.7}$$

This direct acceleration can improve the damping of certain poles as can be seen in section 4.2.4 but also can destabilize the system for certain gains. For a similar setup in [44] even small gains of direct acceleration feedback did destabilize some of the structural resonances.

4.2.2 Resonant Controller

Another way to utilize the acceleration is by filtering the measured acceleration with a second order system with substantial damping [28]. This is also referred to as resonant controller [23]. The theory of this filter is based on a collocated single degree of freedom oscillator representing the structure:

$$\ddot{x} + 2D_\mathrm{n}\omega_\mathrm{n}\dot{x} + \omega_\mathrm{n}^2 x = u. \tag{4.8}$$

The corresponding filter and feedback law are derived as:

$$\ddot{v} + 2D_\mathrm{f}\omega_\mathrm{f}\dot{v} + \omega_\mathrm{f}^2 v = \ddot{x}, \tag{4.9}$$

$$u = -g\omega_\mathrm{f}^2 v. \tag{4.10}$$

It can be seen that the filter equation of the controller resonates at the resonance frequency ω_f which is why the concept is called resonance controller.

This control law stabilizes the system from eq. (4.8) for any $g > 0$ which is proven in [27, p. 97] and [34]. Additionally this compensator has a large roll-off at high frequencies which is positive as the risk of destabilizing high frequency modes may be reduced [27, p. 100]. These advantages do only hold for collocated systems with perfectly known dynamics and neglectable actor and sensor dynamics.

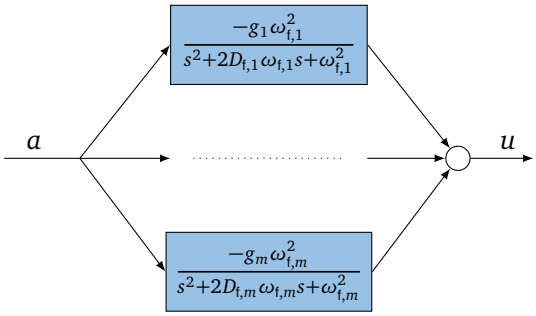

Figure 4.3: Acceleration feedback to damp m structural resonance frequencies with m independent second order compensators

To damp multiple nodes it is possible to add several compensators in parallel like illustrated in fig. 4.3 [27, p. 100]. Each filter is tuned to one resonance frequency of the structure and the damping values of the resonant controllers can be chosen independently as the action of the resonant filters are nearly uncoupled [26]. The transfer function of the resulting compensator derives to:

$$G(s) = \sum_{i=1}^{m} \frac{-g_i \omega_{\mathrm{f},i}^2}{s^2 + 2D_{\mathrm{f},i}\omega_{\mathrm{f},i}s + \omega_{\mathrm{f},i}^2} \tag{4.11}$$

This feedback consisting of possibly multiple resonant controllers can be combined with other control methods in a cascaded manner. For example the resonant controllers can form a inner control loop with an outer loop consisting of a Proportional-Integral (PI) controller [1].

4.2.3 Notch Filter

One approach in non-collocated control is to supplement the controller with a notch filter that has two zeros located near the flexible poles of the system [27, p. 80]. The transfer function of this filter can be formulated as

$$G_{\mathrm{Notch}}(s) = \frac{s^2 + 2g_{\mathrm{min}}D_{\mathrm{Notch}}\omega_{\mathrm{Notch}}s + \omega_{\mathrm{Notch}}^2}{s^2 + 2D_{\mathrm{Notch}}\omega_{\mathrm{Notch}}s + \omega_{\mathrm{Notch}}^2}. \tag{4.12}$$

The general idea is to use the zeros or numerator roots to cancel the resonant poles of the structure while introducing new poles with a larger negative real part [33].

The tuning parameters of this transfer function can be illustrated well in the bode plot in fig. 4.4. The frequency ω_{Notch} is called notch frequency and determines the natural frequency of the zeros and poles of the filter. The parameter g_{min} determines the depth of the transfer function at the notch frequency and is often set to zero. The damping ratio D_{Notch} determines the damping of the filter poles which changes the width of the notch in the bode plot. High damping values correspond to a wider notch while low damping values lead to a sharp notch. In the figure the transfer functions for different damping values are included to illustrate this relation.

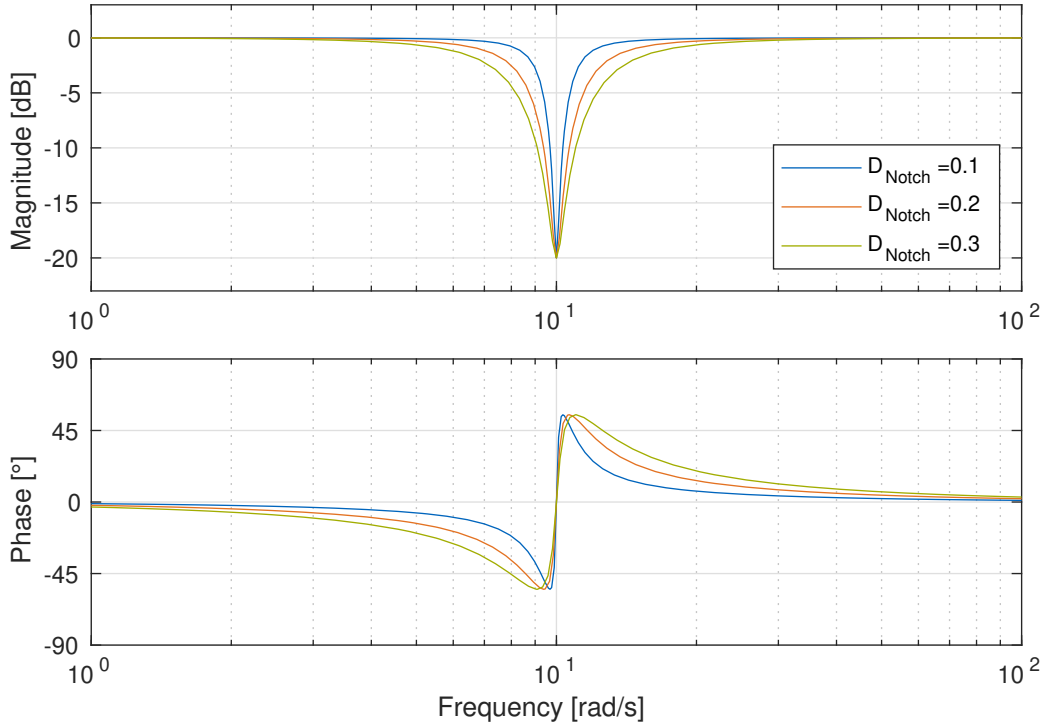

Figure 4.4: Bode plot of notch filters with $g_{\text{min}} = 0.1$ and $\omega_{\text{Notch}} = 10\,\text{rad}\,\text{s}^{-1}$ and varying damping values D_{Notch}

This filter has to be tuned closely to match the frequency of the resonance that shall be attenuated. If tuned correctly the filter damps the targeted flexible mode and allows an increased bandwidth of the system. However, the notch filter lacks robustness to parameter changes and thus, has to be applied with care if the uncertainty of the system model is great [27, p. 81]. In [27] an example is used to demonstrate this sensitivity to parameter changes. In this example a variation of the flexible mode frequency by 20 % leads to a zero-pole flipping where the previously stable branches of the root locus plot become unstable.

4.2.4 Active Vibration Control of the Flexible Inverted Pendulum

In this thesis different approaches from the field of active vibration damping are tested. All of those approaches base on the PD+ controller and extend this rather simple controller to increase its capability to reject the vibrations caused by the spine of LOLA. Namely those approaches are:

1. PD+ with direct acceleration feedback
2. PD+ with notch filters
3. PD+ with notch filters and direct acceleration feedback
4. PD+ with resonant controllers

All control schemes are tuned to perform as well as the standalone PD+ controller from section 4.1 to obtain a standardized point to compare the vibration behavior of the closed-loop systems. As mentioned before the concepts of active vibration damping base on a good knowledge of the resonance frequencies and thus, the robustness of these concepts against frequency change will be looked at with special care.

Direct Acceleration Feedback

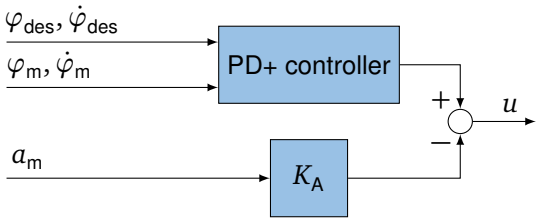

Figure 4.5: Balance Controller using the PD+ controller with additional direct acceleration feedback

Figure 4.5 displays the balance controller consisting of a PD+ controller with additional direct acceleration feedback. The effect of this acceleration feedback can be illustrated with a root locus plot that displays the trajectories of the poles when increasing the acceleration feedback gain K_A. This plot is displayed in fig. 4.6. It can be seen that by feeding back the acceleration the poles corresponding to the first resonance frequency of the structure are moved to the left for increasing acceleration gains and thus, additional damping can be introduced for the first resonance. This is achieved at the cost of potentially reducing the damping of the higher frequencies and the mechanical poles of the inverted pendulum. The system can even be destabilized for certain acceleration feedback gains, as the poles corresponding to the third and highest structural resonance can enter the right half plane.

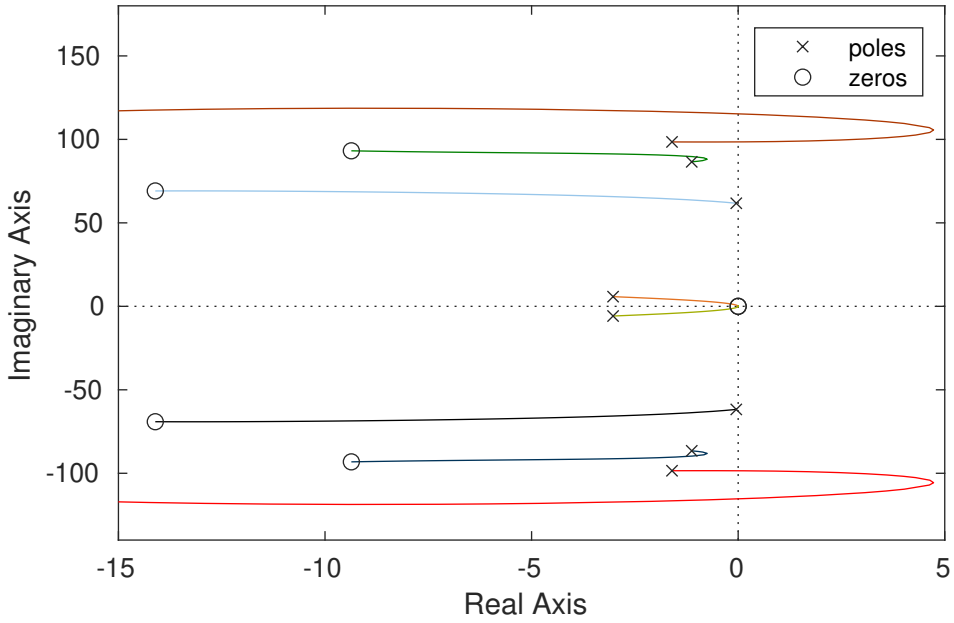

Figure 4.6: Root locus plot of a PD+ controlled system for additional direct acceleration feedback

As the acceleration feedback moves the poles of the inverted pendulum to the right in the complex plain the gains of the PD+ controller have to be increased to maintain the performance requirements. The gains displayed on the left of table 4.1 are used for the controller.

Table 4.1: Parameters of the PD+ controller with additional direct acceleration feedback

Parameter	Value
K_P	2400
K_D	400
K_A	5

Figure 4.7 shows the variance of the vibration peak magnitudes for varying system dynamics compared between the PD+ controlled system and the system with additional direct acceleration feedback. It can be seen that for the nominal system the acceleration feedback improves the peak magnitude of the first resonance significantly while increasing the peaks corresponding to the second and third resonance. Problematic is that the robustness is not improved by adding direct acceleration feedback. Looking at all varied system dynamics one can see that the acceleration feedback improves the maximal peak magnitude of the first resonance marginally and has increased maximal peak magnitudes for the higher resonances. Therefore, direct acceleration feedback with PD+ control is considered insufficient as a control approach for this application and not treated in the following.

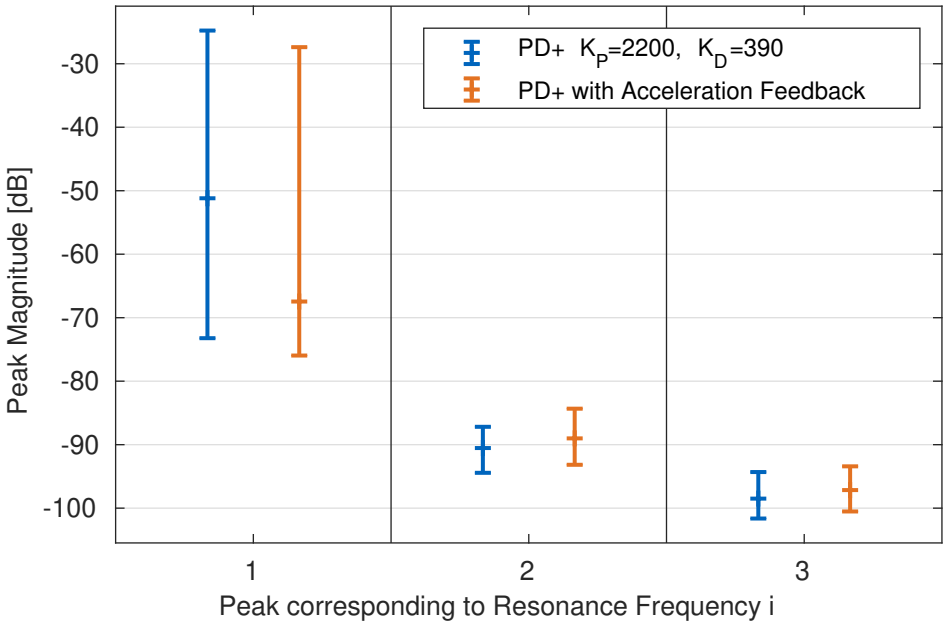

Figure 4.7: Variance of the peak magnitudes from the structural resonances over system dynamics variations compared between the PD+ controlled system and the system with additional acceleration feedback

Resonant Controller

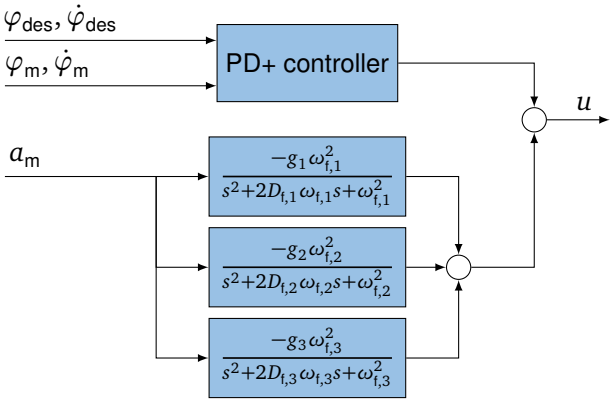

Figure 4.8: Balance Controller using the PD+ controller with additional second order filtered acceleration feedback

The feedback using second order filters is realized with the control setup displayed in fig. 4.8. The resonant controller can be seen as an inner loop with an outer loop consisting of the PD+ controller. One resonant filter is tuned to each resonance frequency. The output of these filters forms the control

input u together with the output of the PD+ controller. One advantage of this approach is that the gains of the PD+ controller do not have to be changed as the additional feedback does not effect the poles corresponding to the inverted pendulum significantly. Thus, the tuning of the PD+ controller and the filtered acceleration feedback can be done almost independently. The parameterization used in this thesis can be seen in table 4.2.

Table 4.2: Parameters of the resonant controllers and the corresponding PD+ controller

Parameter	Resonant Filter 1	Resonant Filter 2	Resonant Filter 3
g_i	1	1	1
$\omega_{\mathrm{f},i}$	$61.58\,\mathrm{rad\,s^{-1}}$	$86.71\,\mathrm{rad\,s^{-1}}$	$98.65\,\mathrm{rad\,s^{-1}}$
$D_{\mathrm{f},i}$	0.1	0.2	0.8
K_{P}		2200	
K_{D}		390	

The effect of this acceleration feedback is illustrated with a root locus plot in fig. 4.9. This plot illustrates the influence of the three resonant controllers by displaying the trajectory of the closed-loop poles when increasing the gains g_i collectively from 0 to 1. It can be seen that primarily the poles corresponding to the first and second resonance frequency of the structure are moved to the left and thus, have increased damping. The poles corresponding to the third resonance frequency are slightly moved to the right and the mechanical poles of the pendulum are moved to the left. It can be said that by adding this kind of acceleration feedback the first and most critical resonance frequency can be damped significantly for the nominal system dynamics. It should be mentioned that the filters introduce poles and zeros that are faster than the range if fig. 4.9 and are not displayed for better clarity.

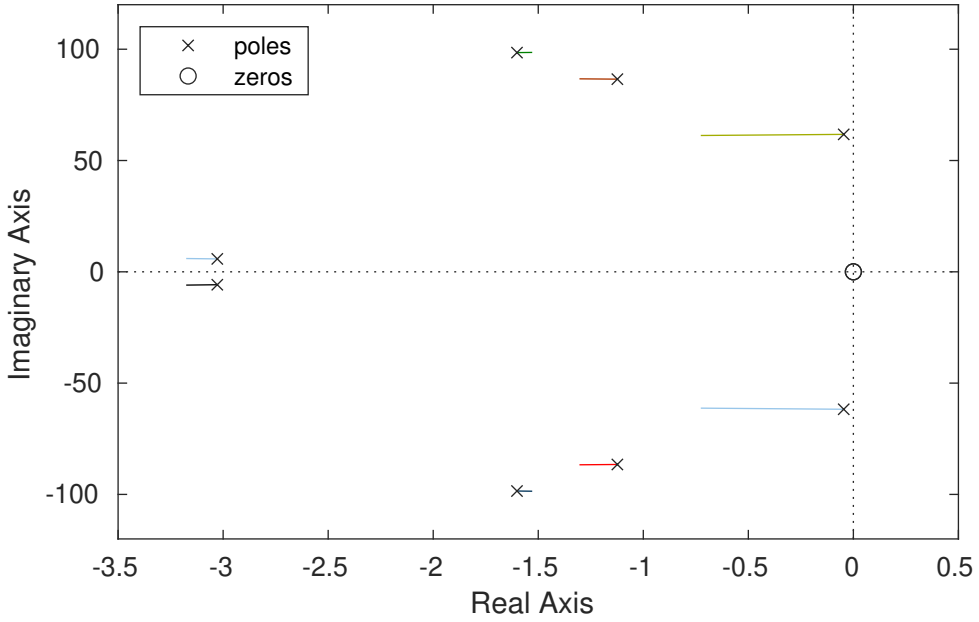

Figure 4.9: Root locus plot for the PD+ controlled system and additional second order filtered acceleration feedback with gains in the range [0;1]

In fig. 4.10 the disturbance transfer function is displayed for the system controlled with PD+ control and the system with additional resonance controllers. It can be seen that the transfer functions are nearly the same but for frequencies close to the resonances. As already mentioned this effect allows to tune the PD+ controller and the resonant controller independently which simplifies the tuning process.

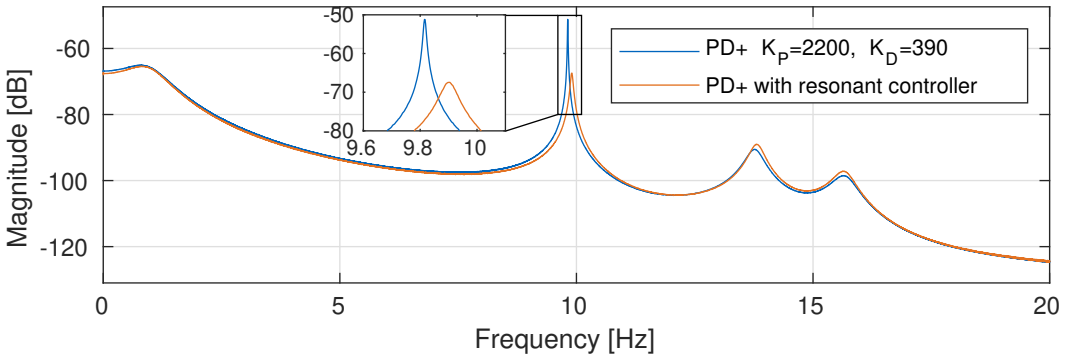

Figure 4.10: Disturbance transfer function compared between the PD+ controller and the PD+ controller with additional second order filtered acceleration feedback

The peaks in the disturbance transfer function under system variation are displayed in fig. 4.11. It can be seen that for the first structural resonance the peak is significantly reduced for the nominal system by adding the resonant controller. But under perturbation of the system dynamics the maximal peak of the first resonance for the system with additional resonant controller is higher than without the resonant controller. The peaks of the second and third resonance and barely effected by the resonant controller. Overall the resonant controllers are not robust against parameter changes and can behave even worse than the PD+ controller system for varied system dynamics. Therefore, the resonant controller are considered incapable of improving the vibration rejection of the PD+ controller for perturbed system dynamics and are not considered in the following of this thesis.

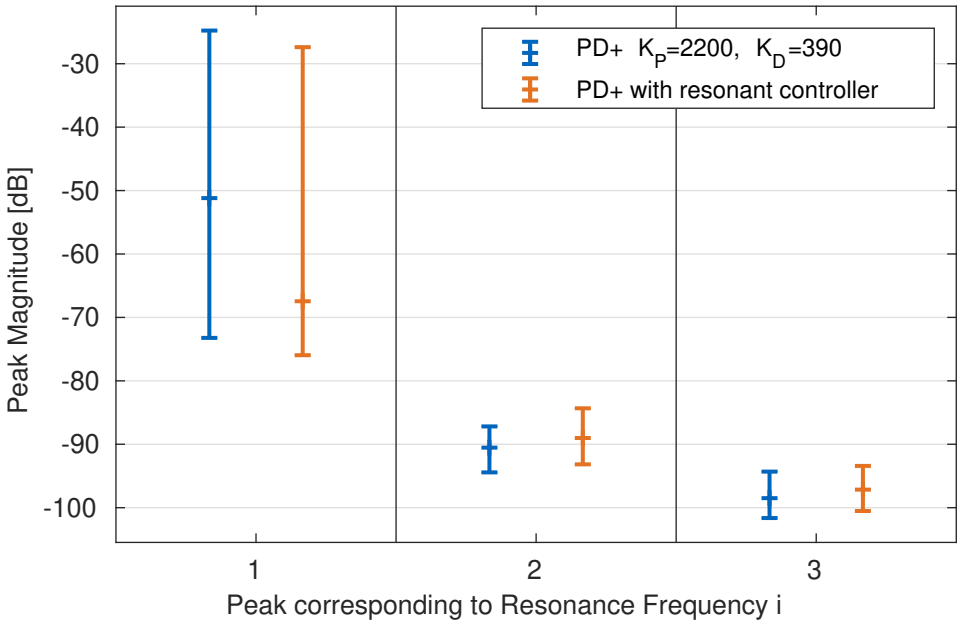

Figure 4.11: Variance of the magnitude of the peaks corresponding to the structural resonances compared between the PD+ controller and the PD+ controller with additional second order filtered acceleration feedback

Notch Filters

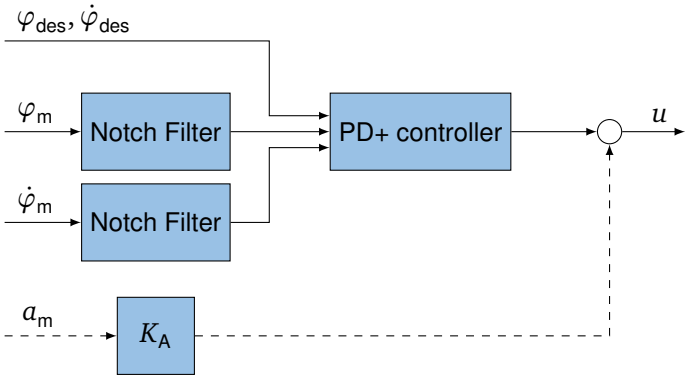

Figure 4.12: Balance Controller using a combination of notch filters and PD+ controller and acceleration feedback

The control setup using notch filters and the PD+ controller is displayed in fig. 4.12. Additional direct acceleration feedback is optional and thus, illustrated with dotted lines. In this setup the notch filters are used to filter the vibrations from the input of the PD+ controller. The acceleration feedback is unfiltered such that the poles can be influenced as in section 4.2.1.

The notch filters are tuned on the resonance frequencies. The width of the notch filter requires a compromise. A notch filter with small width filters the signal parts in resonance frequency and has a low effect on the other parts of the signal but is sensitive to varying resonance frequencies. In contrast, a notch filter with a larger width filters the signal parts in resonance frequencies even for varied resonance frequencies but is also effecting a larger frequency range of the signal and thus, signal intensity and information is getting lost. Subsequently, the notch has to be wide enough to tolerate variations of the resonance frequency while still being small enough to keep as much of the unfiltered signal as possible.

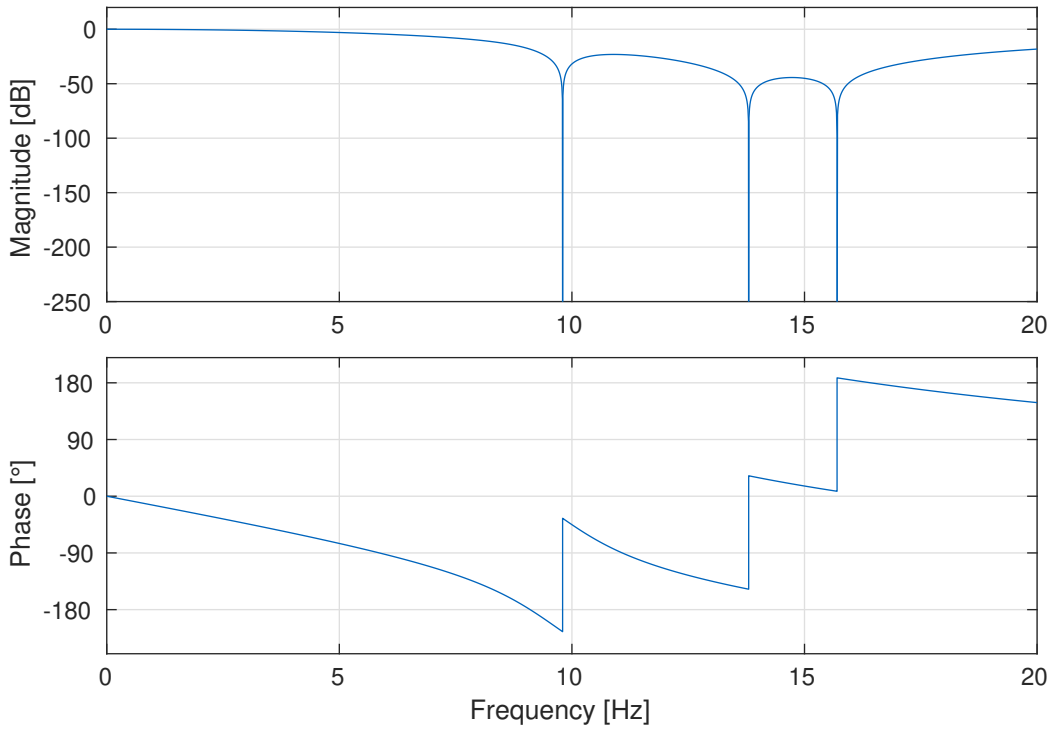

Figure 4.13: Bode diagram of the filter consisting of 3 notch filters tuned on the 3 resonance frequencies with infinite depth as $g_{min} = 0$

Table 4.3: Parameters of the notch filters and the corresponding PD+ controller or PD+ controller with direct acceleration feedback

Parameter	Notch 1	Notch 2	Notch 3
g_{min}	0	0	0
ω_{Notch}	$61.58\,\text{rad}\,\text{s}^{-1}$	$86.71\,\text{rad}\,\text{s}^{-1}$	$98.65\,\text{rad}\,\text{s}^{-1}$
D_{Notch}	0.15	0.8	0.8
K_{P}	2500	2800	
K_{D}	550	600	
K_{A}	0	20	

The parameters used for this thesis can be seen in table 4.3 and the transfer function of the corresponding notch filter is displayed in fig. 4.13. It can be seen that higher PD+ gains are necessary to fulfill the performance requirements of the closed-loop system compared to the PD+ controller without notch filters. This is a result of the loss of signal intensity due to the filtering. The table does additionally contain a parameterization of the PD+ controller with notch filters and acceleration feedback.

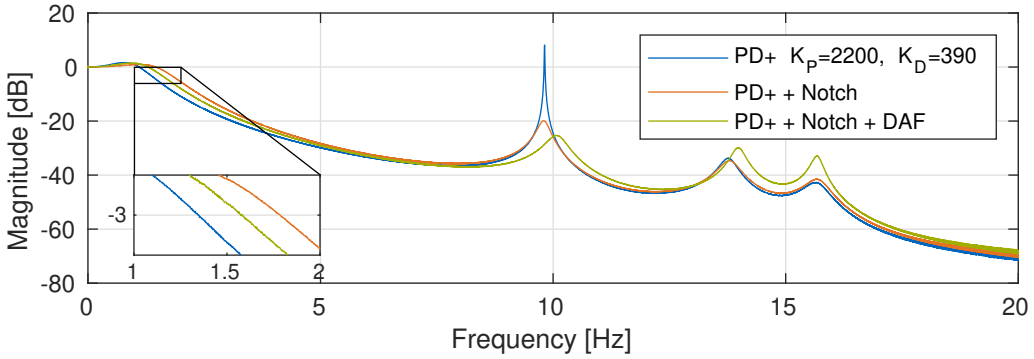

Figure 4.14: Reference transfer function compared between the standalone PD+ controller and the PD+ controller with notch filters and additional acceleration feedback

Figure 4.14 displays the reference transfer function for both notch filter setups and the standalone PD+ controller. In the enlarged area of the plot it can be seen that both setups with the notch filter achieve an improved closed-loop bandwidth.

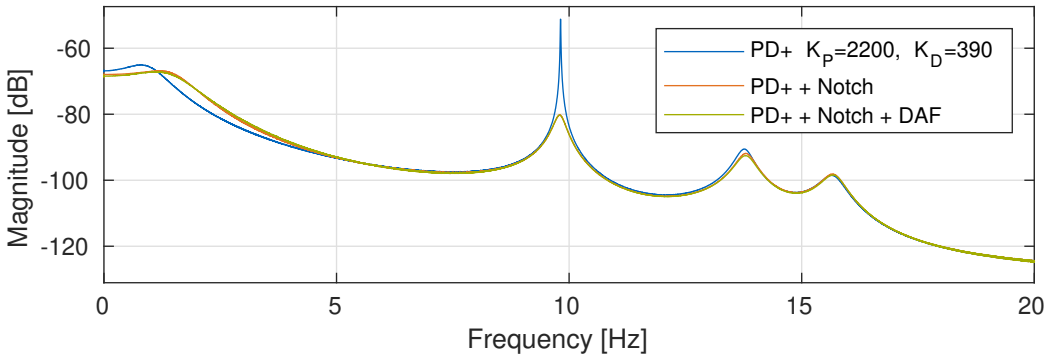

Figure 4.15: Disturbance transfer function compared between the standalone PD+ controller and the PD+ controller with notch filters and additional acceleration feedback

The disturbance transfer function can be seen in fig. 4.15. The addition of notch filters improves the peak corresponding to the first structural resonance significantly compared to the standalone PD+ controller. The peak of the second resonance is decreased while the peak corresponding to the third resonance in

not significantly changed. By adding additional acceleration feedback the first peak can be decreased further at the cost of increasing the peaks corresponding to the higher resonances.

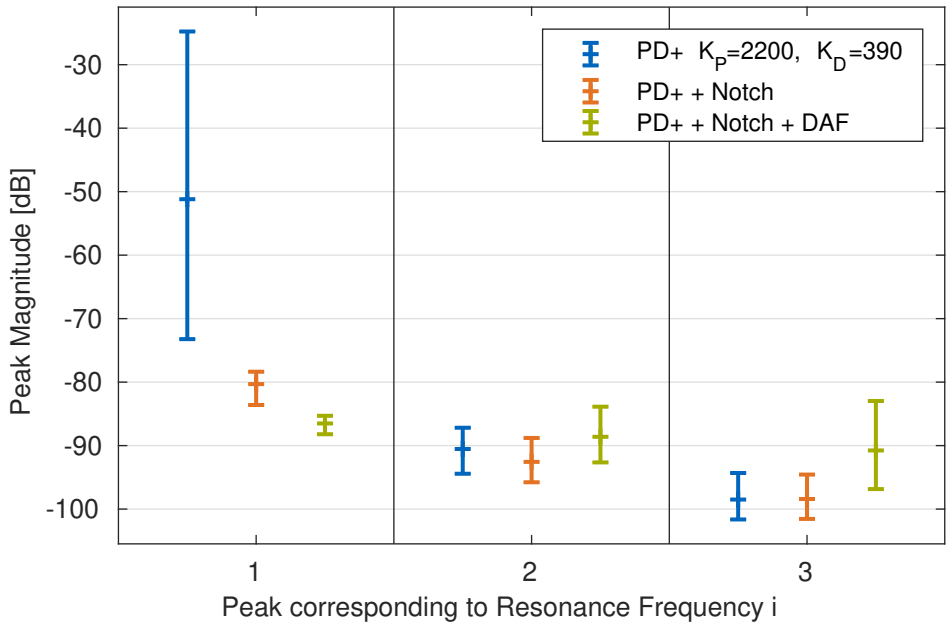

Figure 4.16: Peak magnitudes of the structural resonances in the disturbance transfer function under system perturbations compared between the standalone PD+ controller and the PD+ controller with notch filters and additional direct acceleration feedback (DAF)

The robustness of the control schemes with notch filters can be evaluated based on fig. 4.16. It can be seen that the notch filter without acceleration feedback has improved robustness in the first peak and similar robustness for the higher resonances compared to the PD+ controller. The addition of acceleration feedback improves the robustness and magnitude of the peak corresponding to the first resonance. This is achieved at the cost of increased magnitude and worsened robustness in the second and third peak. As the maximal peak magnitude with acceleration feedback is still lower than the highest peak magnitude of the controller without acceleration feedback the addition of direct acceleration feedback is considered superior.

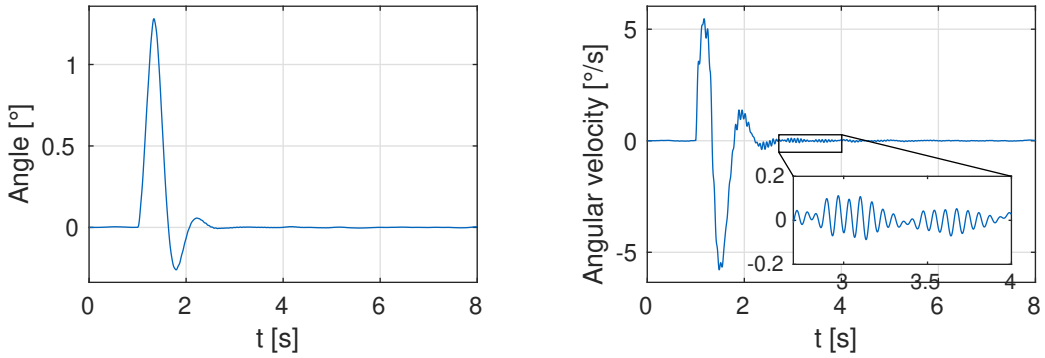

Figure 4.17: Impulse response of the closed-loop system controlled by PD+ controller with notch filters and additional acceleration feedback

The magnitudes of the peaks of the resonances are closer together for the controller with notch filters and acceleration feedback. This can be seen in the vibrations caused by an disturbance impulse in fig. 4.17. The vibration in the enlarged area is not dominated by the first resonance but a superposition of all resonance frequencies.

4.3 Model Based Control Approaches

One problem of the PD+ controller is that the vibration-prone signals are directly fed back, possibly leading to an excitation in resonance frequency. Therefore, one approach to improve the behavior of the closed-loop is to reconstruct the complete state of the system and subsequently feed back the internal states that are not subjected to vibration. This can be done using modern methods of control theory which expand past basic transfer function and work with state-space models. The general form of Single-Input-Multiple-Output (SIMO) system can be seen in eqs. (4.13) and (4.14). For such a system complete state feedback can be used to set the desired dynamics of the closed-loop system which is discussed in section 4.3.1. As the state is not measurable in many cases the state has to be reconstructed from the measurements which will be treated in section 4.3.2. At the end of this chapter in section 4.3.3 these principles will be applied to LOLA.

$$\dot{\boldsymbol{x}} = \boldsymbol{A}\boldsymbol{x} + \boldsymbol{b}u \tag{4.13}$$

$$\boldsymbol{y} = \boldsymbol{C}\boldsymbol{x} + \boldsymbol{d}u \tag{4.14}$$

4.3.1 State Feedback Controller

For state feedback the control law from eq. (4.15) is applied. The complete state vector is fed back with individual gains g_i:

$$u = -\boldsymbol{g} \cdot \boldsymbol{x}. \tag{4.15}$$

The closed-loop dynamics neglecting the reference trajectory derives to:

$$\dot{\boldsymbol{x}} = \boldsymbol{A}\boldsymbol{x} - \boldsymbol{b}\boldsymbol{g}\boldsymbol{x} = (\boldsymbol{A} - \boldsymbol{b}\boldsymbol{g})\,\boldsymbol{x}. \tag{4.16}$$

If the system is controllable (def. 4.1) the poles of the dynamics of this closed-loop system can be set arbitrarily [27, p. 145].

Definition 4.1 (Controllability)**.** A system is referred to as *completely controllable* if the state of the system $\boldsymbol{x}$ can be transferred from any initial state $\boldsymbol{x}_0$ to any final state $\boldsymbol{x}_f$ in finite time t_e [22, p. 64].

The controllability of a system can be proven using the Hautus Lemma which says that the system with dynamics matrix $\boldsymbol{A}$ and input matrix $\boldsymbol{b}$ is completely controllable if the relation

$$\operatorname{rank}\left(\begin{bmatrix}\lambda_i \boldsymbol{I} - \boldsymbol{A} & \boldsymbol{b}\end{bmatrix}\right) = n \tag{4.17}$$

holds for every eigenvalue λ_i of $\boldsymbol{A}$ with $i = 1, 2, ..., n$ [22, p. 81]. In comparison to the Kalman criterion (using the rank of the controllability matrix [22, p. 66]) the Hautus Lemma has the advantage that the rank of a smaller system has to be computed at the cost of the eigenvalue determination. Therefore, the Hautus Lemma is used in this thesis.

Having defined a state feedback controller the reference tracking behavior has to be set. Often it is desired to have perfect steady state control accuracy which can be formulated with the following condition:

$$\dot{\boldsymbol{x}} = \boldsymbol{A}\boldsymbol{x}_{\text{ss}} + \boldsymbol{b}u_{\text{ss}} \stackrel{!}{=} \boldsymbol{0}, \tag{4.18}$$

$$\boldsymbol{y}_{\text{ss}} = \boldsymbol{C}\boldsymbol{x}_{\text{ss}} + \boldsymbol{d}u_{\text{ss}} \stackrel{!}{=} \boldsymbol{y}_{\text{des,ss}}. \tag{4.19}$$

These conditions can be reformulated in matrix notation:

$$\begin{bmatrix}\boldsymbol{A} & \boldsymbol{b} \\ \boldsymbol{C} & \boldsymbol{d}\end{bmatrix}\begin{bmatrix}\boldsymbol{x}_{\text{ss}} \\ u_{\text{ss}}\end{bmatrix} = \begin{bmatrix}\boldsymbol{0} \\ \boldsymbol{I}\end{bmatrix}\boldsymbol{y}_{\text{des,ss}}. \tag{4.20}$$

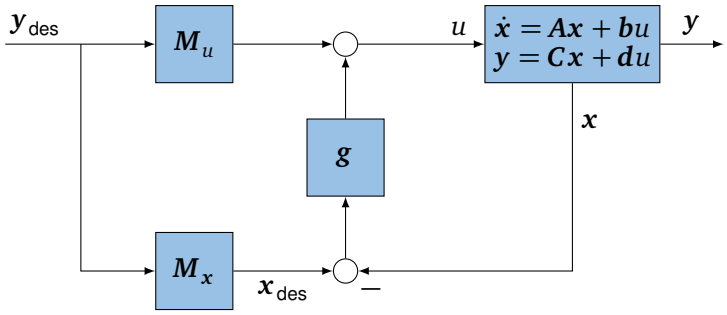

Figure 4.18: Control scheme with state feedback and feedforward control

The structure of the feedforward control combined with the state feedback controller can be seen in fig. 4.18. In steady state the desired state vector $\boldsymbol{x}_{\text{des}}$ calculated by the feedforward control has to be equal to the steady state vector $\boldsymbol{x}_{\text{ss}}$ and thus, the control input u_{ss} is calculated from the desired output $\boldsymbol{y}_{\text{des,ss}}$ by the prefilter. The resulting relation can be found to be:

$$\begin{bmatrix} \boldsymbol{x}_{\text{ss}} \\ u_{\text{ss}} \end{bmatrix} = \begin{bmatrix} \boldsymbol{M}_x \\ \boldsymbol{M}_u \end{bmatrix} \boldsymbol{y}_{\text{des,ss}}. \tag{4.21}$$

This equation can be combined with eq. (4.20) to form the system:

$$\begin{bmatrix} \boldsymbol{A} & \boldsymbol{b} \\ \boldsymbol{C} & \boldsymbol{d} \end{bmatrix} \begin{bmatrix} \boldsymbol{M}_x \\ \boldsymbol{M}_u \end{bmatrix} \boldsymbol{y}_{\text{des,ss}} = \begin{bmatrix} \boldsymbol{0} \\ \boldsymbol{I} \end{bmatrix} \boldsymbol{y}_{\text{des,ss}}. \tag{4.22}$$

This equation system has to be solved in order to obtain the feedforward control matrices $\boldsymbol{M}_u$ and $\boldsymbol{M}_x$. For this thesis the MATLAB function MLDIVIDE is used to solve this system.

Pole Placement

One way to choose the feedback gain $\boldsymbol{g}$ is to specify desired poles $s_1, ..., s_n$ for the resulting closed-loop dynamics. This is generally referred to as pole placement. One matches the characteristic equation with the desired pole positions by setting the gain $\boldsymbol{g}$. Different approaches tackle this matching but for this thesis the MATLAB implementation is used which is based on an algorithm introduced in [18]. This algorithm obtains a solution where the sensitivity of the position of the poles to perturbations in the system dynamics and gain matrix is minimized.

$$\det[s\boldsymbol{I} - (\boldsymbol{A} - \boldsymbol{g}\,\boldsymbol{b})] \stackrel{!}{=} (s - s_1)\ldots(s - s_n) = 0 \tag{4.23}$$

One disadvantage of this method is that one has to determine the desired positions of the poles. Poles with small negative real parts are referred to as slow and cause slow closed-loop dynamics. Poles with large negative real parts or fast poles lead to fast dynamics but also to high values of the control input. The desired poles are often found using a trial and error approach.

Linear Quadratic Regulator

Another way to determine the linear state feedback gain $\boldsymbol{g}$ is to choose the controller in a way that the quadratic cost functional

$$J = \int_0^\infty \left(\boldsymbol{x}^T \boldsymbol{Q} \boldsymbol{x} + \boldsymbol{u}^T \boldsymbol{R} \boldsymbol{u}\right) \mathrm{d}t \tag{4.24}$$

is minimized. The resulting controller is called Linear Quadratic Regulator (LQR). The weight matrix $\boldsymbol{Q}$ manages the contribution from the state vector $\boldsymbol{x}$ to the cost functions. As some states may be irrelevant to the cost function the matrix $\boldsymbol{Q}$ has to be positive semi-definite. The control input is scaled with

the matrix $\boldsymbol{R}$ and as every control input shall contribute to the cost function the matrix has to be strictly positive definite.

The solution can be found by using eq. (4.25) where $\boldsymbol{P}$ is a solution of the Algebraic Ricatti Equation (ARE) from eq. (4.26).

$$\boldsymbol{g} = \boldsymbol{R}^{-1}\boldsymbol{B}^T\boldsymbol{P} \tag{4.25}$$

The ARE equation is generally solvable if the system is controllable [27, p. 195].

$$\boldsymbol{P}\boldsymbol{A} + \boldsymbol{A}^T\boldsymbol{P} + \boldsymbol{Q} - \boldsymbol{P}\boldsymbol{B}\boldsymbol{R}^{-1}\boldsymbol{B}^T\boldsymbol{P} = 0 \tag{4.26}$$

In contrast to pole placement this regulator design does not require desired pole positions. Instead one has to find the weight matrices $\boldsymbol{Q}$ and $\boldsymbol{R}$ which can be more intuitive.

4.3.2 State Estimation

State feedback alone is often not realizable as not all states can be measured or it would be too costly to do so. Therefore, the state has to be estimated based on the available measurements. One way to realize this estimation is the use of a Luenberger observer. The idea is to simulate the model of the process and correcting the simulated model based on the difference between modeled output and actual measurement. Another popular state estimator is the Kalman Filter which bases on a statistical model that is objected to noise. Both concepts are discussed in the following sections before applying them to the LOLA model.

Luenberger Observer

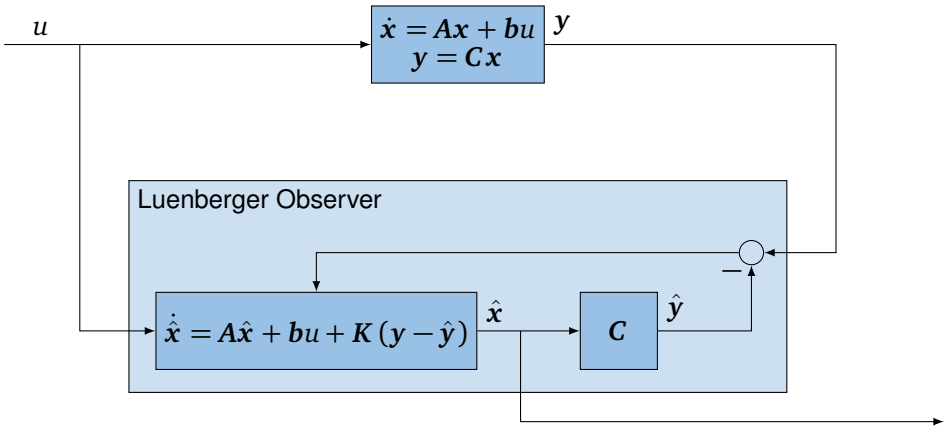

Figure 4.19: Structure of a Luenberger Observer

The foundation of the Luenberger observer is a linear time-invariant model of the observer process which is usually written as:

$$\dot{\boldsymbol{x}} = \boldsymbol{A}\boldsymbol{x} + \boldsymbol{b}u, \tag{4.27}$$

$$\boldsymbol{y} = \boldsymbol{C}\boldsymbol{x} + \boldsymbol{d}u. \tag{4.28}$$

Using this model the observer makes a prediction of the current state based on a previously estimated or initial state vector. To achieve a decaying error in the prediction of the state vector, the output of the

model is compared to the measurement and fed back into the observer with gain $\boldsymbol{K}$. This procedure is illustrated in fig. 4.19. The resulting observer can be characterized with the equation

$$\dot{\hat{\boldsymbol{x}}} = \boldsymbol{A}\hat{\boldsymbol{x}} + \boldsymbol{B}u + \boldsymbol{K}\left(\boldsymbol{y} - \boldsymbol{C}\hat{\boldsymbol{x}}\right). \tag{4.29}$$

Equation (4.30) defines the dynamics of the estimation error e which can be obtained by subtracting the dynamics of the observer from the dynamics of the model:

$$\dot{\boldsymbol{e}} = \dot{\boldsymbol{x}} - \dot{\hat{\boldsymbol{x}}} = (\boldsymbol{A} - \boldsymbol{K}\boldsymbol{C})\boldsymbol{e}. \tag{4.30}$$

It can be seen that the error dynamics are governed by the eigenvalues of the matrix $(\boldsymbol{A} - \boldsymbol{K}\boldsymbol{C})$. As the eigenvalues of a matrix are equal to the eigenvalues of the transposed matrix the matrix can be transposed which yields:

$$(\boldsymbol{A} - \boldsymbol{K}\boldsymbol{C})^T = \boldsymbol{A}^T + \boldsymbol{C}^T\boldsymbol{K}^T. \tag{4.31}$$

It can be seen that the observer design is equivalent to state regulator design of the dual system

$$\dot{\boldsymbol{x}}_\mathrm{T} = \boldsymbol{A}^T\boldsymbol{x}_\mathrm{T} + \boldsymbol{C}^T\boldsymbol{u}_\mathrm{T} \tag{4.32}$$

with the control law

$$\boldsymbol{u}_\mathrm{T} = -\boldsymbol{K}^T\boldsymbol{x}_\mathrm{T}. \tag{4.33}$$

If the dual system is controllable the pole placement algorithm can be used to place the observer poles. The dual system is completely controllable if the observer model is completely observable (def. 4.2) and thus, the observer poles can be places arbitrarily if the system is completely observable.

Definition 4.2 (Observability)**.** A system is called *completely observable* if the initial state $\boldsymbol{x}_0$ can be reconstructed from known input and output signals over a finite time interval [22, p. 92].

Analog to the controllability the observability can also be proven using the Hautus Lemma. It says that the system with dynamics matrix $\boldsymbol{A}$ and output matrix $\boldsymbol{C}$ is completely observable if

$$\operatorname{rank}\left(\begin{bmatrix}\lambda_i\boldsymbol{I} - \boldsymbol{A}\\ \boldsymbol{C}\end{bmatrix}\right) = n \tag{4.34}$$

holds for every eigenvalue λ_i of $\boldsymbol{A}$ with $i = 1, 2, ..., n$ [22, p. 101].

When combining this Luenberger observer with the state feedback one can derive the differential equation containing the state dynamics and the estimation error dynamics:

$$\begin{pmatrix}\dot{\boldsymbol{x}}(t)\\ \dot{\boldsymbol{e}}(t)\end{pmatrix} = \begin{pmatrix}\boldsymbol{A} - \boldsymbol{b}\boldsymbol{g} & \boldsymbol{b}\boldsymbol{g}\\ \boldsymbol{O} & \boldsymbol{A} - \boldsymbol{K}\boldsymbol{C}\end{pmatrix}\begin{pmatrix}\boldsymbol{x}(t)\\ \boldsymbol{e}(t)\end{pmatrix}. \tag{4.35}$$

It can be seen that the poles of the combined system are composed of the observer poles and the regulator poles as the combined dynamics matrix consists of triangular blocks. Thus, the design of state feedback and the state observer are independent from each other which is referred to as *Separation Principle* [27, p. 157-158].

The observer poles are placed to be faster than the poles of the regulator - usually 2 to 6 times faster - which results in the regulator poles dominating the closed-loop behavior [27, p. 152]. The noise of the measurement influences the pole positioning. If the measurement is noisy it is desired to place the poles closer to the regulator poles as this provides some filtering but in this case the influence of the observer poles on the closed-loop response is increased. With less noise the observer poles can be placed faster resulting in higher gain in the matrix $\boldsymbol{K}$ and faster decaying error dynamics in the observer.

Reduced Order Observer

The order of a Luenberger Observer can be reduced if some states are directly measurable leading to a Reduced Order Observer. The state-space model has to be restructured in a way that the state vector $\boldsymbol{x}$ consists of a vector of measurable states $\boldsymbol{y}$ and a vector of hidden states $\boldsymbol{v}$:

$$\boldsymbol{x} = \begin{bmatrix} \boldsymbol{v} \\ \boldsymbol{y} \end{bmatrix}. \tag{4.36}$$

The output equation does contain the identity matrix $\boldsymbol{I}$ as those states are measured under the assumption of perfect measurement without time-lag. The corresponding dynamic system derives to

$$\dot{\boldsymbol{x}} = \left[\begin{array}{c|c} \boldsymbol{A}_{11} & \boldsymbol{A}_{12} \\ \hline \boldsymbol{A}_{21} & \boldsymbol{A}_{22} \end{array}\right] \boldsymbol{x} + \begin{bmatrix} \boldsymbol{b}_1 \\ \hline \boldsymbol{b}_2 \end{bmatrix} u, \tag{4.37}$$

$$\boldsymbol{y} = \left[\begin{array}{c|c} \boldsymbol{0} & \boldsymbol{I} \end{array}\right] \boldsymbol{x}. \tag{4.38}$$

The dynamic system can be reduced by using only hidden states as state vector resulting in eq. (4.39) and incorporating the dynamics of the measured states in the output equation as seen in eq. (4.40).

$$\dot{\boldsymbol{v}} = \underbrace{\boldsymbol{A}_{11}}_{\boldsymbol{A}_{red}} \boldsymbol{v} + \underbrace{\boldsymbol{b}_1 u + \boldsymbol{A}_{12} \boldsymbol{y}}_{\boldsymbol{B}_{red} \boldsymbol{u}_{red}} \tag{4.39}$$

$$\underbrace{\dot{\boldsymbol{y}} - \boldsymbol{A}_{22} \boldsymbol{y} - \boldsymbol{b}_2 u}_{\boldsymbol{y}_{red}} = \underbrace{\boldsymbol{A}_{21}}_{\boldsymbol{C}_{red}} \boldsymbol{v} \tag{4.40}$$

For this system the Luenberger Observer from eq. (4.29) can be applied resulting in the observer described with the equation

$$\dot{\hat{\boldsymbol{v}}} = (\boldsymbol{A}_{11} - \boldsymbol{K}\boldsymbol{A}_{21}) \hat{\boldsymbol{v}} + \boldsymbol{b}_1 u + \boldsymbol{A}_{12} \boldsymbol{y} + \boldsymbol{K} (\dot{\boldsymbol{y}} - \boldsymbol{A}_{22} \boldsymbol{y} - \boldsymbol{b}_2 u). \tag{4.41}$$

The derivative of the output $\dot{\boldsymbol{y}}$ is not known and thus, has to be eliminated. This can be done by substituting $\hat{\boldsymbol{v}} = \boldsymbol{z} + \boldsymbol{K}\boldsymbol{y}$ and $\dot{\hat{\boldsymbol{v}}} = \dot{\boldsymbol{z}} + \boldsymbol{K}\dot{\boldsymbol{y}}$ leading to the transformed dynamics:

$$\dot{\boldsymbol{z}} + \cancel{\boldsymbol{K}\dot{\boldsymbol{y}}} = (\boldsymbol{A}_{11} - \boldsymbol{K}\boldsymbol{A}_{21}) \boldsymbol{z} + (\boldsymbol{A}_{11} - \boldsymbol{K}\boldsymbol{A}_{21}) \boldsymbol{K}\boldsymbol{y} + \boldsymbol{b}_1 u + \boldsymbol{A}_{12} \boldsymbol{y} + \cancel{\boldsymbol{K}\dot{\boldsymbol{y}}} - \boldsymbol{K}\boldsymbol{A}_{22} \boldsymbol{y} - \boldsymbol{K}\boldsymbol{b}_2 u. \tag{4.42}$$

In this equation $\dot{\boldsymbol{y}}$ can be eliminated and a state-space formulation of the Reduced Order Observer can be found where the input vector consists of both the control input u and the measurements $\boldsymbol{y}$:

$$\dot{\boldsymbol{z}} = \underbrace{(\boldsymbol{A}_{11} - \boldsymbol{K}\boldsymbol{A}_{21})}_{\boldsymbol{A}} \boldsymbol{z} + \underbrace{\begin{bmatrix} \boldsymbol{b}_1 - \boldsymbol{K}\boldsymbol{b}_2 & \boldsymbol{A}_{11}\boldsymbol{K} - \boldsymbol{K}\boldsymbol{A}_{21}\boldsymbol{K} + \boldsymbol{A}_{12} - \boldsymbol{K}\boldsymbol{A}_{22} \end{bmatrix}}_{\boldsymbol{B}} \begin{bmatrix} u \\ \boldsymbol{y} \end{bmatrix}, \tag{4.43}$$

$$\hat{\boldsymbol{v}} = \underbrace{\begin{bmatrix} \boldsymbol{I} \end{bmatrix}}_{\boldsymbol{C}} \boldsymbol{z} + \underbrace{\begin{bmatrix} \boldsymbol{0} & \boldsymbol{K} \end{bmatrix}}_{\boldsymbol{D}} \begin{bmatrix} u \\ \boldsymbol{y} \end{bmatrix}. \tag{4.44}$$

The dynamics of this system can be designed similar to the standard Luenberger Observer. For every hidden state in $\boldsymbol{v}$ one pole has to be placed. Those poles can be places arbitrarily if the full model is observable [22, p. 366]. This observer bases on the assumption of perfect measurement which is not given in most real world applications. As previously described the poles need to be tuned to the sensor noise as fast observer poles with high measurement noise can lead to a noise corrupted state estimation signal.

Kalman Filter

For the Luenberger Observer a known and ideal state-space model is assumed. However, in many application the model is not perfectly known or simplifies a nonlinear relation with a linearization. Also the measurement is often corrupted by noise due to imperfect sensors. These effects can be considered as noise on the system. For a discrete model this noise can be treated as a random variable which allows to solve the state reconstruction in a probabilistic framework. The underlying possibly time-variant model can be seen in eqs. (4.45) and (4.46) with process noise $\boldsymbol{w}_k$ and measurement noise $\boldsymbol{v}_k$. The matrices of the dynamical system are discretised and are assumed to be constant over one time step k.

$$\boldsymbol{x}_k = \boldsymbol{A}_{k-1}\boldsymbol{x}_{k-1} + \boldsymbol{b}_{k-1}u_{k-1} + \boldsymbol{w}_{k-1} \tag{4.45}$$

$$\boldsymbol{y}_k = \boldsymbol{C}_k\boldsymbol{x}_k + \boldsymbol{D}_k u_k + \boldsymbol{v}_k \tag{4.46}$$

For the Kalman Filter several assumption on the noise are made. All instances of the process noise $\boldsymbol{w}_k$ and measurement noise $\boldsymbol{v}_k$ are considered independent. Both are assumed to be drawn from a multivariate Gaussian distribution with zero-mean with process covariance matrix $\boldsymbol{Q}_k$ and measurement covariance matrix $\boldsymbol{R}_k$ [35, p. 124].

$$\boldsymbol{w}_k \sim \mathcal{N}(0, \boldsymbol{Q}_k)$$
$$\boldsymbol{v}_k \sim \mathcal{N}(0, \boldsymbol{R}_k)$$

Subsequently, the state $\boldsymbol{x}_k$ will also follow a Gaussian distribution. To estimate this state the Kalman Filter algorithm uses a two step approach in such a way that the mean quadratic estimation error is minimized [19]. First the current estimate is propagated one time step to calculate an a priori estimate of the state which is called prediction. Afterwards, the prediction is refined with the current measurement to obtain the a posteriori estimate. This step is called update.

The algorithm starts with an initial state estimate $\hat{\boldsymbol{x}}_{0|0}$ which also follows a Gaussian distribution with initial covariance $\boldsymbol{P}_{0|0}$. This estimate is propagated to the next time step using the dynamics of the underlying process from eq. (4.45). The state prediction is straight forward and can be seen in eq. (4.47). The covariance matrix is transformed according to the propagation with the dynamics matrix $\boldsymbol{A}_k$ and the modeled process noise is added. Basics on the propagation of Gaussian processes can be found in [35, p. 107-123]. The calculation can be seen in eq. (4.47). As no observations are included in this step the covariance is usually increasing which corresponds an increasing uncertainty.

$$\hat{\boldsymbol{x}}_{k|k-1} = \boldsymbol{A}_{k-1}\hat{\boldsymbol{x}}_{k-1|k-1} + \boldsymbol{B}_{k-1}u_{k-1} \tag{4.47}$$

$$\boldsymbol{P}_{k|k-1} = \boldsymbol{A}_{k-1}\boldsymbol{P}_{k-1|k-1}\boldsymbol{A}_{k-1}^T + \boldsymbol{Q}_{k-1} \tag{4.48}$$

During the update step the state prediction is corrected based on the current measurement observation $\boldsymbol{y}_k$. A new optimal Kalman gain $\boldsymbol{K}_k$ is calculated following eq. (4.49). The difference between measurement and predicted measurement multiplied with the Kalman gain is used to correct the state estimation resulting in an a posteriori estimate $\hat{\boldsymbol{x}}_{k|k}$ following eq. (4.50). Equation (4.51) displays the update of the covariance matrix.

$$\boldsymbol{K}_k = \boldsymbol{P}_{k|k-1}\boldsymbol{C}_k^T\left(\boldsymbol{C}_k\boldsymbol{P}_{k|k-1}\boldsymbol{C}_k^T + \boldsymbol{R}_k\right)^{-1} \tag{4.49}$$

$$\hat{\boldsymbol{x}}_{k|k} = \hat{\boldsymbol{x}}_{k|k-1} + \boldsymbol{K}_k\left(\boldsymbol{y}_k - \boldsymbol{C}_k\hat{\boldsymbol{x}}_{k|k-1} - \boldsymbol{D}_k u_k\right) \tag{4.50}$$

$$\boldsymbol{P}_{k|k} = (\boldsymbol{I} - \boldsymbol{K}_k\boldsymbol{C}_k)\boldsymbol{P}_{k|k-1} \tag{4.51}$$

One of the advantages of this algorithm over the Luenberger Observer is that for known process and measurement noises no parameter tuning is necessary whereas with the Luenberger Observer the poles have to be set. The measurement noise covariance matrix can be parameterized using the sensor characteristics in most cases. Problematic is that the process noise is not that easy to determine and often ends up as a tuning parameter. Estimating this matrix is topic of recent research for example one approach is to use an autocovariance least squares method [24][30]. These methods are exceeding the scope of this thesis and thus the process noise covariance matrix has to be manually tuned.

Extended Kalman Filter

The standard Kalman Filter algorithm bases on the linear system dynamics from eqs. (4.45) and (4.46). To estimate the states of a nonlinear systems of the form

$$\boldsymbol{x}_k = \boldsymbol{f}_{k-1}(\boldsymbol{x}_{k-1}, u_{k-1}) + \boldsymbol{w}_{k-1} \tag{4.52}$$
$$\boldsymbol{y}_k = \boldsymbol{h}_k(\boldsymbol{x}_k, u_k) + \boldsymbol{v}_k \tag{4.53}$$

the algorithm can be adopted resulting in the Extended Kalman Filter which can be considered the standard of nonlinear state estimation [35, p. 396]. The general idea is to use the nonlinear system equations for the prediction of the state and use this prediction to linearize the equations for the update step.

The prediction of the state vector can be done using the nonlinear dynamic equation from eq. (4.52) resulting in eq. (4.54). To propagate the covariance matrix the linearization of the system dynamics is needed and displayed in eq. (4.55). With this linearized system the covariance can be computed the same way as for the standard Kalman Filter see eq. (4.56).

$$\hat{\boldsymbol{x}}_{k|k-1} = \boldsymbol{f}_{k-1}\left(\hat{\boldsymbol{x}}_{k-1|k-1}, u_{k-1}\right) \tag{4.54}$$
$$\boldsymbol{A}_{k-1} = \left.\frac{\partial \boldsymbol{f}_{k-1}}{\partial \boldsymbol{x}}\right|_{\hat{\boldsymbol{x}}_{k-1|k-1}, u_{k-1}} \tag{4.55}$$
$$\boldsymbol{P}_{k|k-1} = \boldsymbol{A}_{k-1}\boldsymbol{P}_{k-1|k-1}\boldsymbol{A}_{k-1}^T + \boldsymbol{Q}_{k-1} \tag{4.56}$$

For the update step the output equation of the linear system has to be linearized. Equation (4.57) shows the linearization where the predicted state is used as the linearization point. With the linearized output equation the Kalman gain and the covariance can be updated with the same eqs. (4.58) and (4.60) analog to the linear Kalman filter. The state update in eq. (4.59) utilizes the nonlinear output relation to correct the estimation.

$$\boldsymbol{C}_k = \left.\frac{\partial \boldsymbol{h}_k}{\partial \boldsymbol{x}}\right|_{\hat{\boldsymbol{x}}_{k|k-1}, u_k} \tag{4.57}$$
$$\boldsymbol{K}_k = \boldsymbol{P}_{k|k-1}\boldsymbol{C}_k^T\left(\boldsymbol{C}_k\boldsymbol{P}_{k|k-1}\boldsymbol{C}_k^T + \boldsymbol{R}_k\right)^{-1} \tag{4.58}$$
$$\hat{\boldsymbol{x}}_{k|k} = \hat{\boldsymbol{x}}_{k|k-1} + \boldsymbol{K}_k\left[\boldsymbol{y}_k - \boldsymbol{h}_k\left(\hat{\boldsymbol{x}}_{k|k-1}, u_k\right)\right] \tag{4.59}$$
$$\boldsymbol{P}_{k|k} = (\boldsymbol{I} - \boldsymbol{K}_k\boldsymbol{C}_k)\boldsymbol{P}_{k|k-1} \tag{4.60}$$

One weakness of this approach is the linear propagation of the covariance matrix which leads to significant problems for systems with severe nonlinearities as the Extended Kalman Filter tends to underestimate the covariance matrix [15]. The error due to the linearization can be reduced by iterating the Extended Kalman Filter multiple times per time step and by doing so refining the point of linearization [35, p. 412]. This improvement is achieved at cost of computation time and also does not fix the problem of model inaccuracies. Another similar approach is to utilize a second order Taylor expansion instead of the first order approximation used for the Extended Kalman Filter.

Steady-State Kalman Filter

The previously introduced Kalman Filters are computationally expensive during run-time as a matrix inversion is necessary to compute the Kalman gain. To reduce the computational burden a Steady-State Kalman Filter can be used where most of the computation can be done beforehand. To derive this version of the Kalman Filter the model is restricted to a time-invariant linear model from where the time indices are replaced with the index d to mark that the system is discretised:

$$\boldsymbol{x}_k = \boldsymbol{A}_\mathrm{d}\boldsymbol{x}_{k-1} + \boldsymbol{b}_\mathrm{d}u_{k-1} + \boldsymbol{w}_{k-1}, \tag{4.61}$$
$$\boldsymbol{y}_k = \boldsymbol{C}_\mathrm{d}\boldsymbol{x}_k + \boldsymbol{D}_\mathrm{d}u_k + \boldsymbol{v}_k. \tag{4.62}$$

Looking at the equations from the Kalman Filter necessary to calculate the Kalman gain with the time-invariant model

$$\boldsymbol{P}_{k|k-1} = \boldsymbol{A}_d \boldsymbol{P}_{k-1|k-1} \boldsymbol{A}_d^T + \boldsymbol{Q}, \tag{4.63}$$

$$\boldsymbol{K}_k = \boldsymbol{P}_{k|k-1} \boldsymbol{C}_d^T \left(\boldsymbol{C}_d \boldsymbol{P}_{k|k-1} \boldsymbol{C}_d^T + \boldsymbol{R} \right)^{-1}, \tag{4.64}$$

$$\boldsymbol{P}_{k|k} = (\boldsymbol{I} - \boldsymbol{K}_k \boldsymbol{C}_d) \boldsymbol{P}_{k|k-1} \tag{4.65}$$

one can be seen that the calculations do not depend on the measurements but are just iterations based on the matrices of the time-independent model. The Steady-State Kalman Filter can be found if the Kalman gain converges after sufficient iterations:

$$\lim_{k \to \infty} \boldsymbol{K}_k = \boldsymbol{K}_\infty. \tag{4.66}$$

With this Kalman gain the Steady-State Kalman Filter can be formulated in a classical observer form by inserting the state update from eq. (4.50) into the state prediction in eq. (4.47) of the standard Kalman Filter which yields:

$$\hat{\boldsymbol{x}}_{k+1|k} = \boldsymbol{A}_\mathrm{d} \hat{\boldsymbol{x}}_{k|k-1} + \boldsymbol{B}_\mathrm{d} u_k + \boldsymbol{A}_\mathrm{d} \boldsymbol{K}_\infty \left(\boldsymbol{y}_k - \boldsymbol{C}_\mathrm{d} \hat{\boldsymbol{x}}_{k|k-1} - \boldsymbol{D}_\mathrm{d} u_k \right). \tag{4.67}$$

This observer only calculates an estimate for the state at time k with the sensor information of prior time steps up to $k-1$. In order to refine this estimate with the current measurement one can use eq. (4.50) but with the steady-state gain which results in the steady-state update equation:

$$\hat{\boldsymbol{x}}_{k|k} = \hat{\boldsymbol{x}}_{k|k-1} + \boldsymbol{K}_\infty \left(\boldsymbol{y}_k - \boldsymbol{C}_\mathrm{d} \hat{\boldsymbol{x}}_{k|k-1} - \boldsymbol{D}_\mathrm{d} u_k \right). \tag{4.68}$$

Assuming that this steady-state gain does exist one can infer that the covariance matrix also has to converges which implies that $\boldsymbol{P}_{k|k-1} = \boldsymbol{P}_{k+1|k} = \boldsymbol{P}_\infty$. One can insert eq. (4.65) and eq. (4.64) into eq. (4.63) to obtain the Discrete Algebraic Ricatti Equation (DARE):

$$\boldsymbol{P}_\infty = \boldsymbol{A}_\mathrm{d} \boldsymbol{P}_\infty \boldsymbol{A}_\mathrm{d}^T - \boldsymbol{A}_\mathrm{d} \boldsymbol{P}_\infty \boldsymbol{C}_\mathrm{d}^T \left(\boldsymbol{C}_\mathrm{d} \boldsymbol{P}_\infty \boldsymbol{C}_\mathrm{d}^T + \boldsymbol{R} \right)^{-1} \boldsymbol{C}_\mathrm{d} \boldsymbol{P}_\infty \boldsymbol{A}_\mathrm{d}^T + \boldsymbol{Q}. \tag{4.69}$$

The DARE has a unique positive definite solution and thus, the corresponding Steady-State Kalman Filter is stable if and only if the conditions

- $(\boldsymbol{A}, \boldsymbol{C})$ is detectable
- $(\boldsymbol{A}, \sqrt{\boldsymbol{Q}})$ is stabilizable where $\sqrt{\boldsymbol{Q}} \sqrt{\boldsymbol{Q}}^T = \boldsymbol{Q}$

are met [19, p. 105]. Stabilizability (def. 4.3) and Detectability (def. 4.4) are basically weaker notions of Controllability and Observability.

Definition 4.3 (Stabilizability)**.** "If a system is controllable or stable, then it is also stabilizable. If a system is uncontrollable or unstable, then it is stabilizable if its uncontrollable modes are stable." [35, p. 44].

Definition 4.4 (Detectability)**.** "If a system is observable or stable, then it is also detectable. If a system is unobservable or unstable, then it is detectable if its unobservable modes are stable" [35, p. 45].

If the system fulfills this condition and the DARE can be solved the Kalman gain can be directly computed with the converged covariance matrix:

$$\boldsymbol{K}_\infty = \boldsymbol{P}_\infty \boldsymbol{C}_\mathrm{d}^T \left(\boldsymbol{C}_\mathrm{d} \boldsymbol{P}_\infty \boldsymbol{C}_\mathrm{d}^T + \boldsymbol{R} \right)^{-1}. \tag{4.70}$$

The Steady-State Kalman Filter improves the run-time complexity of the state estimation significantly as the calculation of the gain can be done offline. However, this comes at the cost of flexibility because the capability to handle time-varying systems gets lost. Additionally this algorithm loses the optimality especially for the first time steps. Still, the Steady-State Kalman Filter performs nearly as well as the linear Kalman Filter and the results are often nearly indistinguishable [35, p. 198]. It can be concluded that the Steady-State Kalman Filter is degrading the Kalman Filter algorithm to a point where it can be seen as a design principle for a Luenberger Observer.

4.3.3 Observer Based Control of the Flexible Inverted Pendulum

As previously concluded the PD+ controller is not adequate to control the inverted pendulum with structural dynamics sufficiently. This results from the feedback of an vibration prone signal which caused an excitation affected by this vibrations. Therefore, control schemes with an observer and state feedback can be used to control based on the angle of the imaginary, rigid pendulum. Two opposing approaches with observers and state regulators are implemented for this thesis and are discussed in the following section.

1. The first approach bases on simplicity and models only the first and most dominant resonance frequency. This model can be observed well with a reduced observer of order two and the two estimated states can be used for a PD+ controller.

2. In contrast the second approach utilizes the complete knowledge of the system and models the complete structural dynamics and actor dynamics. This process can be observer with a Kalman Filter of order 9 and controller with either a LQR or PD+ controller.

Applied Second Order Observer

As already mentioned the idea of this control approach is to reduce the system dynamics as far as possible while still including some structural dynamics. This is done by modeling only first resonance frequency assuming that it is the dominating resonance. The other resonances and anti-resonances are neglected. The structural dynamics model of one resonance frequency can be modeled with a second order system with the transfer function

$$G_{\text{s,red}}(s) = \frac{1}{\frac{1}{\omega^2}s^2 + \frac{2D}{\omega}s + 1}. \tag{4.71}$$

This transfer function can be brought to CCF which results in the state-space model

$$\dot{\boldsymbol{x}}_{\text{s,red}} = \begin{bmatrix} 0 & 1 \\ -\omega^2 & -2D\omega \end{bmatrix} \boldsymbol{x}_{\text{s,red}} + \begin{bmatrix} 0 \\ 1 \end{bmatrix} u_{\text{s,red}}, \tag{4.72}$$

$$y_{\text{s,red}} = \begin{bmatrix} 1 & 0 \end{bmatrix} \boldsymbol{x}_{\text{s,red}}, \tag{4.73}$$

$$\dot{y}_{\text{s,red}} = \begin{bmatrix} 0 & 1 \end{bmatrix} \boldsymbol{x}_{\text{s,red}}. \tag{4.74}$$

This structural dynamics model can be combined with the linearized dynamics of the inverted pendulum from eq. (2.3). The input of the second order model is the angle of the inverted pendulum $u_{\text{s,red}} = \varphi$. The combined model of the system derives to

$$\dot{\boldsymbol{x}} = \left[\begin{array}{cc|cc} 0 & 1 & 0 & 0 \\ \frac{mgl}{I_0} & 0 & 0 & 0 \\ \hline 0 & 0 & 0 & 1 \\ \omega^2 & 0 & -\omega^2 & -2D\omega \end{array}\right] \boldsymbol{x} + \left[\begin{array}{c} 0 \\ \frac{1}{I_0} \\ \hline 0 \\ 0 \end{array}\right] u. \tag{4.75}$$

The parameters ω and D are chosen to match the damping and eigenfrequency of the first resonance. It is assumed that the angle and angular velocity of the inverted pendulum with simplified structural dynamics can be measured directly and thus $y_1 = y_{\text{s,red}}$ and $y_2 = \dot{y}_{\text{s,red}}$. With the definition of the angular velocity in eq. (4.74) the output equation of the process model can be described by

$$\boldsymbol{y} = \left[\begin{array}{cc|cc} 0 & 0 & 1 & 0 \\ 0 & 0 & 0 & 1 \end{array}\right] \boldsymbol{x}. \tag{4.76}$$

In the measurement equation it can be seen the last two states are measured directly and thus, a reduced order observer is justified. This observer estimates the first and second state which correspond to the angle and angular velocity of the rigid inverted pendulum. This system is observable which can be proven using the Hautus criterion. Subsequently the poles of the Reduced Order Observer can be places arbitrarily. The noise on the measurement is considered relatively low and therefore fast poles can be placed without further problems. The poles are set 5 times faster than the resulting regulator poles which is on the faster side of the recommended range of 3 to 6.

The estimated states of the observer are used as an improved input for the PD+ controller. Combined with the Reduced Order Observer this can be interpreted as state feedback on the gravity compensated reduced system with the dynamics

$$\dot{\boldsymbol{x}}_{\text{red}} = \begin{bmatrix} 0 & 1 \\ 0 & 0 \end{bmatrix} \boldsymbol{x}_{\text{red}} + \begin{bmatrix} 0 \\ \frac{1}{I_0} \end{bmatrix} u. \tag{4.77}$$

Adding the control law of the PD controller one obtains a new reduced dynamical system:

$$\dot{\boldsymbol{x}}_{\text{red}} = \begin{bmatrix} 0 & 1 \\ -\frac{P}{I_0} & -\frac{D}{I_0} \end{bmatrix} \boldsymbol{x}_{\text{red}}. \tag{4.78}$$

The PD+ gains are tuned to match the desired closed-loop performance in the step response and the disturbance impulse. More decisive is the disturbance rejection as an observer does not include a model for disturbances which cannot be measured. Therefore, the controller gains are tuned to match the requirements on the disturbance impulse response. Based on the chosen gains the resulting regulator poles $p_{\text{r},1/2}$ are calculated from gravity compensated, PD controlled system:

$$p_{\text{r},1/2} = \text{eig}\left(\begin{bmatrix} 0 & 1 \\ -\frac{P}{I_0} & -\frac{D}{I_0} \end{bmatrix} \right). \tag{4.79}$$

Based on these poles the observer poles $\boldsymbol{p}_{\text{o}}$ are set with a 5 times larger real part than the fastest regulator pole. As the PLACE function in MATLAB cannot place two poles in the exact same locations the poles are set 5 % left and right of the ideal pole position which yields

$$\boldsymbol{p}_{\text{o}} = 5 \min\left(\text{Re}\left\{\boldsymbol{p}_{\text{r}}\right\}\right) \begin{bmatrix} 1.05 \\ 0.95 \end{bmatrix}. \tag{4.80}$$

Table 4.4 contains the gains that are found for the PD+ controller and the resulting observer poles. It can be seen that the gains of the PD+ controller are higher compared to the control without an observer. The observer itself reduces the aggressiveness of the closed-loop system as additional poles are introduced. Therefore, the controller gains have to be increased.

Table 4.4: Gains of the PD+ controller and the corresponding observer poles for the control scheme with a Reduced Order Observer

Parameter	Value
K_{P}	4750
K_{D}	720
p_o	$\left[-31.5122, -28.5110\right]$

The resulting matrices forming the Reduced Order Observer can be found in appendix A.

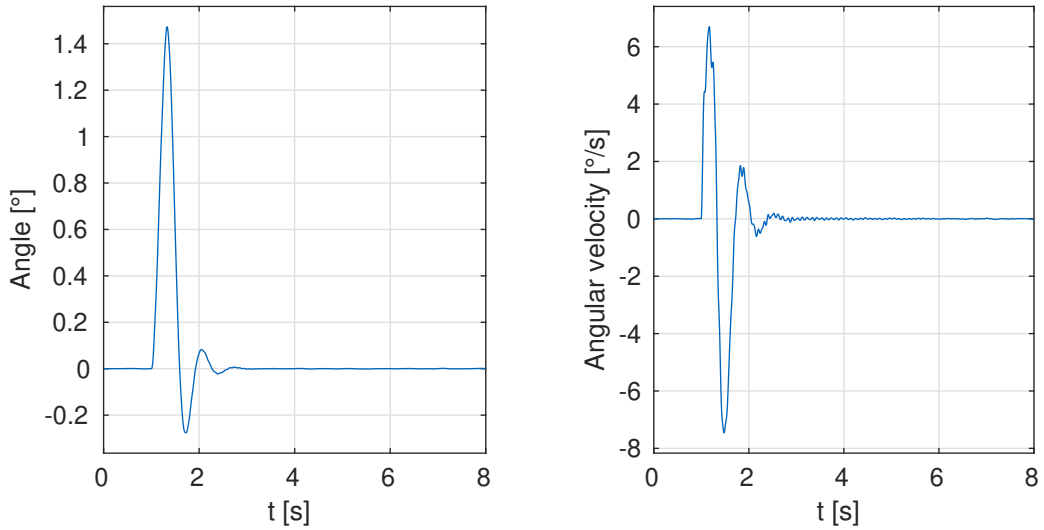

Figure 4.20: Response of the closed-loop system with the Reduced Order Observer combined with PD+ control to a disturbance impulse

The impulse response of the closed-loop system can be seen in fig. 4.20. It can be seen that the performance criteria form eqs. (4.3) and (4.4) are fulfilled. The step response is displayed in fig. 4.21 where one can see that the performance requirements from eq. (4.1) and eq. (4.2) are met. In both figures some vibrations in the angular velocity can be seen which are more damped compared to the PD+ controller alone.

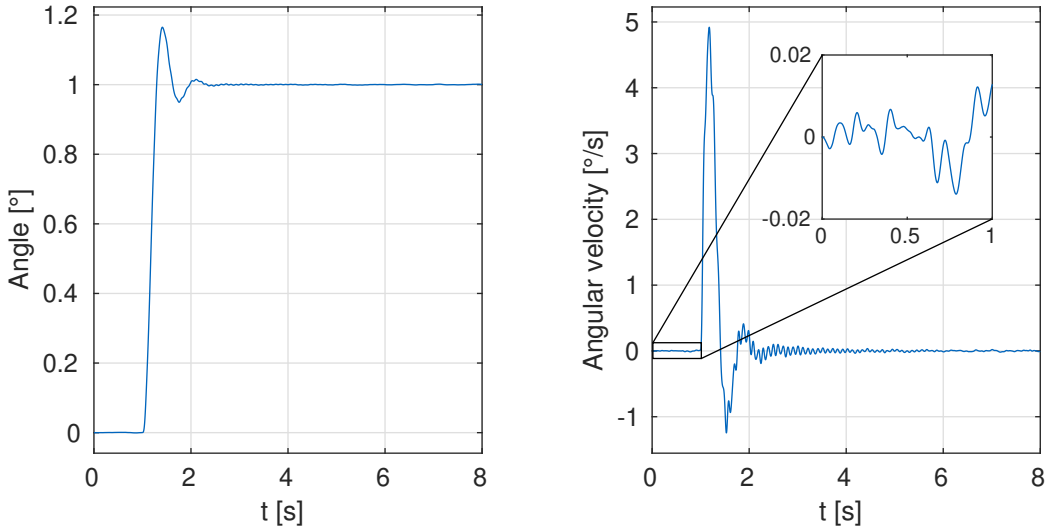

Figure 4.21: Step response of the closed-loop system with the Reduced Order Observer combined with PD+ control

In the step response plot in fig. 4.21 the angular velocity during the first second is enlarged. One can see that the angular velocity contains a small amount of interference. During this time span no disturbance or reference changes appear in the simulation and the simulation is run without varying the initial position from the upright position. Thus, the interference of the angular velocity results from the quantization and measurement noise. For the Reduced Order Observer the poles are placed fast and by doing so the error convergence is valued more important than the filtering of the measurement noise. The absolute value of this interference is below $0.0139\,^{\circ}\,\mathrm{s}^{-1}$ compared to $0.0123\,^{\circ}\,\mathrm{s}^{-1}$ for the PD+ controller which is increased but acceptable.

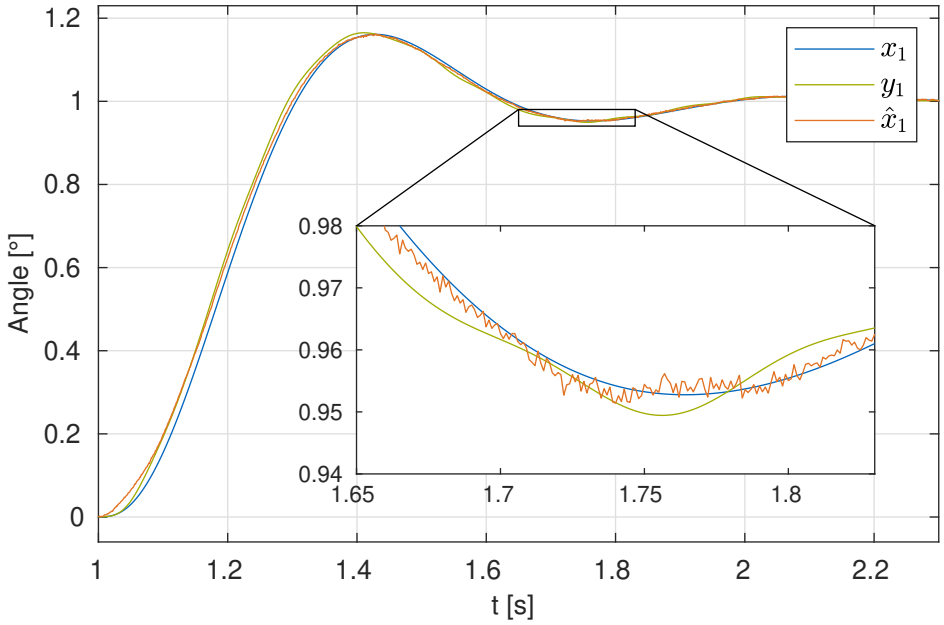

Figure 4.22: Step response of the control scheme with the Reduced Order Observer. The angle of the rigid pendulum x_1 and the angle of the pendulum with structural dynamics y_1 is compared to the estimated angle $\hat{x}_1$

Figure 4.22 displays the step response in detail. The plot contains the angle of the rigid pendulum x_1 and the angle of the pendulum with structural dynamics y_1 before quantization and noise is added. One can see that the output y_1 visibly oscillates around x_1. Additionally the estimated angle $\hat{x}_1$ is displayed. This estimate follows x_1 accurately at most times and contains less vibration as y_1. The estimate is affected by noise which is considered admissible.

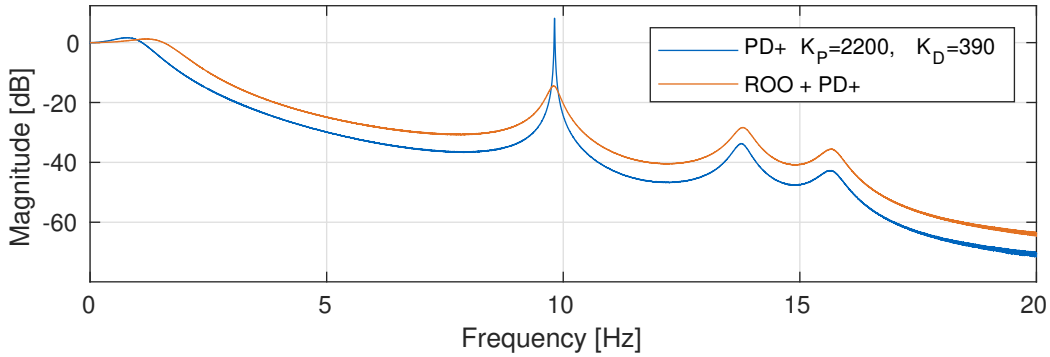

Figure 4.23: Identified reference transfer function for the closed-loop system with the Reduced Order Observer combined with PD+ control in comparison to the aggressive, standalone PD+ controller

Figure 4.23 displays the identified reference transfer function of the Reduced Order Observer control scheme in comparison to the PD+ controller. It can be seen that the scheme with the Reduced Order Observer performs better in measures of the bandwidth. The bandwidth is improved to 1.87 Hz compared to 1.34 Hz with the PD+ controller. Summarizing one can see that the control scheme with the Reduced Order Observer meets all design requirements with only one minor disadvantage due to the slightly increased noise on the system outputs.

The vibration behavior is improved by using the Reduced Order Observer which can be seen in the disturbance transfer function fig. 4.24. The peak corresponding to the first resonance frequency of the structure is decreased from −51 dB to −80 dB which corresponds to a reduction by about 96 %. The peaks of the second and third resonance of the structure are not significantly changed.

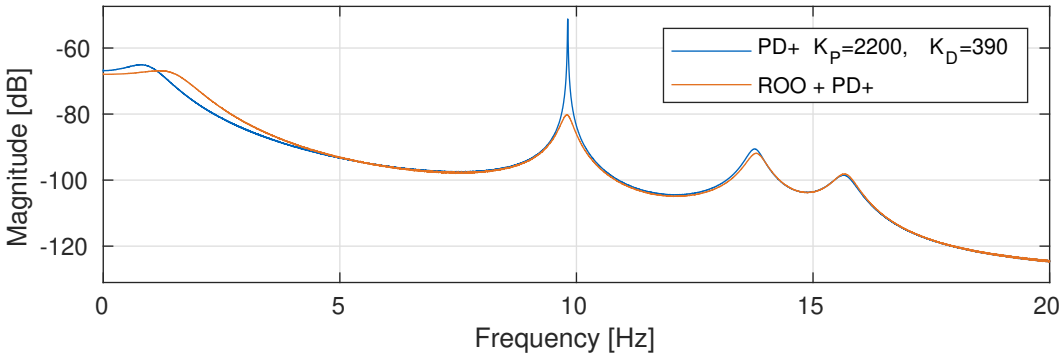

Figure 4.24: Identified disturbance transfer function for the closed-loop system with the Reduced Order Observer combined with PD+ control in comparison to the aggressive, standalone PD+ controller

Figure 4.25 contains the magnitude of the structure peaks in the disturbance transfer function. It can be seen that for perturbations in the system dynamics the Reduced Order Observer still improved the vibration behavior. The damping of the first resonance frequency is significantly increased while the higher resonances remain nearly unchanged. This fact does match with theory as the observer model contained only the first resonance frequency. Overall this control scheme performed well considering the reduced process model.

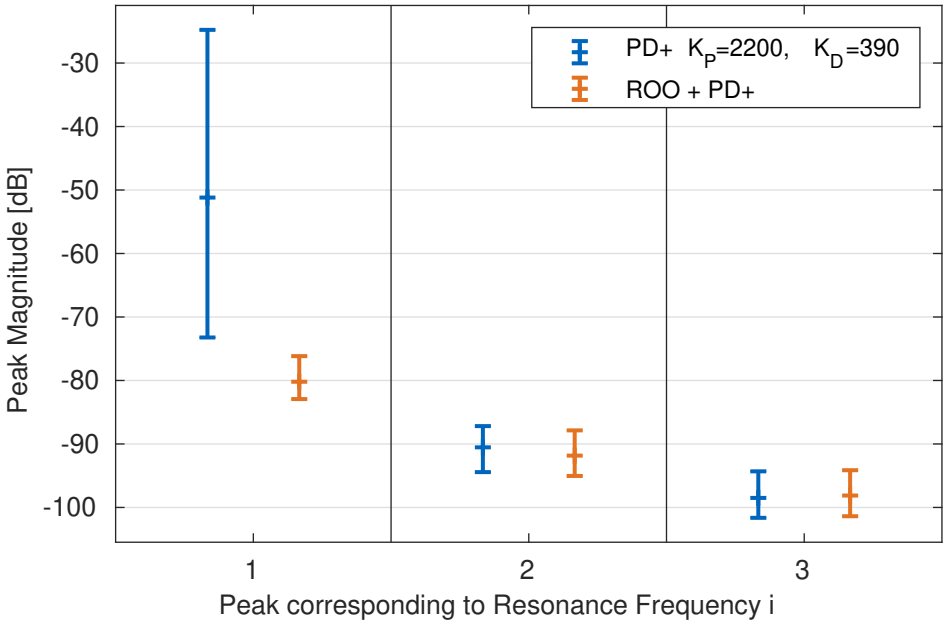

Figure 4.25: Vibration behavior for perturbed system dynamics

Applied Steady-State Kalman Filter

As a second approach the complete model knowledge is used for the control design. Thus, a model of the complete system including the full structural dynamics and the actor dynamics is derived. This system is of order 9 and will be discussed in the beginning. For state feedback a Linear Quadratic Regulator is designed and compared to the capabilities of a PD+ controller. To estimate the state vector a Kalman Filter is used. The system could be modeled nonlinear and estimated with the Extended Kalman Filter Algorithm which would result in a low modeling error but high computational burden during runtime. As the system is supposed to operate close to the upright position the error due to linearization around this position is considered insignificant and thus, the downsides of the Extended Kalman Filter

are dominating the benefits. Subsequently, a Steady-State Kalman Filter is implemented which bases on a linearized system.

To take full advantage of the Kalman Filter the system is modeled to contain as much information as possible. The actuator dynamics can be easily integrated by converting the actuator model into state-space:

$$\dot{y}_{\text{act}} = \dot{x}_{\text{act}} = -\frac{1}{T_{\text{act}}} x_{\text{act}} + \frac{1}{T_{\text{act}}} u. \tag{4.81}$$

This state-space model can be merged with the linearized model from eq. (3.11) which yields the dynamics of the full dynamic equation

$$\dot{\boldsymbol{x}}_{\text{f}} = \left[\begin{array}{c|cc|ccc} -\frac{1}{T_{\text{act}}} & 0 & 0 & 0 & \dots & 0 \\ \hline 0 & 0 & 1 & 0 & \dots & 0 \\ \frac{1}{I_0} & \frac{mgl}{I_0} & 0 & 0 & \dots & 0 \\ \hline \multicolumn{1}{c|}{\multirow{2}{*}{$\boldsymbol{0}$}} & \multicolumn{2}{c|}{\multirow{2}{*}{$\boldsymbol{b}_{\text{s}}$}} & \multicolumn{3}{c}{\multirow{2}{*}{$\boldsymbol{0}$}} \\ & & & & & \\ \multicolumn{1}{c|}{} & \multicolumn{2}{c|}{} & \multicolumn{3}{c}{$\boldsymbol{A}_{\text{s}}$} \end{array}\right] \underbrace{\left[\begin{array}{c} x_{\text{act}} \\ \hline \varphi \\ \dot{\varphi} \\ \hline \multirow{2}{*}{$\boldsymbol{x}_{\text{s}}$} \\ \\ \end{array}\right]}_{\boldsymbol{x}_{\text{f}}} + \left[\begin{array}{c} \frac{1}{T_{\text{act}}} \\ \hline 0 \\ 0 \\ \hline \boldsymbol{0} \end{array}\right] u. \tag{4.82}$$

Note that the input u is now the input of the actuator model and not the torque directly affecting the inverted pendulum. Using the matrices $\boldsymbol{C}_{\text{lin}}$ and $\boldsymbol{d}$ from eq. (3.16) the output equation of the full model derives to

$$\boldsymbol{y}_{\text{f}} = \left[\begin{array}{c|c} \boldsymbol{d} & \boldsymbol{C}_{\text{lin}} \end{array}\right] \boldsymbol{x}_{\text{f}}. \tag{4.83}$$

For this linear time-invariant system a Linear Quadratic Regulator is designed. As the cost functional can be scaled without changing the resulting regulator the weight of the input signal is fixed to $R = 1$. The goal of this regulator is to control the system with reduced vibrations of the output and thus, the cost functional from eq. (4.24) is transformed to weight the output $\boldsymbol{y}_f$ with the matrix $\tilde{\boldsymbol{Q}}$:

$$J = \int_0^\infty \boldsymbol{x}^T \underbrace{\boldsymbol{C}^T \tilde{\boldsymbol{Q}} \boldsymbol{C}}_{\boldsymbol{Q}} \boldsymbol{x} + u^2 \, \mathrm{d}t. \tag{4.84}$$

The weight $\tilde{\boldsymbol{Q}}$ is set by punishing the first sensor output which corresponds to the angle measured by the IMU. The measurement noise matrix $\boldsymbol{R}$ of the Kalman Filter is parameterized with the noise variance of the measurements. The process noise matrix $\boldsymbol{Q}$ introduces low noise for the states of the structural dynamics model and the actuator model while assuming higher noise on the states of the inverted pendulum. The parameterization can be seen in table 4.5. The resulting matrices can be found in appendix B.

Table 4.5: Parameters of the Kalman Filter and LQR controller

Parameter	Value
$\boldsymbol{Q}$	$\mathrm{diag}\left(\left[\begin{array}{ccccccc} 1\times10^{-12}, & 1\times10^{-4}, & 1\times10^{-3}, & 1\times10^{-12}, & \dots & 1\times10^{-12} \end{array}\right]\right)$
$\boldsymbol{R}$	$\mathrm{diag}\left(\left[\begin{array}{ccc} 5.7245\times10^{-9}, & 1.3231\times10^{-6}, & 1.6849\times10^{-3} \end{array}\right]\right)$
$\tilde{\boldsymbol{Q}}$	$\mathrm{diag}\left(\left[\begin{array}{ccc} 1.8\times10^{7}, & 0, & 0 \end{array}\right]\right)$

The critical performance measure was the bandwidth of the closed-loop system. Figure 4.26 shows the reference transfer function with a zoomed area around the cutoff frequency. It can be seen that the system controlled with the Kalman Observer and the Linear Quadratic Regulator has a similar bandwidth as the PD+ controlled system.

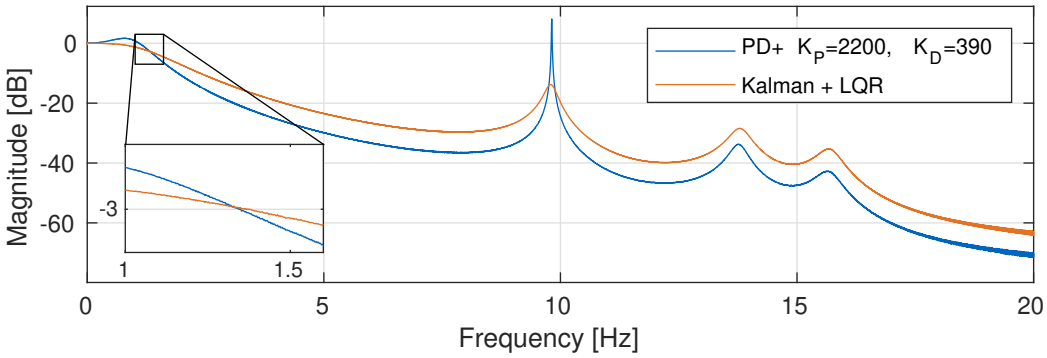

Figure 4.26: Identified reference transfer function for the closed-loop system with the Steady-State Kalman Filter combined with the Linear Quadratic Regulator in comparison to the standalone PD+ controller

The impulse response is shown in fig. 4.27. It can be seen that the performance requirements are outperformed. The system is strongly damped and has less overshoot in comparison to the system controlled with the PD+ controller. Also it can be noticed that the angle converges very fast to the upright position. About 1.1 s after the impulse the angle is already back to a $\pm 0.005^\circ$ error band. In the angular velocity vibrations with a low and decaying amplitude can be seen.

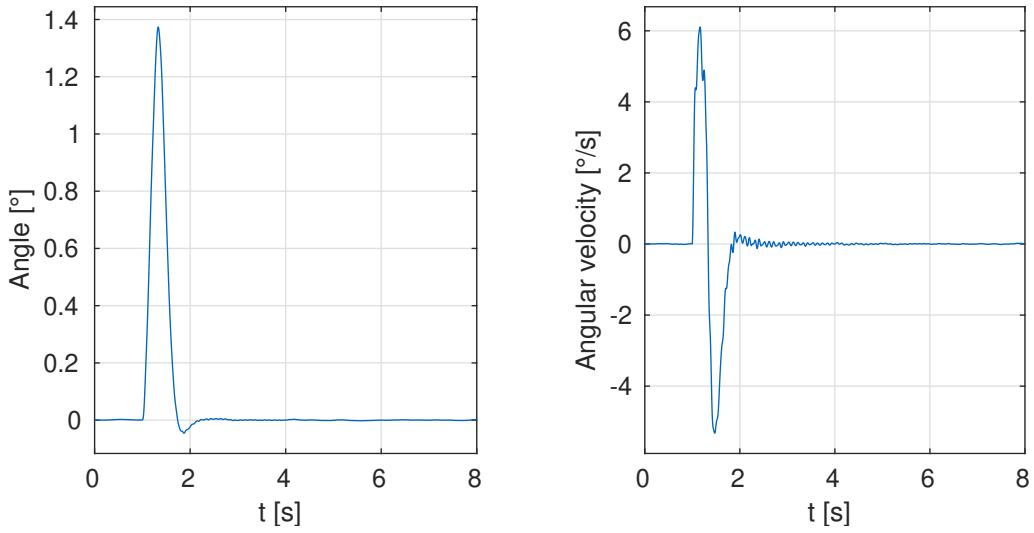

Figure 4.27: Disturbance impulse response of the model controlled with a Linear Quadratic Regulator and a Steady-State Kalman Filter

Figure 4.28 displays the step response of the system with Kalman Filter and Linear Quadratic Regulator. It can be seen that the overshoot is about 3.1 % and thus, far below the allowed overshoot from eq. (4.2). The settling time of 0.4 s is low compared to eq. (4.1). It can be concluded that although the bandwidth is similar to the PD+ controlled system the step and impulse responses are vastly improved. In the step response in the measured angular velocity a vibration is clearly visible although it decays quickly.

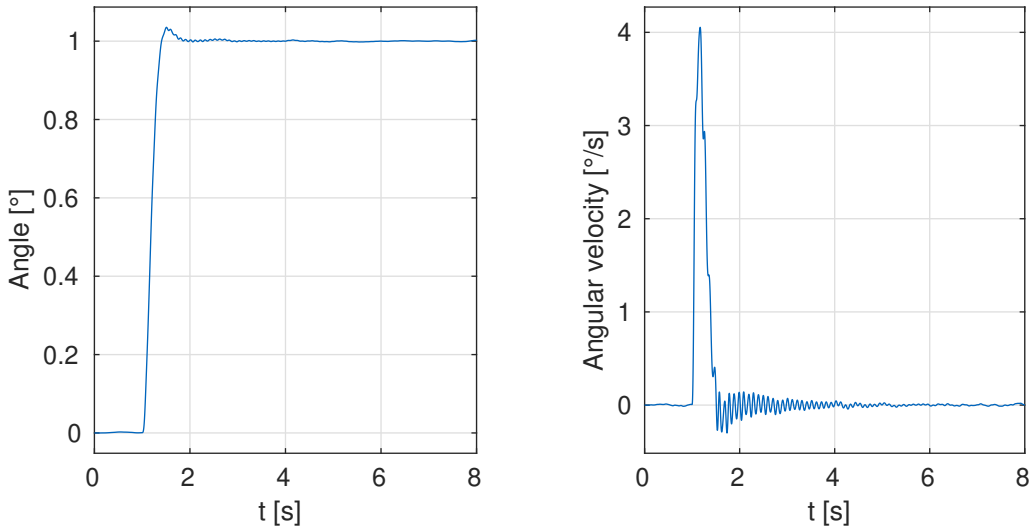

Figure 4.28: Step response of the model controlled with a Linear Quadratic Regulator and a Steady-State Kalman Filter

The disturbance transfer function can be seen in fig. 4.29. In comparison to the standalone PD+ controller the control scheme with the Kalman Filter has a significantly reduced peak corresponding to the first structure resonance frequency. While the peak of the second resonance frequency is slightly damped the last resonance is not changed.

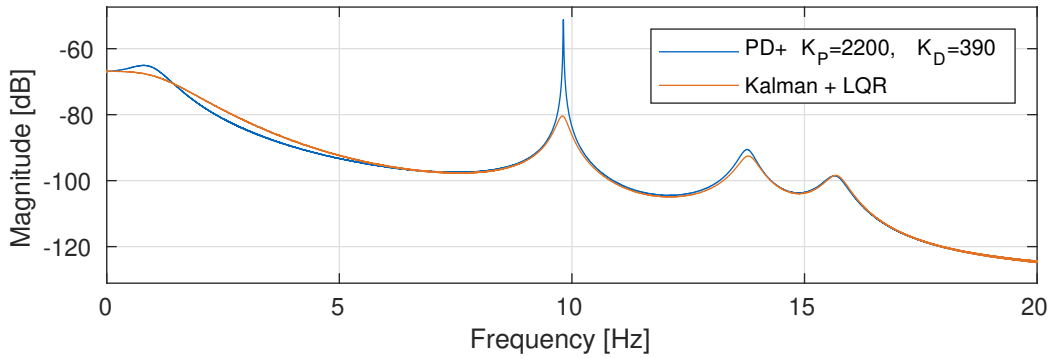

Figure 4.29: Identified disturbance transfer function for the closed-loop system with the Steady-State Kalman Filter combined with the Linear Quadratic Regulator in comparison to the standalone PD+ controller

This improvement in the vibration rejection holds for varying system dynamics which can be seen in fig. 4.30. For the control scheme using the Kalman Filter and the Linear Quadratic Regulator the maximal peak corresponding to the first resonance of the structure is lower than the lowest peak of the PD+ controlled system. Overall the closed-loop is robustified against these parameter changes as one can see that the variance of the peaks for the first resonances is reduced. The peaks corresponding to the second resonance of the structure is slightly reduced without effecting the range of the peaks. For the third resonance no difference can be seen. Overall the vibration rejection is improved by using a combination of a Kalman Filter and a Linear Quadratic Regulator. The vibrations caused by the first and most dominant resonance frequency is reduced.

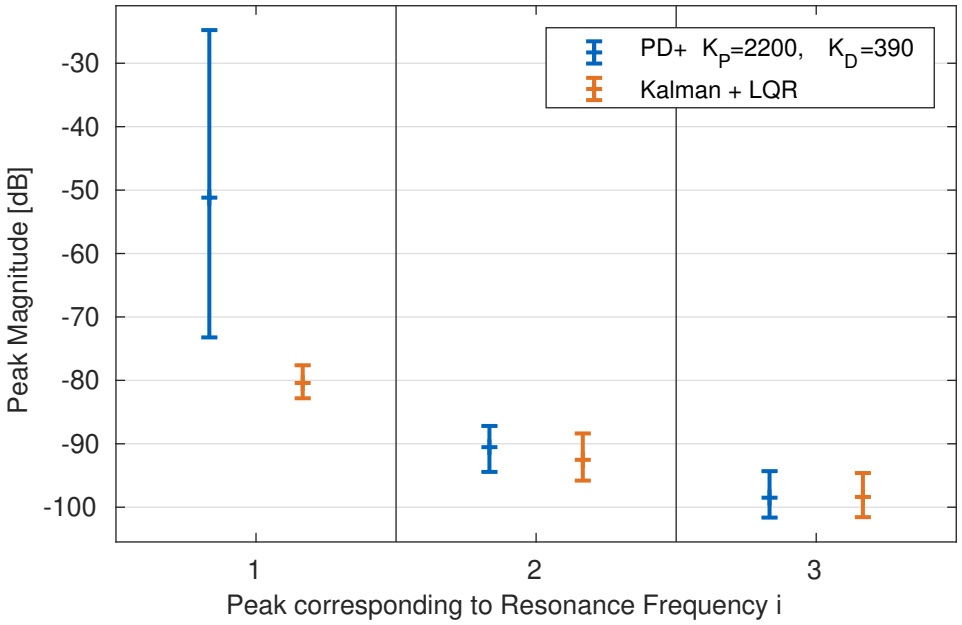

Figure 4.30: Peaks of the disturbance transfer function corresponding to the resonances of the structure for perturbed system dynamics in comparison between the PD+ controlled system and the control scheme with Kalman Filter and Linear Quadratic Regulator

Another advantage of the LQR is that the design does also contain optimization considering the control input u. One can develop a control scheme that bases on the same Kalman Filter but uses a PD+ controller instead of the LQR similar to the scheme with the second order observer. This control scheme is also tuned to fit the performance criteria which results in the gains displayed in table 4.6. Figure 4.31 displays the control input u of both control schemes with the Kalman Filter during the impulse response. It can be seen that less control input is used when using the LQR instead of using the PD+ controller.

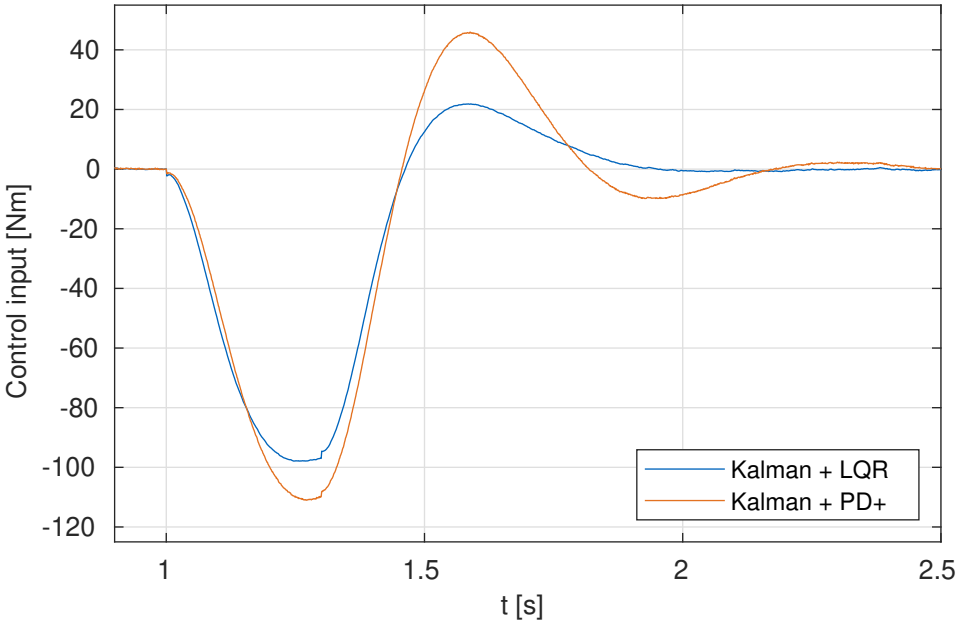

Figure 4.31: Control input needed for the impulse response compared between the control scheme with Kalman Filter and LQR or with PD+ controller

Table 4.6: Parameters of the PD+ controller that is used in combination with the Kalman Filter

Parameter	Value
K_P	3900
K_D	580

4.4 Comparison of the Control Schemes

In this section the different control approaches are compared in order to formulate a recommendation on which controller should be implemented in LOLA. Aside from bare performance, factors like complexity in design and in modeling are considered. The control schemes compared in this section are:

1. PD+ controller with notch filters and direct acceleration feedback (PD+ + Notch + DAF)
2. Reduced Order Observer with PD+ controller (ROO + PD+)
3. Steady-State Kalman Filter with Linear Quadratic Regulator (Kalman + LQR)

The performance measures of these controllers are summarized in table 4.7.

Table 4.7: Summarized performance measures for the three most promising control approaches with the parameterizations from tables 4.3 to 4.5

Performance Measure	PD+ + Notch + DAF	ROO + PD+	Kalman + LQR
$T_{5\,\%}$	0.877 18 s	0.685 73 s	0.4574 s
Δh	18.398 %	16.489 %	3.526 %
ω_c	1.5736 Hz	1.8673 Hz	1.3676 Hz
$\varphi_{i,min}$	1.2807°	1.4733°	1.3736°
$\varphi_{i,max}$	−0.260 13°	−0.276 22°	−0.045 502°
$\lvert G_d(j\omega_{r,1})\rvert$	−86.51 dB	−80.20 dB	−80.41 dB
$\lvert G_d(j\omega_{r,2})\rvert$	−88.61 dB	−91.83 dB	−92.53 dB
$\lvert G_d(j\omega_{r,3})\rvert$	−90.76 dB	−98.12 dB	−98.38 dB
$\lvert G_d(j\omega_{r,1})\rvert_{max}$	−85.31 dB	−76.17 dB	−77.62 dB
$\lvert G_d(j\omega_{r,2})\rvert_{max}$	−83.87 dB	−87.86 dB	−88.37 dB
$\lvert G_d(j\omega_{r,3})\rvert_{max}$	−82.97 dB	−94.14 dB	−94.61 dB

Looking at the performance measures for the reference tracking one can see that the Kalman Filter scheme performed best in terms of settling time $T_{5\,\%}$ and overshoot Δh. This results from the high gains in the Linear Quadratic Regulator and from the prefilter scheme used in this control setup. The control scheme using the Reduced Order Observer performs better than the notch filter setup in this category.

In terms of the bandwidth ω_c the scheme with the Reduced Order Observer achieves the highest bandwidth followed by the setup using the notch filter and the Kalman Filter scheme. This is also illustrated in fig. 4.32 where the reference transfer function is displayed for the three concepts. Due to the high damping of the mechanical poles of the inverted pendulum using the Kalman Filter setup the transfer function is flat for low frequencies and subsequently, drops below −3 dB faster than the other schemes with less damping of the mechanical poles.

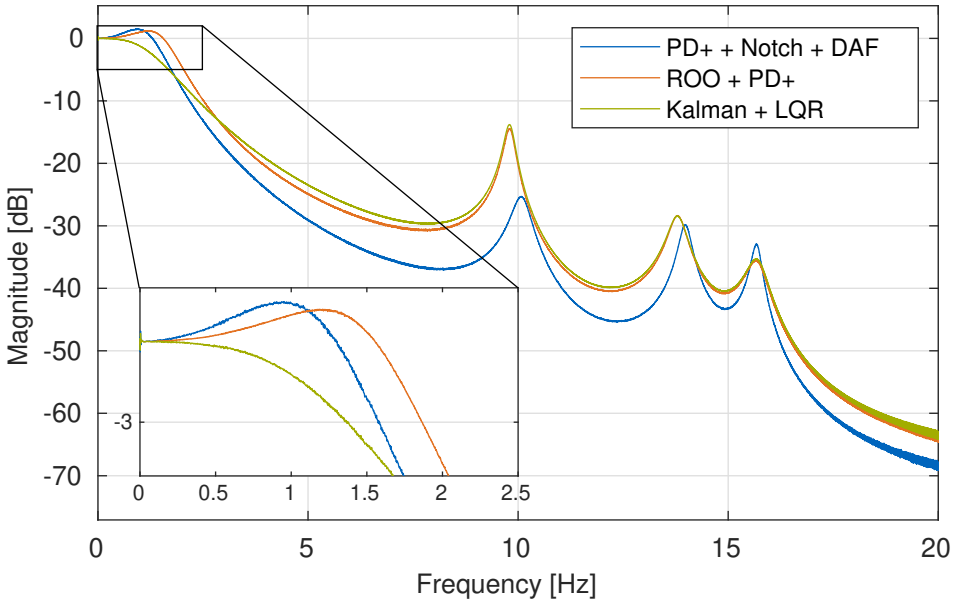

Figure 4.32: Magnitude of the identified reference transfer function $G_r(s)$ with enlarged area to illustrate the bandwidth

The impulse responses are illustrated in fig. 4.33. In terms of disturbance rejection the control scheme using notch filters has the lowest maximal deflection $\varphi_{i,max}$ in the measured angle after a disturbance impulse. The control scheme with the Kalman Filter has a higher maximal deflection but has a lower overshoot $\varphi_{i,min}$ when returning to the upright position. The control setup using the Reduced Order Observer perform worst in terms of disturbance impulse rejection.

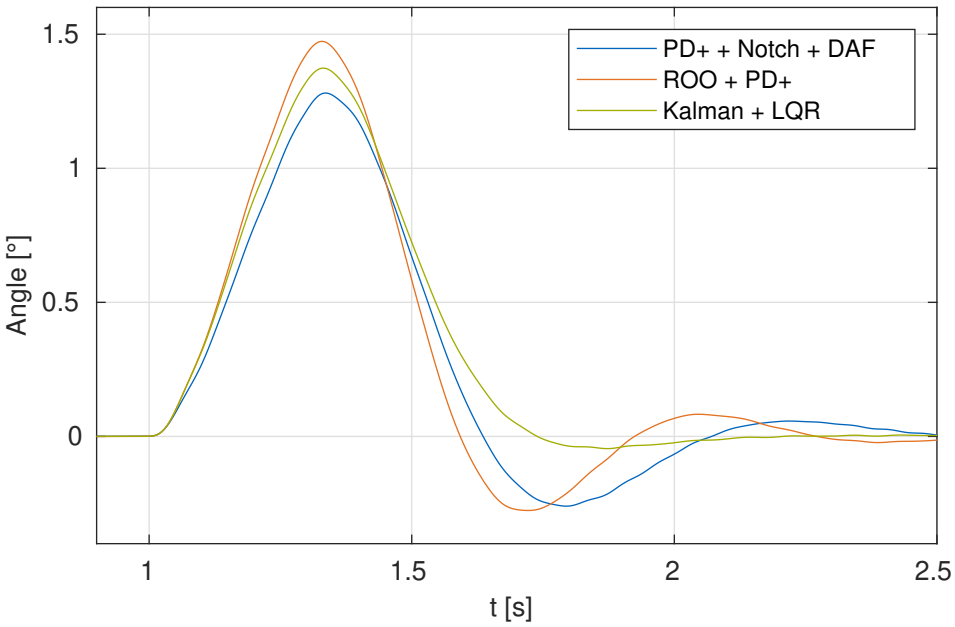

Figure 4.33: Response to a disturbance impulse

In fig. 4.34 the peaks corresponding to the resonances of the structure are displayed for the three controllers. Considering the vibration rejection the two model based control schemes perform relatively similar with a slightly better robustness to parameter changes for the Kalman Filter setup where the variance of the peak magnitude of the first resonance is lower. The controller using notch filters outperforms the observer based control setups in terms of the first resonance frequency as the magnitude is lower

for the nominal system and for all perturbed systems. The magnitude of the peaks of the higher resonances is increased in comparison to the observer based schemes and also these resonances are more sensitive to parameter changes. Overall the peaks of the controller using notch filters are more balanced and lower for the tested parameters and parameter variations and thus, the controller with notch filter and direct acceleration feedback is considered to have the better vibration rejection behavior.

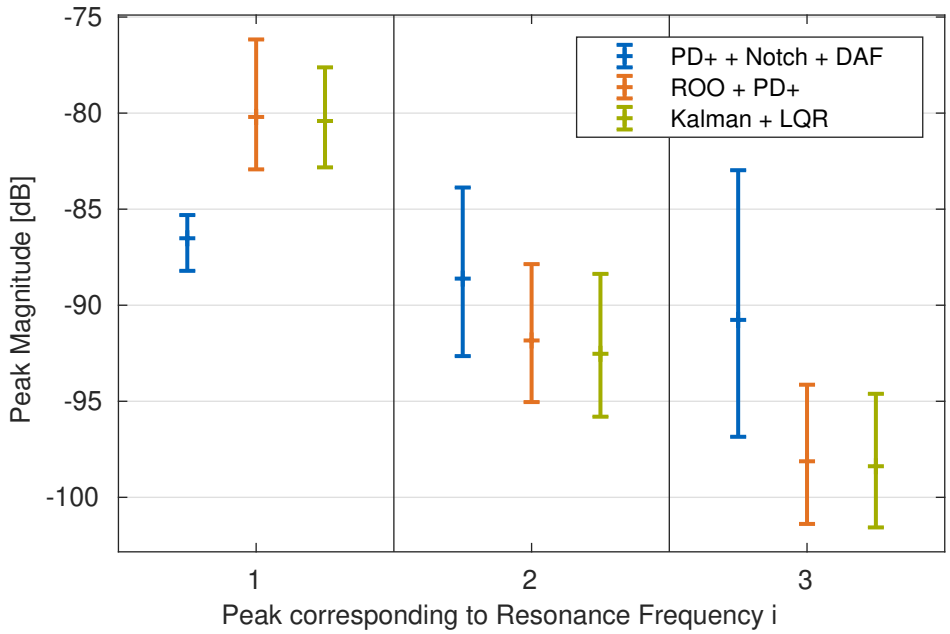

Figure 4.34: Magnitude of the peaks corresponding to the structural resonances in the disturbance transfer function $G_{\mathrm{d}}(s)$ for varying system dynamics

After discussing the performance of the controller based on the performance measures resulting from the simulation, the effort to design the controllers is now rated. It should be said that this can be considered subjective and is not based on comparable numbers.

The modeling effort determines how much information about the system is necessary to design the controller. The notch filters require the least model knowledge as only the frequencies of the resonances have to be known and those can be obtained relatively easy from experiments. For the Reduced Order Observer a model of the inverted pendulum has to be known together with the damping ratio and the frequency of the first resonance. The damping is difficult to obtain and often has to be estimated. The highest system knowledge is needed for the Kalman Filter as here all resonance frequencies and damping ratios as well as the actor model has to be known. Also the sensor noise has to be determined. Obtaining sufficiently precise values for all these parameters can be hard and might make this approach infeasible in a real-world application.

In terms of design complexity, which determines how hard it is to design the controller for a determined model, the Reduced Order Observer control setup is the simplest of the three controllers. It is only necessary to define the gains of the PD+ controller and the distance between the regulator and observer poles. The validity of the chosen distance can be evaluated well with the observation error and thus, the concept is less complex to design than the other two. For each notch filter the depth of the notch g_{min} and the damping coefficient D_{Notch} have to be determined. Subsequently 6 parameters of the notch filters and additionally the gains of the PD+ controller and of the acceleration feedback have to be tuned. Those parameters are coupled and effect the same performance measures which can make the design process more complex. For the Kalman Filter and Linear Quadratic Regulator weight matrices $\boldsymbol{Q}$ and $\tilde{\boldsymbol{Q}}$ have to be found. Assuming diagonal weight matrices there are 12 parameters that have to be

set in order to determine the controller which is more complex than the design of the other concepts.

Overall the control concept using a Reduced Order Observer and the PD+ controller requires good model knowledge and a model for the first resonance frequency. Based on this the controller can be designed relatively easy and the resulting controller can achieve a high bandwidth and solid overall performance.

With a full model of the structural dynamics, the underlying inverted pendulum dynamics, the sensor dynamics and the actor dynamics a Kalman Filter can be used in combination with a Linear Quadratic Regulator. To tune the process noise matrix $\boldsymbol{Q}$ and the weight matrix $\tilde{\boldsymbol{Q}}$ for the regulator can be tedious and many coupled parameters have to be tuned. To include reference tracking a feedforward controller has to be designed which does not require further parameter tuning. The resulting controller has the best reference tracking and good vibration damping even for perturbed system dynamics.

The controller built of notch filters tuned to the resonance frequencies and a PD+ controller with direct acceleration feedback requires the least amount of model knowledge although the design process involves 9 parameters with coupled effects. The resulting controller has the best vibration damping behavior and thus, is considered a good compromise between effort and performance and the best fit for the problem.

Chapter 5

Validation using Multi-Body Simulation

In the preceding chapter the control schemes are tested on the inverted pendulum model with structural dynamics, which is a highly abstracted model of the real control problem of the humanoid robot LOLA. To validate the control schemes in LOLA's application a Multi-Body Simulation (MBS) of the robot is used. This simulation is described in detail in [5]. Along with the rigid multi-body dynamics including nonlinear drive mechanisms, nonlinear gear elasticity and nonlinear friction the dynamics of the electrical motors are modeled. The contact with the ground is modeled using spring-damper systems. This results in a set of Ordinary Differential Equations (ODEs) with a total of 164 DoF [31]. Sensor models are included that cover limited sensor bandwidth, noise, quantization and bias. The MBS is written in highly-efficient C++ code and contains the complete control system of LOLA.

As all bodies are assumed to be rigid, in the simulation no eigenfrequencies from the structural dynamics can be seen. Therefore, the structural dynamics model introduced in section 3.2 are included in the sensor model of the simulation. This is necessary to evaluate the performance of the control systems in the MBS in context of vibration damping. But this does also limit the informative value of this validation as the MATLAB SIMULINK simulation and the MBS both include the same structural dynamics model which may vary significantly from the actual structural dynamics. Therefore, the results of this validation have to be evaluated with care and the transfer of the results to the reality has to be questioned. Still the validation gives some information about whether the balance controller works in the setting with the other control modules or interferes with them.

Two scenarios are used in the MBS. In the first scenario the robot is standing and a disturbance impulse via a torque is applied to test the balance controller. In the second scenario the robot is standing the seconds before starting to walk forwards.

Figure 5.1 displays the IMU signals from the MBS using the control scheme with the Kalman Filter and the Linear Quadratic Regulator in the scenario with a disturbance torque at 2 s. In the output angle φ_m it can be seen that already prior to the disturbance the angle oscillates for the Kalman Filter control setup. This oscillation is stable and has no increasing amplitude. After the disturbance this oscillation is magnified and has a increasing amplitude, destabilizing the robot. In the angular velocity $\dot{\varphi}_m$ a minor improvement in the oscillation damping can be seen compared to the PD+ controller prior to the impulse. In the measured acceleration a_m it can be seen that prior to the disturbance the oscillations are damped in comparison to the bare PD+ controller.

In contrast to the disturbance impulse scenario, for the walking motion the control setup using the Kalman Filter is stable. The signals of the IMU resulting from this simulation can be seen in fig. 5.2. It can be seen that the oscillations in the angular velocity $\dot{\varphi}_m$ and in the a_m are reduced in comparison to the PD+ controller. In the output angle φ_m it can be seen that the upper body movement due to the walking motion has an increased amplitude for the Kalman Filter control scheme. This can be quantified

using the Root Mean Squared Error (RMSE) between the measured signals and the desired reference trajectories which are assumed to be equal to zero. These errors are displayed in table 5.1. The errors in the angular velocity and acceleration is decreased while the error in the angle is increased by using the Kalman Filter control setup instead of the PD+ controller.

Table 5.1: Root Mean Squared Error (RMSE) of the measured IMU signals during walking motion in comparison between the standalone PD+ controller and the Kalman + LQR control setup

RMSE	PD+	Kalman + LQR
φ_m	0.2060°	0.3132°
$\dot{\varphi}_m$	$5.0440\,^\circ\,s^{-1}$	$4.2428\,^\circ\,s^{-1}$
a_m	$1.4691\,m\,s^{-2}$	$1.2554\,m\,s^{-2}$

It can be concluded that the Kalman Filter control setup is not stable for disturbance impulses which makes this control setup inapplicable in the application on the real robot. During walking motion the vibrations in angular velocity and acceleration are reduced at cost of larger movements of the upper body. Overall the performance of the control setup is decreased compared to the MATLAB SIMULINK simulation.

The control system using notch filters with the PD+ controller with acceleration feedback is also implemented in C++ to be validated in the MBS. The IMU output in the scenario of the disturbance impulse can be seen in fig. 5.3. In the output angle φ_m the control setup using notch filters has an increased settling time but similar maximal deflections in comparison to the PD+ controller. The use of the notch filter dampens the vibrations in the angular velocity $\dot{\varphi}_m$ slightly. The oscillations in the acceleration a_m are significantly reduced. The RMSE for these signals in comparison to the PD+ controller is displayed in table 5.2. The error in the angle is increased by 2.6 % while the errors in angular velocity and acceleration are reduced by 9.6 % and 35.5 % respectively.

Table 5.2: Root Mean Squared Error (RMSE) of the measured IMU signals during the impulse scenario in comparison between the standalone PD+ controller and the notch filter control setup

RMSE	PD+	Kalman + LQR
φ_m	0.1730°	0.1775°
$\dot{\varphi}_m$	$2.3495\,^\circ\,s^{-1}$	$2.1240\,^\circ\,s^{-1}$
a_m	$0.6108\,m\,s^{-2}$	$0.3934\,m\,s^{-2}$

The resulting IMU signals for the MBS using the notch filter control setup in the walking scenario can be seen in fig. 5.4. The corresponding RMSE can be seen in table 5.3. The vibrations in angular velocity $\dot{\varphi}_m$ and acceleration a_m are visibly damped and for both signals the RMSE is reduced by about 18 %. In the output angle φ_m it can be seen that the range of motion of the upper body is increased which also reflects the increased RMSE in the output angle φ_m.Overall the vibration damping is improved using the notch filters. No issues with the stability of the balance controller occur. It can be said that the control setup using notch filters and direct acceleration feedback improves the performance of the balance controller in the MBS.

Table 5.3: Root Mean Squared Error (RMSE) of the measured IMU signals during walking motion in comparison between the standalone PD+ controller and the notch filter control setup

RMSE	PD+	Kalman + LQR
φ_m	0.2060°	0.2894°
$\dot{\varphi}_m$	$5.0440\,^\circ\,s^{-1}$	$4.1652\,^\circ\,s^{-1}$
a_m	$1.4691\,m\,s^{-2}$	$1.1908\,m\,s^{-2}$

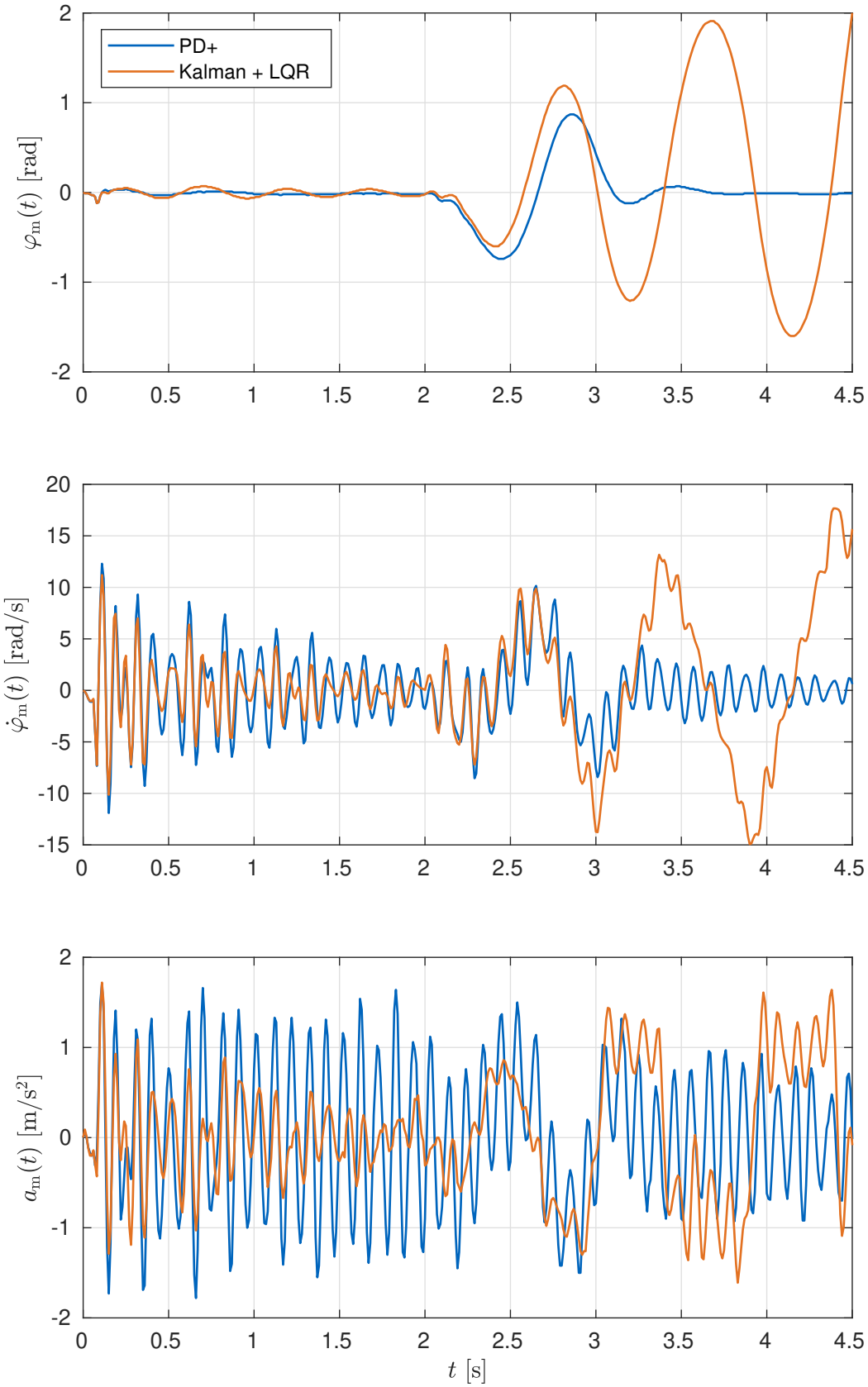

Figure 5.1: Sensor signals of the IMU for MBS with the balance controller consisting of a Kalman Filter and a Linear Quadratic Regulator during a disturbance impulse

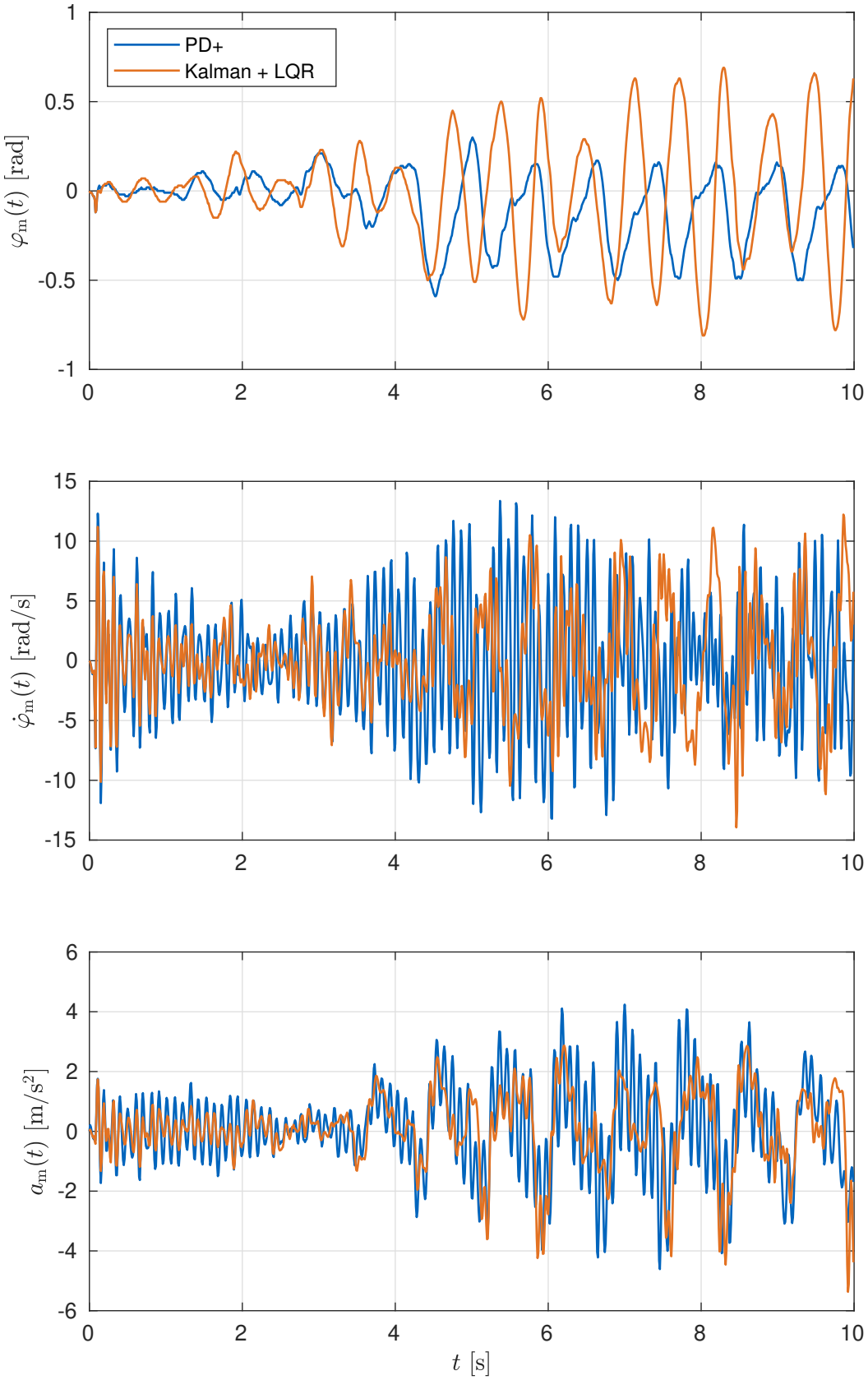

Figure 5.2: Sensor signals of the IMU for MBS with the balance controller consisting of a Kalman Filter and a Linear Quadratic Regulator during a walking motion

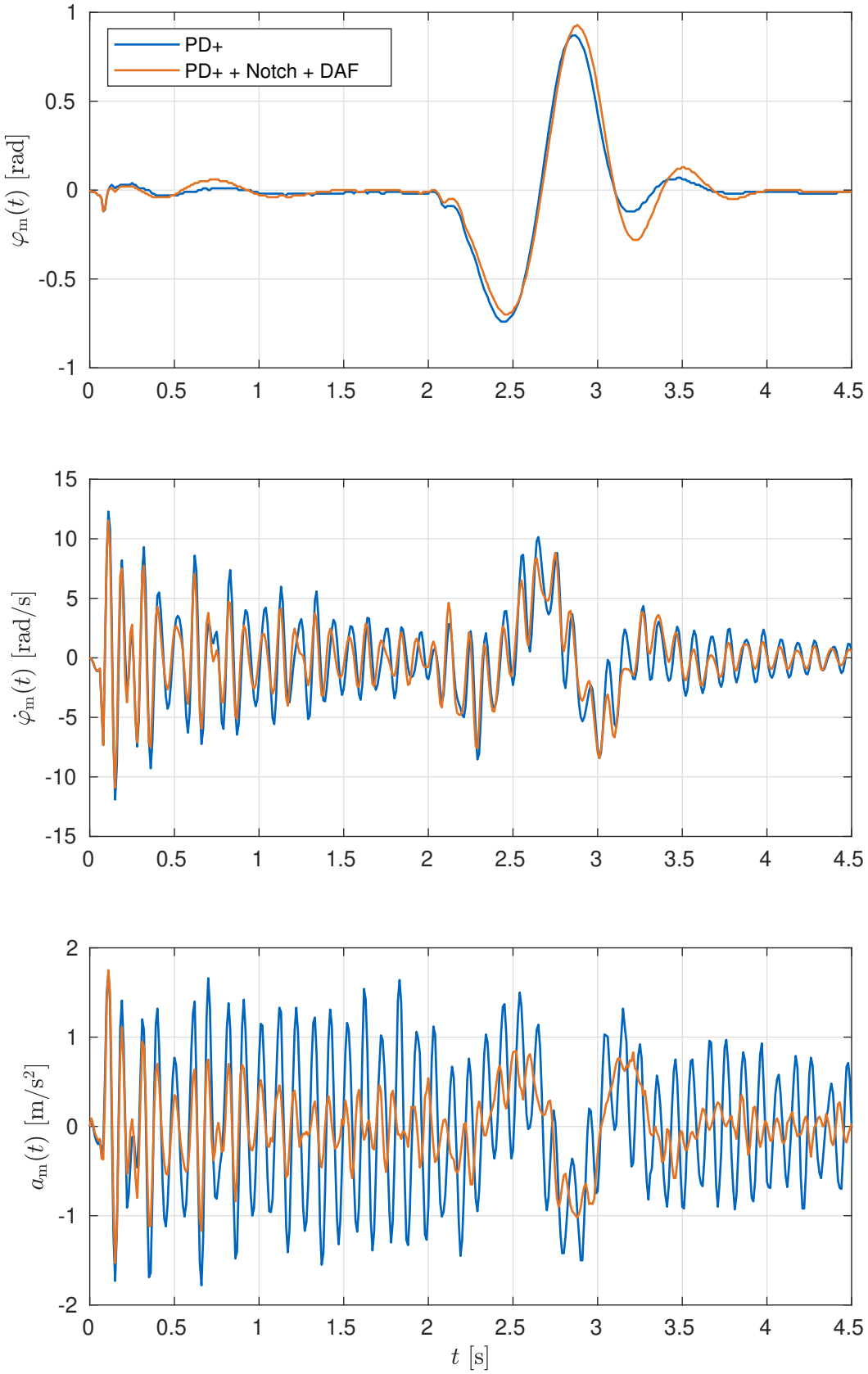

Figure 5.3: Sensor signals of the IMU for MBS with the balance controller consisting of notch filters with a PD+ controller and direct acceleration feedback during a disturbance impulse

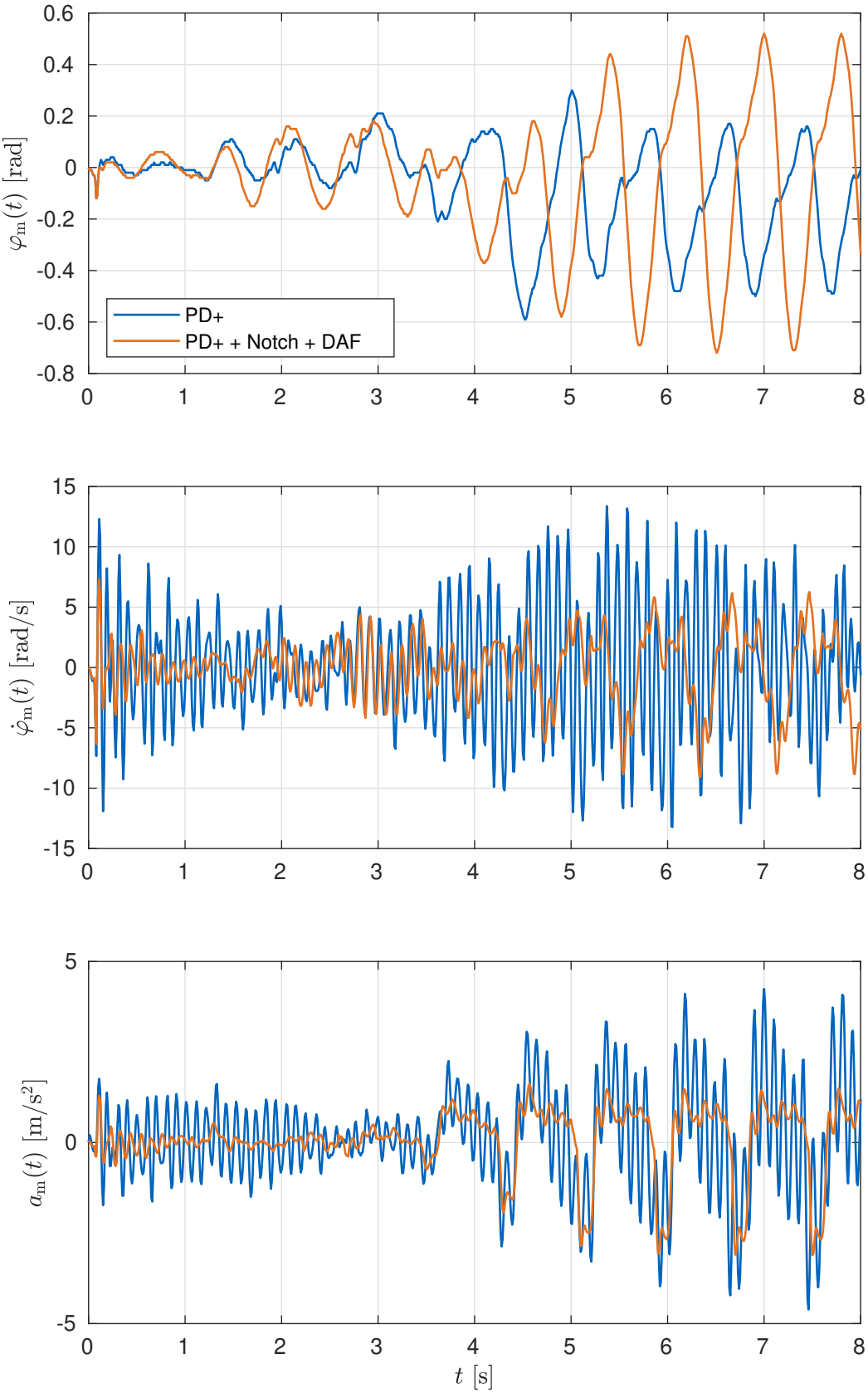

Figure 5.4: Sensor signals of the IMU for MBS with the balance controller consisting of notch filters with a PD+ controller and direct acceleration feedback during a walking motion

Chapter 6

Conclusion

In this research project the balance controller of the biped robot LOLA is analyzed in detail. The underlying model, the inverted pendulum, is extended by a structural dynamics model. This model is based on a transfer function containing three pairs of resonance and anti-resonance frequencies. Around this extended model a simulation is build that includes a sensor model with quantization and noise and an actuator model. In the framework of this simulation different control approaches from the field of active vibration damping and model-based control are designed and tested with the goal to find a controller that can control the flexible inverted pendulum with high performance and high vibration damping while also being robust to system perturbations.

Model-based control schemes consisting of observers and state feedback are designed and work effectively in the MATLAB SIMULINK simulation where only the flexible inverted pendulum is modeled. The control setup using a Kalman Filter in combination with a Linear Quadratic Regulator leads to significantly improved step and impulse responses compared to the previously used PD+ controller while reducing the resulting vibrations simultaneously. In the MBS this control setup leads to a walking motion with significantly reduced vibrations in the angular velocity and the acceleration. The control scheme cannot stabilize the robot for a disturbance torque in the MBS. Therefore, and due to the significant modeling effort the practicability of the control scheme using a Kalman Filter with a Linear Quadratic Regulator is questionable.

The most promising control setup from the field of active vibration damping includes notch filters which filter the parts of the measured signals that contain the vibrations resulting from the structural resonances. Using these signals a PD+ controller computes the control input which is less effected by the vibrations of the structure than a PD+ controller without notch filters. The idea is that using the notch filters the vibrations due to the structural dynamics are not fed back into the system. Additional direct acceleration feedback can improve the damping of the resonances. The notch filters do just require the frequencies of the structural resonance as a priori knowledge which makes them relatively easy to apply. In the MATLAB SIMULINK simulation, this control setup reduces the structural vibrations significantly and allows for a more aggressive closed-loop system. The vibration damping behavior is significantly improved and robust against system perturbations. Using the MBS it is verified that this control setup reduces high-frequency vibrations even in combination with the other control modules of LOLA.

The validation of the control schemes is based on the MBS which is extended with the structural dynamics model derived in this thesis. Therefore, the informative value of this validation may be corrupted as the structural dynamics model is limited to three resonances and the damping coefficient are only estimated. subsequently, experiments on the real robot have to be conducted in order to prove the effectiveness of the proposed balance controllers. This was not possible within the research for this thesis as the Chair of Applied Mechanics was closed due to the current COVID-19 pandemic which leaves area for future research.

Currently the desired torque to stabilize the upper body of the robot is realized by both the feet and the arms of the robot together. The majority of the torque is generated by the feet. As the IMU and the arms of the robot are located in the upper body they represent a collocated sensor/actor pair considering the structural dynamics of the spine. Therefore, it could be beneficial to use the arms of the robot for vibration damping and generate the torque to control the upper body angle by the feet. In future research it could be analyzed how much torque can be generated by the arms and how this torque can be used to dampen the upper body vibration. This states a collocated vibration damping problem which has multiple benefits regarding the stability of active vibration control approaches.

In this thesis the control schemes are designed and tuned to the nominal system dynamics. The robustness against modeling errors is evaluated by applying the control schemes to systems that are perturbed versions of the nominal system e.g. with shifted resonance frequencies. This is done to verify that the control schemes can handle the changing system dynamics that result from different configurations of LOLA. For example the dynamics change if LOLA's arms are raised in comparison to hanging arms. Instead of choosing a control setup that is insensitive to changing resonance frequencies, it is also possible to obtain a better approximation of the resonance frequencies in runtime. In future research the model of the structural dynamics can be refined in order to approximate the estimate of the resonance frequencies based on the current configuration of the robot. Another approach is to estimate the resonance frequencies online via system identification using e.g. the recurrent least-squares approach as done in [25][12]. Doing so the controllers can be tuned to the current resonance frequencies during runtime. This can improve the performance of all control schemes. Subsequently, the resonant controller, which should work better with refined estimates of the resonance frequencies, should be considered due to the good tunability and stability properties.

Appendix A

Reduced Order Observer

The following equations describe a discretised Reduced Order Observer from eqs. (4.43) and (4.44) with the parameters used for the simulation:

$$\boldsymbol{A}_{\text{ROO,d}} = \begin{bmatrix} 0.9413 & 0.0009704 \\ -0.8719 & 0.9996 \end{bmatrix} \tag{A.1}$$

$$\boldsymbol{B}_{\text{ROO,d}} = \begin{bmatrix} 8.172\text{e}-9 & 0.05869 & -0.000672 \\ 1.667\text{e}-5 & 0.8808 & -0.01353 \end{bmatrix} \tag{A.2}$$

$$\boldsymbol{C}_{\text{ROO,d}} = \begin{bmatrix} 1 & 0 \\ 0 & 1 \end{bmatrix} \tag{A.3}$$

$$\boldsymbol{D}_{\text{ROO,d}} = \begin{bmatrix} 0 & 0 & 0.01583 \\ 0 & 0 & 0.2393 \end{bmatrix} \tag{A.4}$$

Appendix B

Kalman Filter and Linear Quadratic Regulator

$$\boldsymbol{K}_{\infty} = \begin{bmatrix} -7.266\text{e}-13 & -1.863\text{e}-14 & 4.338\text{e}-16 \\ 1.005 & -0.001705 & 0.0001724 \\ -5.526 & -0.1622 & 0.003741 \\ 0.0001723 & 3.851\text{e}-6 & -9.417e-8 \\ -0.001345 & -4.144\text{e}-5 & 9.399\text{e}-7 \\ 0.0001363 & 1.836\text{e}-6 & -5.382\text{e}-8 \\ 0.009126 & 0.0002813 & -6.378\text{e}-6 \\ 0.0001243 & -3.286\text{e}-6 & 2.732\text{e}-8 \\ -0.001781 & -5.492\text{e}-5 & 1.245\text{e}-6 \end{bmatrix} \tag{B.1}$$

$$\boldsymbol{g} = \begin{bmatrix} 0.4726 & 5575.0 & 1001.0 & 7.162\text{e}+5 & -13680.0 & 3.348\text{e}+5 & -520.7 & 1.123\text{e}+5 & 1423.0 \end{bmatrix} \tag{B.2}$$

$$\boldsymbol{M}_x = \begin{bmatrix} -537.6 & 9.997 & -0.01716 \\ 1.0 & -0.0186 & 3.192\text{e}-5 \\ 1.557\text{e}-13 & 8.918\text{e}-7 & 4.702\text{e}-9 \\ 0.0002637 & -5.198\text{e}-6 & 7.098\text{e}-9 \\ -1.057\text{e}-13 & 0.0006809 & 3.042\text{e}-6 \\ 0.000133 & -9.757\text{e}-7 & 1.104\text{e}-8 \\ 7.696\text{e}-14 & 0.000816 & 3.364\text{e}-6 \\ 0.0001027 & 6.459\text{e}-7 & 1.539\text{e}-8 \\ -4.89\text{e}-15 & -0.0001719 & -4.076\text{e}-6 \end{bmatrix} \tag{B.3}$$

$$\boldsymbol{M}_u = \begin{bmatrix} -537.6 & 9.997 & -0.01716 \end{bmatrix} \tag{B.4}$$

Appendix C

Summarized Simulation Results

Table C.1: Results of the control schemes with the MATLAB SIMULINK Simulation of the inverted pendulum

Performance Measure	PD+ table 3.2	PD+ section 4.1	PD+ with DAF table 4.1	PD+ + resonant table 4.2	PD+ + Notch table 4.3	PD+ + Notch + DAF table 4.3	ROO + PD+ table 4.4	Kalman + PD+ table 4.6	Kalman + LQR table 4.5
$T_{5\%}$	1.5712 s	1.0629 s	1.1259 s	0.960 87 s	0.713 94 s	0.877 18 s	0.685 73 s	0.724 67 s	0.4574 s
Δh	24.624 %	19.022 %	21.322 %	18.013 %	15.414 %	18.398 %	16.489 %	18.623 %	3.526 %
ω_c	1.0376 Hz	1.3466 Hz	1.3733 Hz	1.3847 Hz	1.7872 Hz	1.5736 Hz	1.8673 Hz	1.9264 Hz	1.3676 Hz
$\varphi_{i,min}$	2.1878°	1.4809°	1.3954°	1.5023°	1.4874°	1.2807°	1.4733°	1.4261°	1.3736°
$\varphi_{i,max}$	−0.546 16°	−0.293 92°	−0.309 35°	−0.29°	−0.283 16°	−0.260 13°	−0.276 22°	−0.262 96°	−0.045 502°
$\lvert G_d(j\omega_{r,1})\rvert$	−71.31 dB	−51.19 dB	−67.45 dB	−79.14 dB	−80.31 dB	−86.51 dB	−80.20 dB	−80.27 dB	−80.41 dB
$\lvert G_d(j\omega_{r,2})\rvert$	−91.26 dB	−90.53 dB	−89.01 dB	−92.11 dB	−92.56 dB	−88.61 dB	−91.83 dB	−92.53 dB	−92.53 dB
$\lvert G_d(j\omega_{r,3})\rvert$	−98.47 dB	−98.50 dB	−97.15 dB	−98.11 dB	−98.41 dB	−90.76 dB	−98.12 dB	−98.39 dB	−98.38 dB
$\lvert G_d(j\omega_{r,1})\rvert_{max}$	−51.89 dB	−24.77 dB	−27.39 dB	−24.74 dB	−78.36 dB	−85.31 dB	−76.17 dB	−77.91 dB	−77.62 dB
$\lvert G_d(j\omega_{r,2})\rvert_{max}$	−86.48 dB	−87.19 dB	−84.33 dB	−87.98 dB	−88.79 dB	−83.87 dB	−87.86 dB	−88.48 dB	−88.37 dB
$\lvert G_d(j\omega_{r,3})\rvert_{max}$	−94.52 dB	−94.31 dB	−93.41 dB	−94.27 dB	−94.56 dB	−82.97 dB	−94.14 dB	−94.59 dB	−94.61 dB

Bibliography

[1] Abdullahi, A. M., Mohamed, Z., and M., M. N. “Resonant Control of a Single-Link Flexible Manipulator”. In: *Jurnal Teknologi* 67.5 (Mar. 2014). DOI: 10.11113/jt.v67.2840.

[2] Balas, M. “Feedback control of flexible systems”. In: *IEEE Transactions on Automatic Control* 23.4 (Aug. 1978), pp. 673–679. DOI: 10.1109/tac.1978.1101798.

[3] Balas, M. J. “Active control of flexible systems”. In: *Journal of Optimization Theory and Applications* 25.3 (July 1978), pp. 415–436. DOI: 10.1007/bf00932903.

[4] Baz, A. and Hong, J.-T. “Adaptive Control of Flexible Structures Using Modal Positive Position Feedback”. In: *International Journal of Adaptive Control and Signal Processing* 11.3 (May 1997), pp. 231–253. DOI: 10.1002/(sici)1099-1115(199705)11:3<231::aid-acs435>3.0.co;2-8.

[5] Buschmann, T. *Simulation and control of biped walking robots*. München: Verl. Dr. Hut, 2011. ISBN: 9783868538045.

[6] Buschmann, T., Lohmeier, S., and Ulbrich, H. “Biped walking control based on hybrid position/force control”. In: *2009 IEEE/RSJ International Conference on Intelligent Robots and Systems*. IEEE, Oct. 2009. DOI: 10.1109/iros.2009.5354643.

[7] Chalhoub, N. G. and Ulsoy, A. G. “Control of a flexible robot arm: experimental and theoretical results”. In: *Journal of Dynamic Systems, Measurement, and Control* 109.4 (Dec. 1987), pp. 299–309. DOI: 10.1115/1.3143859.

[8] Englsberger, J., Werner, A., Ott, C., Henze, B., Roa, M. A., Garofalo, G., Burger, R., Beyer, A., Eiberger, O., Schmid, K., and Albu-Schaffer, A. “Overview of the torque-controlled humanoid robot TORO”. In: *2014 IEEE-RAS International Conference on Humanoid Robots*. IEEE, Nov. 2014. DOI: 10.1109/humanoids.2014.7041473.

[9] Fanson, J. L. and Caughey, T. K. “Positive position feedback control for large space structures”. In: *AIAA Journal* 28.4 (Apr. 1990), pp. 717–724. DOI: 10.2514/3.10451.

[10] Friswell, M. I. and Inman, D. J. “The relationship between positive position feedback and output feedback controllers”. In: *Smart Materials and Structures* 8.3 (Jan. 1999), pp. 285–291. DOI: 10.1088/0964-1726/8/3/301.

[11] Goh, C. J. and Caughey, T. K. “On the stability problem caused by finite actuator dynamics in the collocated control of large space structures”. In: *International Journal of Control* 41.3 (Mar. 1985), pp. 787–802. DOI: 10.1080/0020718508961163.

[12] Harder, M. “Simulation von Externen Ansätzen zur Aktiven Schwingungsdämpfung von Flexiblen Robotermanipulatoren”. MA thesis. TUM - Lehrstuhl für Angewandte Mechank, 2019.

[13] Hildebrandt, A.-C., Wittmann, R., Sygulla, F., Wahrmann, D., Rixen, D., and Buschmann, T. “Versatile and robust bipedal walking in unknown environments: real-time collision avoidance and disturbance rejection”. In: *Autonomous Robots* 43.8 (Feb. 2019), pp. 1957–1976. DOI: 10.1007/s10514-019-09838-3.

[14] Hsu, W., Lai, C., and Hsu, P. “A novel design for vibration suppression for lightly-damped servo control systems”. In: *2011 8th Asian Control Conference (ASCC)*. 2011, pp. 251–256.

[15] Huang, G. P., Mourikis, A. I., and Roumeliotis, S. I. “Analysis and improvement of the consistency of extended Kalman filter based SLAM”. In: *2008 IEEE International Conference on Robotics and Automation*. IEEE, May 2008. DOI: 10.1109/robot.2008.4543252.

[16] Inman, D. J. *Vibration with control*. Hoboken, NJ: Wiley, 2006. ISBN: 0470010517.

[17] Ji, J.-K. and Sul, S.-K. “Kalman filter and LQ based speed controller for torsional vibration suppression in a 2-mass motor drive system”. In: *IEEE Transactions on Industrial Electronics* 42.6 (1995), pp. 564–571. DOI: 10.1109/41.475496.

[18] KAUTSKY, J., NICHOLS, N. K., and DOOREN, P. V. “Robust pole assignment in linear state feedback”. In: *International Journal of Control* 41.5 (May 1985), pp. 1129–1155. DOI: 10.1080/0020718508961188.

[19] Lewis, F. *Optimal and robust estimation : with an introduction to stochastic control theory*. Boca Raton: CRC Press, 2008. ISBN: 9781420008296.

[20] Lohmeier, S. *Design and realization of a humanoid robot for fast and autonomous bipedal locomotion*. München: Verl. Dr. Hut, 2010. ISBN: 9783868537345.

[21] Lunze, J. *Regelungstechnik 1 : Systemtheoretische Grundlagen, Analyse und Entwurf einschleifiger Regelungen*. Berlin, Heidelberg: Springer Berlin HeidelbergImprint Springer Vieweg, 2016. ISBN: 9783662526774.

[22] Lunze, J. *Regelungstechnik 2*. Springer Berlin Heidelberg, 2016. DOI: 10.1007/978-3-662-52676-7.

[23] Mao, Q. and Pietrzko, S. *Control of Noise and Structural Vibration*. Springer London, 2013. DOI: 10.1007/978-1-4471-5091-6.

[24] Odelson, B. J., Rajamani, M. R., and Rawlings, J. B. “A new autocovariance least-squares method for estimating noise covariances”. In: *Automatica* 42.2 (Feb. 2006), pp. 303–308. DOI: 10.1016/j.automatica.2005.09.006.

[25] Orszulik, R. R. and Shan, J. “Vibration Control Using Input Shaping and Adaptive Positive Position Feedback”. In: *Journal of Guidance, Control, and Dynamics* 34.4 (July 2011), pp. 1031–1044. DOI: 10.2514/1.52287.

[26] Pota, H. R., Moheimani, S. O. R., and Smith, M. “Resonant controllers for smart structures”. In: *Smart Materials and Structures* 11.1 (Feb. 2002), pp. 1–8. DOI: 10.1088/0964-1726/11/1/301.

[27] Preumont, A. *Vibration Control of Active Structures: An Introduction (Solid Mechanics and Its Applications) (v. 96)*. Springer, 2002. ISBN: 1-4020-0496-6.

[28] Preumont, A. and Loix, N. “Active damping of a stiff beam-like structure with acceleration feedback”. In: *Experimental Mechanics* 34.1 (Mar. 1994), pp. 23–26. DOI: 10.1007/bf02328438.

[29] Qiu, Z. “Acceleration Sensor Based Vibration Control for Flexible Robot by Using PPF Algorithm”. In: *2007 IEEE International Conference on Control and Automation*. IEEE, May 2007. DOI: 10.1109/icca.2007.4376577.

[30] Rajamani, M. R. and Rawlings, J. B. “Estimation of the disturbance structure from data using semidefinite programming and optimal weighting”. In: *Automatica* 45.1 (Jan. 2009), pp. 142–148. DOI: 10.1016/j.automatica.2008.05.032.

[31] Rauth, L. “Inertiale Stabilisierung eines humanoiden Laufroboters”. MA thesis. TUM - Lehrstuhl für Angewandte Mechank, 2019.

[32] Rouillard, V. “Excitation techniques for resonance analysis of packages”. In: *Packaging Technology and Science* 15.5 (Sept. 2002), pp. 267–274. DOI: 10.1002/pts.598.

[33] Schmidt, P. and Rehm, T. “Notch filter tuning for resonant frequency reduction in dual inertia systems”. In: *Conference Record of the 1999 IEEE Industry Applications Conference. Thirty-Forth IAS Annual Meeting (Cat. No.99CH36370)*. IEEE. DOI: 10.1109/ias.1999.805973.

[34] Sim, E. and Lee, S. W. “Active vibration control of flexible structures with acceleration feedback”. In: *Journal of Guidance, Control, and Dynamics* 16.2 (Mar. 1993), pp. 413–415. DOI: 10.2514/3.21025.

[35] Simon, D. S. *Optimal State Estimation*. John Wiley & Sons, June 12, 2006. 554 pp. ISBN: 0471708585.

[36] Song, G., Schmidt, S. P., and Agrawal, B. N. “Experimental Robustness Study of Positive Position Feedback Control for Active Vibration Suppression”. In: *Journal of Guidance, Control, and Dynamics* 25.1 (Jan. 2002), 179a–182. DOI: 10.2514/2.4865.

[37] Sygulla, F. and Rixen, D. “A force-control scheme for biped robots to walk over uneven terrain including partial footholds”. In: *International Journal of Advanced Robotic Systems* 17.1 (Jan. 2020), p. 172988141989747. DOI: 10.1177/1729881419897472.

[38] Sygulla, F., Wittmann, R., Seiwald, P., Berninger, T., Hildebrandt, A.-C., Wahrmann, D., and Rixen, D. “An EtherCAT-Based Real-Time Control System Architecture for Humanoid Robots”. In: *2018 IEEE 14th International Conference on Automation Science and Engineering (CASE)*. IEEE, Aug. 2018. DOI: 10.1109/coase.2018.8560532.

[39] Urbann, O., Schwarz, I., and Hofmann, M. “Flexible Linear Inverted Pendulum Model for cost-effective biped robots”. In: *2015 IEEE-RAS 15th International Conference on Humanoid Robots (Humanoids)*. IEEE, Nov. 2015. DOI: 10.1109/humanoids.2015.7363525.

[40] Urbann, O. and Tasse, S. “Observer based biped walking control, a sensor fusion approach”. In: *Autonomous Robots* 35.1 (Apr. 2013), pp. 37–49. DOI: 10.1007/s10514-013-9333-4.

[41] Vold, H., Crowley, J., and Rocklin, G. T. “New ways of estimating frequency response functions.” In: *S V Sound and Vibration* 18.11 (1984), pp. 34–38. ISSN: 00381810.

[42] Wahrmann, D., Hildebrandt, A.-C., Bates, T., Wittmann, R., Sygulla, F., Seiwald, P., and Rixen, D. “Vision-Based 3D Modeling of Unknown Dynamic Environments for Real-Time Humanoid Navigation”. In: *International Journal of Humanoid Robotics* 16.01 (Feb. 2019), p. 1950002. DOI: 10.1142/s0219843619500026.

[43] Winter, D. “Human balance and posture control during standing and walking”. In: *Gait & Posture* 3.4 (Dec. 1995), pp. 193–214. DOI: 10.1016/0966-6362(96)82849-9.

[44] Wu, S.-T., Lian, S.-H., and Chen, S.-H. “Vibration control of a flexible beam driven by a ball-screw stage with adaptive notch filters and a line enhancer”. In: *Journal of Sound and Vibration* 348 (July 2015), pp. 71–87. DOI: 10.1016/j.jsv.2015.03.025.

Disclaimer

I hereby declare that this thesis is entirely the result of my own work except where otherwise indicated.
I have only used the resources given in the list of references.

Garching bei München, May 15, 2020

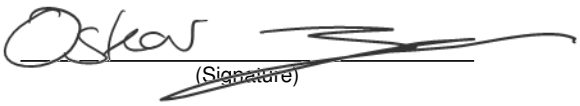

(Signature)